Saucer-shaped sills, magma fingers and lobes: Insights from 3D laboratory experiments

Uchitha Nissanka Arachchige

BSc Hons, MSc

A thesis submitted for the degree of

Doctor of Philosophy

At Monash University in 2021

School of Earth, Atmosphere and Environment

Faculty of Science

Copyright notice

Abstract

Saucer-shaped sill complexes are observed in sedimentary basins worldwide and are considered to be one of the main principal pathways for magma transport through the upper crust. Recent field and three-dimensional (3D) seismic reflection survey observations indicate that these sills have non-planar margins, consisting of lobes and finger-like segments. The emplacement mechanisms of saucer-shaped sills into rheologically complex, visco-elasto-plastic host rocks and how and where lobe and finger-like segments emerge from these intrusions remain poorly understood. This thesis aims to address these fundamental knowledge gaps through the use of 3D laboratory experiments.

Rheological analyses of gel-forming Laponite RD® (LRD) were performed to evaluate its suitability as a visco-elasto-plastic laboratory analogue for upper crustal rocks. The analyses reveal that LRD gels change from a brittle, elastic-dominant, linear viscoelastic material to a plastic material as shear strain increases. The linear viscoelastic region occurs for lower shear strains before it yields and then undergoes strain hardening, before a peak stress occurs as the shear strain increases. LRD at higher shear strains beyond peak stress behaves as a plastic material. LRD can be used to model elastic deformation within linear viscoelastic region at a shear strain rate of 0.1 s^{-1} and plastic deformation at higher shear strains. It is concluded that LRD is an ideal material for modelling the behaviour of rocks during the emplacement of magma and the propagation of brittle fractures in the upper crust.

Experiments were performed to understand the emplacement of saucer-shaped sills and sill segmentation using LRD and paraffin oil as the upper crustal and magma analogues, respectively. Layering of rocks was simulated by varying the concentration and strength of LRD. Saucer-shaped sills formed in experiments in which an inner flat sill formed along the two-layer interface, and an outer inclined sheet formed in the homogeneous upper layer. Sharp transitions occur between inner flat sills to outer inclined sheets, both of which have non-planar margins with lobe and finger-like and segments. It is proposed that the saucer-shaped sills formed in the experiments are compatible with linear elastic fracture mechanism (LEFM) models in which the inner to outer sill transition occurs due to an elasticity-dominated interaction between the growing inner sill and the surrounding material and free surface.

Detailed geometrical analysis of the segmentation observed at the experimental sill margins identifies a bimodal behaviour of marginal segments: i) wide lobes with small aspect ratios controlled by layer interfaces; and ii) narrow and long segments with large aspect ratios that form in the homogenous upper layer. It is proposed that intrusion large-scale sill segmentation is linked to mixed mode (I+III) fracturing within inclined sheets and small-scale visco-plastic instabilities dominate within the interface. A major implication of this thesis is that segments evolve in space and time and multi-stage emplacement mechanisms should be considered. The findings of this thesis are applicable to Ni-Cu sulphide deposits, and they can be used to track magma flow pathways and to discover potential orthomagmatic ore deposits.

Publications during enrolment

- Laponite gels - visco-elasto-plastic analogues for geological laboratory modelling
  Arachchige, U.N., Cruden, A.R., Weinberg, R., 2021
  Tectonophysics 805, 228773

Thesis including published works declaration

I hereby declare that this thesis contains no material which has been accepted for the award of any other degree or diploma at any university or equivalent institution and that, to the best of my knowledge and belief, this thesis contains no material previously published or written by another person, except where due reference is made in the text of the thesis.

This thesis includes one original paper published in a peer reviewed journal. The core theme of the thesis is structural magmatism. The ideas, development and writing up of all the papers in the thesis were the principal responsibility of myself, the student, working within the School of Earth, Atmosphere and Environment under the supervision of Prof. Alexander R. Cruden and Prof. Roberto F. Weinberg.

(The inclusion of co-authors reflects the fact that the work came from active collaboration between researchers and acknowledges input into team-based research.)

In the case of Chapters 2, 3, and 4, my contribution to the work involved the following:

Thesis Chapter	Publication Title	Status	Nature and % of student contribution	Co-author name(s) Nature and % of Co-author's contribution	Co-author(s), Monash student
2	Laponite gels - visco-elasto-plastic analogues for geological laboratory modelling	Published	85% Design, data acquisition and analysis, manuscript writing	Alexander R. Cruden 10% Roberto Weinberg 5%	No No
3	Laboratory Modelling of Sill Emplacement: Part 1: Saucer-shaped intrusions	Not submitted	85% Design, experiments, data acquisition and analysis, manuscript writing	Alexander R. Cruden 7% Roberto Weinberg 3% Jonas Köpping 3% Anja Slim 2%	No No Yes No
4	Laboratory Modelling of Sill Emplacement: Part 2: Sill segmentation	Not submitted	85% Design, experiments, data acquisition and analysis, manuscript writing	Alexander R. Cruden 10% Roberto Weinberg 5%	No No

I have renumbered sections of submitted or published papers in order to generate a consistent presentation within the thesis.

Student name: Uchitha Nissanka Arachchige

Student signature: **Date:** 18/11/2021

I hereby certify that the above declaration correctly reflects the nature and extent of the student's and co-authors' contributions to this work. In instances where I am not the responsible author I have consulted with the responsible author to agree on the respective contributions of the authors.

Main Supervisor name: Alexander R Cruden

Main Supervisor signature: **Date:** 18/11/2021

Acknowledgements

In September 2017, I had three PhD offers from USA, Canada and Australia and was in great doubt about which one to accept because it would obviously change my future. The way Sandy Cruden, my eventual main supervisor, replied to me, his patience and lenience resolved my doubts and I jumped onto a plane in October that year, leaving my 10 day-old baby girl with a lots of hard feelings, insecurities and sadness for leaving what I loved most back home. Thinking back to the last 4 years, what I have learned is immeasurable. Thank you Sandy, thank you for giving me this opportunity and believing in me. There were a few times during my PhD career when I wanted to quit, but you were always there saying "Just hang on Uchi, you can do it," which always strengthened my mind. Thank you for pushing me forward and giving your total support to me and my family.

I would also like to thank my co-supervisor, Roberto Weinberg for your support and guidance. In my world, you are a legendary man who always thinks out of the box with creative ideas. Roberto, thanks for sharing your extensive knowledge and for the exciting discussions, for improving my writing – most of all – for showing me how to think scientifically and encouraging me to aim high.

This research was supported through the Co-funded Monash Graduate Scholarship (MGS), Dean's International Postgraduate Research Scholarship (DIPRS) and an Australian Research Council Discovery Grant (DP190102422).

It's been a long, stressful and winding journey, but I have managed to finish my PhD and learned not only about geology, but even more about "life". Nothing would have been possible without the help of many people, which I consider as team work.

Thank you to my PhD panel members, Steven Mickelthwaite, Jozua van Otterloo, Oliver Nebel, Andrew Tomkins, and Anja Slim for your constructive feedback and leaving me your doors open for a chat. I would specially like to thank Anja, for all your time, exciting discussions and helping me to bridge the unknown gap of geology and physics in my project.

I wish to thank the support staff at EAE, Emily, Silvana, Leigh, Junnel, Caroline, Rob, Yuzhou, Ada, Christine, Rachelle and Massimo for providing such a friendly, helpful and straightforward work environment. I am also very thankful to Brett, Antonio and the whole team at the Monash Instrumentation Facility for their support with the experimental apparatuses I have used for my research. I have spent countless hours working in our geodynamic lab, and without the help, advice and guidance of Nic, Anung, Hany and Megan I wouldn't have gotten so far. Thank you guys, you have been very helpful.

My officemates Gan, Yuval, Sony and Emma also deserve credit for making work a friendly place and tolerating my excited discussions. I would also like to thank our Friday soccer team: Mathias, Cass, Ben, Dietmar, Luis, Francisco and Davide for keeping me strong. I am also very thankful to Jonas, my research partner, for your countless discussions, helping me with analyses and an interesting time during our Montana fieldwork.

I wouldn't be where or who I am without my parents, Shirani and Susil. Thank you for believing and always encouraging to be my best self. Thank you Nandawathie and Dharmakeerthi, my mother and father-in-laws for your great support throughout this period.

Purni, nothing would have been the same without you. I knew nothing about love before, but I am learning it with you. You never got off the roller coaster which I have ridden. Thank you for all your efforts, your sacrifices and taking care of our two babies during my PhD period. I made it thanks to you.

Table of contents

Chapter 1

Introduction

1.1 Project rationale

The geometries of planar igneous intrusions such as dykes and sills have often been used to delineate emplacement mechanisms, magma flow pathways, and melt source locations in crustal-scale magma plumbing systems. It is known that some sills deviate from their strata-concordant, planar geometry to define so-called saucer-shaped sills, which have concave upward shapes and strata-discordant outer sheets. It is also known that dykes and sills do not always propagate with uniform margins but instead break down into finger-like and/or lobate segments. Emergence of such segments from the margins of planar intrusive sheets is observed in several mafic sill complexes such as in the Karoo (e.g., Golden Valley sill; Schofield et al., 2010), Raton, Rockall, Neuquén, Faroe-Shetland, and Møre basins (e.g., Vigra sill; Miles and Cartwright, 2010). Finger-like structures that emerge from mafic sills are also known to trap Ni-Cu sulphides in narrow, elongated channels that are observed in deep to upper crustal levels. Ni-Cu sulphide deposits, such as Noril'sk, Voisey Bay, Nebo-Babel, Uitkomst, Eagle and Jinchuan are hosted within igneous intrusions that show characteristic finger-like geometries (Barnes et al., 2016). Therefore, intrusive planar sheets and channelized finger-like structures in magma plumbing systems are important for transport of both magma and economically important metals from deep mantle sources to upper crustal levels.

Despite decades of research on the emplacement mechanisms and structural characteristics of igneous intrusions, the emplacement of saucer-shaped sills within rheologically complex host rocks (i.e. visco-elasto-plastic) and understanding of how and where finger-like and lobate segments emerge from these intrusions remain poorly understood. In this thesis, I employ a laboratory modelling approach that allows me to scale down time, dimensions, mechanical and rheological properties of host rocks and magmas to approximately simulate igneous intrusion processes at more convenient timeframes and length scales. The outcome of this modelling approach will be to create new knowledge on the complexities of sills in nature, constrain how they are emplaced and propagate in the shallow crust, and how complex, segmented structures develop along sill margins.

1.2 Aims and motivation

The overarching aim of this work is to better understand the fundamental processes that form saucer-shaped intrusions and how and why marginal sill segmentation occurs. This thesis aims to answer the following outstanding questions about sill emplacement mechanisms within rheologically complex host rocks and how parameters such as host rock mechanical properties control the formation of segmented saucer-shaped intrusions:

- How do the rheological and mechanical properties of host rocks influence the formation of the saucer-shaped intrusions?
- How and why do finger-like and lobe structures emerge from planar magmatic intrusions?
- What processes control the geometries of segmented sill margins during magma emplacement?

These questions are addressed using three dimensional (3D) laboratory experiments that simulate the injection of magma into a layered visco-elasto-plastic upper crust. The experimental results are compared with selected natural examples as well as previous analogue and numerical modelling studies.

1.3 Thesis structure

This thesis comprises an introductory chapter, followed by three research chapters and a final discussion and conclusions chapter. Chapters 2-4 have been formatted as stand-alone journal articles. Chapters 2 and 3 are identical to the published/submitted versions with minor amendments such as referencing styles to maintain a constant format throughout the thesis. Chapter 4 will be ready for journal submission after minor modifications.

Chapter 1 introduces the research topics of the thesis and presents key background information, including a literature review on non-planar magmatic intrusions, magma propagation structures and geodynamic modelling, and a detailed description of laboratory modelling methods and scaling.

Chapter 2: Laponite® gels – Visco-elasto-plastic analogues for geological laboratory modelling

Uchitha N. Arachchige, Alexander R. Cruden, Roberto Weinberg.
Published in Tectonophysics (2021): https://doi.org/10.1016/j.tecto.2021.228773

This chapter characterises the rheological and mechanical properties of Laponite RD® (LRD), the host rock analogue in my analogue models, using a series of rheological tests. It also assesses the suitability of LRD for use in geological analogue modelling.

Chapter 3: Laboratory modelling of sill emplacement: Part 1 - Saucer-shaped intrusions.

Uchitha N. Arachchige, Alexander R. Cruden, Roberto Weinberg, Jonas Köpping, Anja Slim. Unpublished.

This chapter presents the results of a series of isothermal experiments in which I investigate the formation and growth of saucer-shape sills emplaced into layered and homogeneous visco-elasto-plastic LRD gels. This chapter also includes a complete description of the modelling setup and scaling, which is used as a reference for Chapter 4. This work highlights the first laboratory experimental simulation of saucer-shaped sills in layered visco-elasto-plastic host rocks.

Chapter 4: Laboratory modelling of sill emplacement: Part 2 - Sill segmentation.

Uchitha N. Arachchige, Alexander R. Cruden, Roberto Weinberg.
Unpublished.

Non-planar sill intrusions in nature and segmentation of their margins during intrusion can be used to delineate magma propagation pathways and emplacement mechanisms. However, insights from laboratory experimental modelling is still lacking. This chapter presents results of a series of laboratory experiments that focus on the analysis of marginal segment geometries and the controls on their formation.

Chapter 5 summarises and synthesises the main findings of the three research chapters, and discusses their implications in a broader context. Research questions that require further investigation are also discussed.

1.4. Context of the research

1.4.1. Sills

Igneous sills constitute a major component of volcanic plumbing systems (Chevallier and Woodford, 1999; Thomson and Hutton, 2004; Hansen and Cartwright, 2006; Kavanagh et al., 2006, 2015; Bunger and Cruden, 2011; Muirhead et al., 2012; Magee et al., 2018). Recent field and 3D seismic reflection observations also highlight that extensive lateral and vertical magma transport may occur within mafic sill complexes (Magee et al., 2016, 2018; Spacapan et al., 2017; Galland et al., 2019).

On the basis of their low thickness-to-length aspect ratios, the most commonly accepted model for sill emplacement model assumes that they are fluid pressure-driven (hydraulic) fractures (Lister and Kerr, 1991; Rubin, 1995). Most theoretical and numerical models of sill emplacement are therefore based on intrusion into purely elastic host rocks (Pollard and Johnson, 1973; Lister, 1990; Menand and Tait, 2002; Rivalta et al., 2005; Taisne and Tait, 2009; Bunger and Cruden, 2011). This mechanism is further supported by laboratory experimental modelling of sills (Kavanagh et al., 2006, 2017; Bunger et al., 2008; Mathieu et al., 2008; Menand, 2008; Chanceaux and Menand, 2014). However, in many sedimentary basins, igneous sills are often emplaced into rocks, like shale, that deform in an inelastic manner (Pollard et al., 1975; Schofield et al., 2010; Magee et al., 2016). Mechanisms other that purely elastic fracturing, such as localized shear-failure and/or ductile flow (e.g., Pollard et al., 1975; Haug et al., 2017), host rock fluidization (e.g., Schofield et al., 2010, 2012) and viscous indentation and "bulldozing" (e.g., Spacapan et al., 2017) have therefore also been proposed to explain the formation of igneous sills in sedimentary basins.

Although sill emplacement mechanisms have been widely studied, the formation of saucer-shaped intrusions (Fig. 1.1), non-planar sill fronts and marginal segmentation (Fig. 1.2) during sill emplacement are still not well understood. The sections below summarise recent progress in understanding of the geometry and emplacement mechanisms of non-planar sills.

1.4.1. Saucer-shaped sills

Saucer-shaped sill morphologies are considered to be a fundamental and common geometry of intrusions in sedimentary basins (Galland et al., 2009; Galland & Scheibert, 2013; Chen et al., 2017). Field observations of saucer-shaped sills (Fig. 1.1a) in the Golden Valley Sill Complex, South Africa (Chevallier and Woodford, 1999; Planke et al., 2005; Planke, 2008) and from 3D seismic observations (Thomson and Hutton, 2004; Hansen and Cartwright, 2006; Polteau et al., 2008a) have shown that they typically exhibit a sub-horizontal, strata-concordant inner sill forming the base, and an inclined upward and outward branching outer sheet that cross-cuts the overburden strata (Fig. 1.1b).

A variety of mechanisms have been proposed to explain the formation of inclined sheets within saucer-shaped sills. These mechanisms mainly invoke dominantly elastic (Pollard and Holzhausen, 1979) or plastic (Galland et al., 2009; Haug et al., 2017) behaviours of the host rocks. Elastic-dominant numerical (Malthe-Sørenssen et al., 2004; Gill and Walker, 2020; Walker and Gill, 2020) and laboratory experiments (Bunger et al., 2008) show that saucer-shaped sills can form due to the mechanical interplay between elastic deformation around the growing sill and its interaction with the Earth's free surface. In contrast, some laboratory (Mathieu et al., 2008; Galland et al., 2009) and numerical (Haug et al., 2017) models argue that the inclined sheets of saucer-shaped sills can be created due to inelastic damage (i.e., plastic failure) caused by an inflating inner sill.

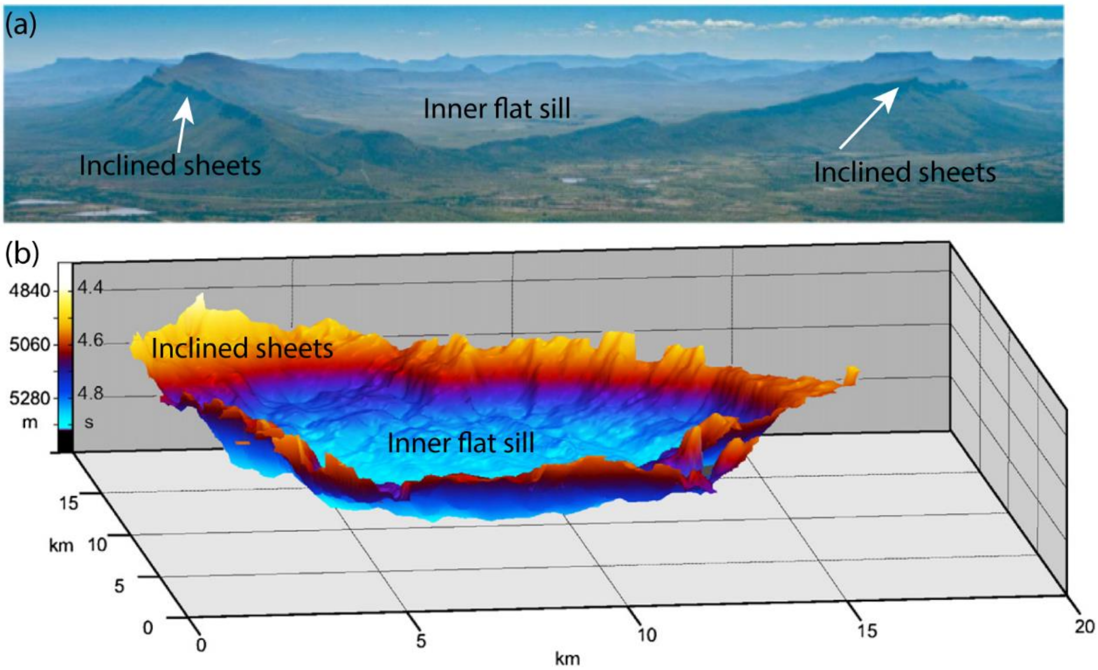

Figure 1.1. *(a) Oblique aerial view of the Golden Valley sill in the Karoo basin, South Africa showing an inner flat sill and outer inclined sheets (Polteau et al., 2008b). (b) 3D seismic interpretation of a saucer-shaped sill in the More Basin offshore Mid-Norway (modified from*

Despite these end member models, the formation and propagation of saucer-shaped sills within more rheologically (e.g., visco-elasto-plastc) and mechanically (e.g., layered) complex host materials that are similar to rocks in nature remain largely unexplored. Moreover, previous experiments have always produced saucer-shaped intrusions with planar propagating fronts, without forming segmented margins (i.e., lobes and fingers; Fig. 1.2) that are commonly observed in nature (Thomson and Hutton, 2004; Hansen and Cartwright, 2006; Magee et al., 2016).

1.4.2. Sill segmentation

Field observations and 3D seismic surveys (Fig. 1.2) have found that most sills consist of segments that range in size from metres to kilometres (Pollard et al., 1975; Thomson and Hutton, 2004; Hansen and Cartwright, 2006; Magee et al., 2016). In the intrusion literature, this segmentation often refers to the separation of originally planar sill margins into laterally and/or vertically offset, overlapping and/or underlapping individual segments, such as magma lobes and fingers (Schofield et al., 2012; Magee et al., 2016). Moreover, at a particular time step during emplacement, the intrusion margin may consist of a combination of two or more different segments (i.e., lobes or fingers) with a range of sizes, which we refer to here as "complex segmentation". The term magma lobe (Fig. 1.2a, b) in the sill literature is a purely morphological term that refers to a near-circular to elongated lobe-shaped geometry (Miles and Cartwright, 2010; Schofield et al., 2012). The term magma finger (Fig. 1.2a, c) commonly describes elongated, narrow segments with blunt and/or bulbous terminations at the leading edges of dykes and sills (Pollard et al., 1975; Schofield et al., 2010; Spacapan et al., 2017; Galland et al., 2019).

The formation of long, linear intrusive segments is often attributed to Linear Elastic Fracture Mechanics (LEFM) processes, whereby segments are idealised as Mode 1 elastic fractures with tapered (wedge-shaped) or sharp tips (Pollard, 1973; Delaney and Pollard, 1981; Rubin, 1993). Magma flow connectors between segments, such as intrusive steps and bridge structures (Fig. 1.2d), result from the segmentation and propagation of tensile elastic fractures ahead of an advancing planar intrusion that are oriented orthogonal to the minimum principal stress (σ_3) direction.

However, several studies suggest that mechanisms other than elastic fracturing, such as ductile flow, shear faulting and granular flow (e.g., fluidisation) can also result in magma finger formation (Pollard et al., 1975; Thomson and Hutton, 2004; Schofield et al., 2012; Magee et al., 2016; Spacapan et al., 2017). A viscous indentation model has been proposed to explain the formation of magma fingers in the Neuquen basin, Argentina (Fig. 1.1b; Spacapan et al., 2017) in which shear failure of the host rocks is promoted by viscous shear stresses adjacent to a propagating sill tip. Non-brittle emplacement mechanisms, mainly attributed to Saffman-

Taylor viscous instabilities (Saffman and Taylor, 1958; Pollard et al., 1975), may explain how magma fingers can form during in-situ boiling and volatization of host-rock pore-fluids (thermal fluidization) or rapid, fracture-related depressurization of pore-fluid causing host-rock disaggregation (triggered fluidization) (Schofield et al., 2010).

Emergence of magma fingers and lobate fronts from sill margins has also been explained by magma cooling and solidification (Holness, 2003; Miles and Cartwright, 2010), whereby sudden opening of stalled planar fracture fronts leads to marginal finger and lobe formation (Currier and Marsh, 2015). This mechanism is analogous to the development of frontal lobes and channels in lava flows (Kerr et al., 2006). It has also been observed in laboratory experiments in which hot vegetable oil is injected to colder layered solid gelatine to model solidification effects during sill formation (Fig. 1.2d) and propagation (Chanceaux and Menand, 2014, 2016).

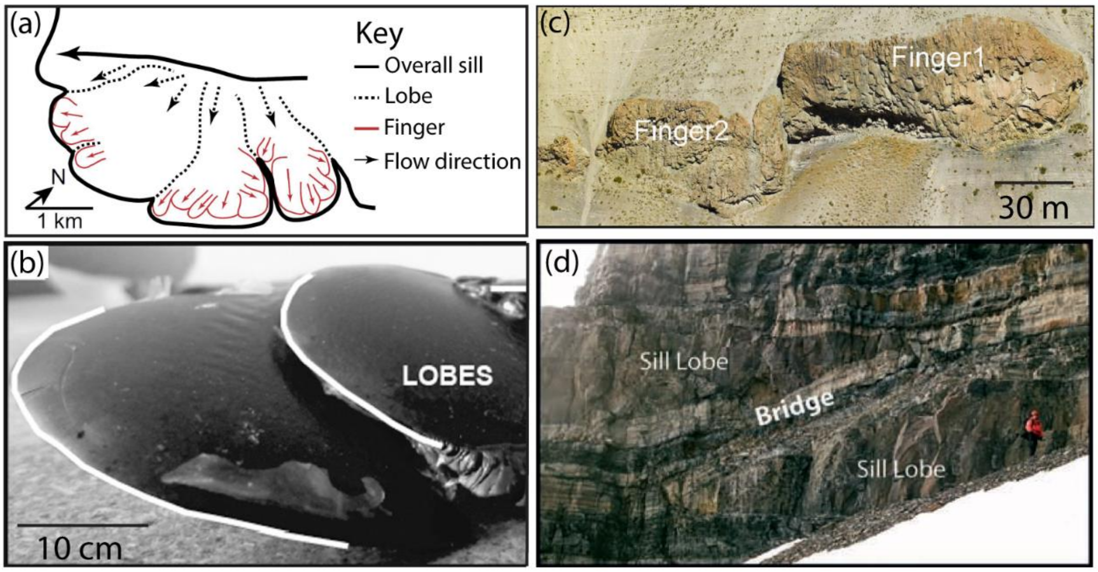

Figure 1.2. *Non-planar geological structures in magmatic intrusions (a) Magma lobes and fingers mapped in 3D seismic reflection data in a sill located in the Rockall Trough (modified after Thomson and Hutton, 2004; figure from Magee et al., 2015). (b) Magma lobes formed in solidification experiments of vegetable oil injected into a gelatine host (figure from Chanceaux and Menand, 2014). (c)Magma fingers in the Neuquén Basin, Argentina (figure from Galland et al., 2019). (d) Cross section image of a bridge structure within overlapping sill lobes in Theron Mountains (modified after Hutton, 2009).*

1.5 Methodology

All of the experimental results presented in this thesis are based on scaled analogue modelling of magma emplacement. Analogue modelling is a technique that is used to test models and/or hypotheses in the laboratory at convenient time and length scales. Ramberg (1967) famously stated:

"The significance of scale-model work in tectonic studies lies in the fact that a correctly constructed dynamic scale model passes through an evolution which simulates exactly that of the original (the prototype), though on a more convenient geometric scale(smaller) and with a conveniently changed rate (faster)"

Some of the most significant advances in the study of dyke and sill emplacement carried out by means of analogue modelling are summarised below.

1.5.1 Analogue modelling

The correct selection of materials to simulate the behaviour of rocks in the laboratory is an essential step for modelling deformation within Earth's interior at multiple scales. James Hall published the first geological analogue experiment about 200 years ago (Hall, 1815) in an attempt to model the formation of folds in sedimentary strata observed along the Berwickshire coastline of Scotland. A series of landmark laboratory modelling papers in the early 20^{th} century investigated the formation of salt domes (Escher and Kuenen, 1929; Link 1930) and the mechanics of geological structures (Hubbert, 1951). A significant advancement in analogue modelling occurred during the second half of the 20^{th} century as the theory of the plate tectonics was developed in 1960s (Jacoby 1973, 1976; Kincaid and Olson, 1987; Brune and Ellis, 1997). Buckingham's (1914) and Hubbert's (1937) work on the theory of scaling methods, and its application to geological processes, changed the analogue modelling approach from being a qualitative and descriptive tool to an advanced quantitative method. This was further developed by many others (Hubbert 1951; Ramberg 1967, 1981; Shemenda 1983; Weijermars and Schmeling, 1986; Richard 1991; Ribe and Davaille, 2013). Scaling theory, which requires geometric, kinematic and dynamic similarity between an experiment and a natural prototype, allows the experimental results to scale quantitatively to the values in nature, providing a deeper understanding of geological and geodynamic processes.

The first analogue experiments to simulate the processes of magma transport and emplacement were conducted by Daubrée (1891), who designed models to investigate the formation of diatremes. Hubbert and Willis (1957) used elastic gelatine and mud as rock and magma analogues, respectively, to simulate hydraulic fracturing in boreholes, with results that are relevant to the emplacement of igneous dykes and sills. However, the first qualitative laboratory experiments on sill intrusions were conducted by Pollard (1973), who used grease and layered gelatine as magma and host-rock analogue, respectively.

The first quantitative analogue models of sill emplacement were carried out by Rivalta et al. (2005) and Kavanagh et al. (2006; see also Menand 2008), in which air and water (magma analogue) were injected into a layered gelatine host, respectively. In these experiments, the authors systematically varied the input pressure and the rigidity contrast between the upper and lower gelatine layers. These experiments focused on how feeder dykes transition into sills at rock interfaces.

Novel laboratory techniques and analogue materials have also been introduced, resulting in further advances in modelling of magmatic intrusions. Gelatine (Kavanagh et al., 2006; Di Giuseppe et al., 2009; van Otterloo and Cruden, 2016) has been used to simulate viscoelastic host rock deformation during magma emplacement, whereas granular materials such as silica flour (spheres and crystals; Galland et al., 2006), diatomite powder (Gressier et al., 2010), quartz sand and plaster powder (Poppe et al., 2021) and sand (Mathieu et al., 2008) have been used to simulate brittle behaviour. Different types of syrups (Corn and Glucose: Schellart, 2011; Honey: Mathieu et al., 2008), oils (Silicon: Mueller et al., 2009; Vegetable oil: Galland et al., 2006), waxes (Paraffin: Rossetti et al., 1999; Polyethylene glycole (PEG): Griffiths and Fink, 1997), air and water (Huppert and Hallworth, 2007) have been used as to simulate the Newtonian flow behaviour of magma and lava (Griffiths and Fink, 1993; Kerr, 2001; Beckett et al., 2011).

Over the last decade, analogue modelling has been greatly strengthened from the introduction of high-resolution optical image correlation methods (i.e., particle imaging velocimetry, PIV, and digital image correlation, DIC) (e.g., Adam et al., 2005; Galland et al., 2016; Riller et al., 2012; Schrank et al., 2012). The integration of analogue modelling with advanced imaging and deformation monitoring techniques has greatly improved understanding of both dyke and sill emplacement processes. Digital image correlation (DIC) using laser fluoresced tracer particles in host rock analogues were used to quantify incremental and finite strains in gelatine induced by intrusion dynamics (Kavanagh et al., 2015, 2017, 2018). Moreover, these studies have considered how combinations of magma and host rock analogue materials, which impacts the model parameters, for example the buoyancy of the magma analogue through density difference. Imaging of internal structures and deformation has also been quantified using X-Ray computed tomography (X-RCT) scans of analogue experiments (Adam et al., 2013; Zwaan and Schreurs, 2016; Zwaan et al., 2018; Poppe et al., 2019). In addition to the aforementioned contributions, further details of modelling of volcanic magma plumbing systems can be found in extensive reviews by Galland et al. (2015) and Kavanagh et al. (2018).

1.5.2 Experimental design

The experimental set up used in this thesis is designed to simulate lateral emplacement of sills at different crustal levels and to study the propagation and growth of non-planar intrusions. A 2-layer system with a horizontal interface is used to ensure initial sill propagation occurs within a horizontal plane. Digital photography is used to map sill geometries and quantify intrusion growth parameters such as radius, area and velocity over time. Analysis of the resulting parameters allows me to compare the modelling outcomes with previous analogue and numerical results, as well as global field and 3D seismic data examples of sills and saucer-shaped intrusions.

The experiments reported in Chapters 3 and 4 are carried out in a 30 × 30 × 6 cm transparent, acrylic tank (Fig. 1.3). The tank is filled with crustal analogue materials (see material and scaling), usually comprising two horizontal layers (Layers 1 and 2) with different mechanical properties. The magma analogue is injected horizontally along the Layer 1/2 interface via a nozzle at the side of the tank fed by peristaltic pump at controlled volumetric flow rates. Intrusion propagation is monitored by high resolution DSLR cameras placed above (plan view) and at the side (cross sectional view) of the apparatus.

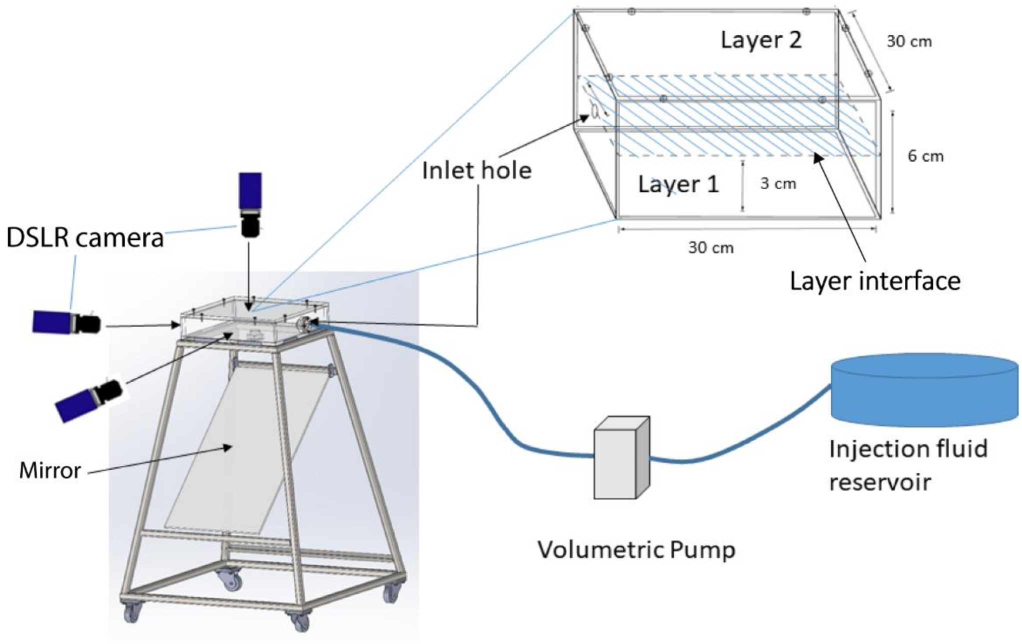

Figure 1.3. *Experimental setup (Chapters 2 and 3) with two analogue crustal layers (Layer 1 and 2). The magma analogue is injected horizontally via an inlet hole, along the Layer1/2 interface.*

1.5.3. Materials and scaling

The correct selection of materials is essential for successful analogue experiments as the materials should capture the mechanical properties of rocks and magmas in nature, thereby satisfying rheological similarity criteria (Weijermars and Schmeling, 1986; Kavanagh et al., 2018b; Reber et al., 2020). Therefore, a complete rheological characterisation of model materials is an important first step in designing analogue experiments. The rheological properties of both crustal and magma analogues were measured using an Anton Paar Physica MCR-301 parallel plate rheometer, following the methods described in previous rheological analysis of analogue modelling materials (ten Grotenhuis et al., 2002; Rivalta et al., 2005; Di Giuseppe et al., 2009; Kavanagh et al., 2013; van Otterloo and Cruden, 2016). The following sections provide a summary of the crustal and magma analogue materials used in my experiments, and the scaling used to compare models (subscript m) with natural prototypes (subscript p).

1.5.3.1. Crustal analogue material

After some preliminary experiments and rheological tests, Laponite RD® (LRD) was selected as the material to model crustal host rock behaviour during analogue sill emplacement. LRD

(Fig 1.4) is a synthetic crystalline layered silicate compound with a crystal structure and chemical composition comparable to the natural clay mineral hectorite (Nuemann, 1965 Cummins, 2007; Wallace and Rutherford, 2015). Despite a decade of research on its material properties, LRD has only been used by Bertelsen et al. (2018) for geological analogue experiments, but shows considerable potential (Kavanagh et al., 2018) as a crustal analogue. Therefore, its suitability as a crustal analogue for magma injection experiments has been assessed by a comprehensive suite of rheological tests and the results are summarised in Chapter 2.

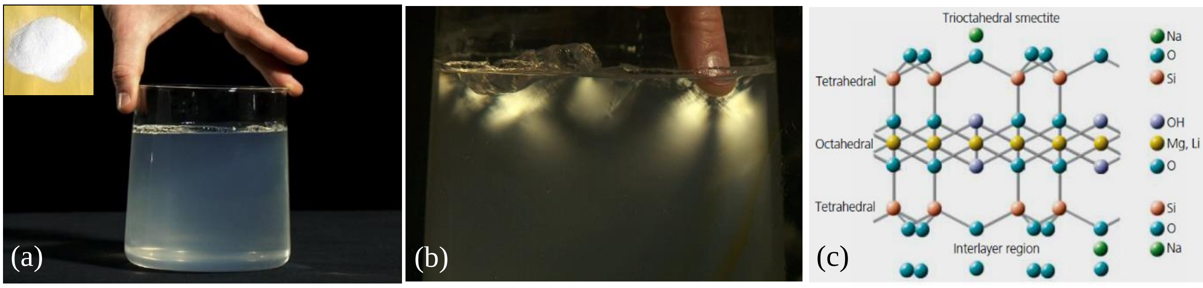

Figure 1.4. *Appearance of Laponite RD® after complete mixing with water (a) and its photo-elastic properties (b). (c) Empirical formula and layered structure of individual Laponite® particles.*

When mixed with water, LRD forms a clear gel, which is similar to gelatine but is colourless and more transparent. Like gelatine, its photo-elastic properties can be used to visualize and map stresses associated with loads and propagating fractures. It is a chemically and biologically stable material and it is easy to alter its mechanical properties, such as the Young's modulus, by changing its concentration in water. LRD has a density around 1000 kg m^{-3} and lower surface energy values (24-44 mJ/m^2; Norris et al., 1993) compared to frequently used host rock analogue gels such as gelatine (1 J/m^2; Kavanagh et al., 2013). This ensures that surface tension dynamics are minimized in geological analogue experiments using LRD. Pressurised cracks in LRD gels form characteristic marginal finger and lobate-like segments, rather than planar cracks with smooth margins. These characteristics, plus its rheological properties, indicate that LRD is an ideal host rock analogue to study the formation and propagation of sills and saucer-shaped sills, and sill segmentation into lobes and fingers.

1.5.3.2. Magma analogue

Paraffin oil (BP Ltd.) at 22.5° was used as the magma analogue in the experiments reported in Chapters 3 and 4. This choice was made because potential water-based magma analogues were observed to react with LRD, resulting in crazing and fracturing that is unrelated to sill emplacement dynamics. Paraffin oil has a viscosity of 0.16 Pa s and a density of 850 kg m^{-3}at this temperature and it was mixed with red dye without altering its viscosity to provide a better visual contrast with the host material. Paraffin oil is a linear, Newtonian fluid (Kavanagh et al., 2018b) and rheological analysis by Duarte et al. (2013; Fig. 5) shows that it is weakly temperature dependant between 16 °C – 24 °C. Therefore, it is assumed that the viscosity of the magma analogue in the isothermal experiments of Chapter 3 and 4 is constant.

1.5.3.3. Scaling

The experimental approach is focused on modelling the emplacement of igneous sills and saucer-shaped intrusions in a horizontally layered analogue upper crust. The scaling, material selection and general design of the experiments follows the analogue modelling approach described by Hubbert (1937), Ramberg (1967) and used by Merle and Borgia (1996), Rivalta et al. (2005), Kavanagh et al. (2006), Mathieu et al. (2008), Menand, (2008) and Galland et al. (2009). Scaling factors and dimensionless numbers are defined for the models in order to satisfy geometric, kinematic and dynamic similarity with structures and processes in nature. However, the scaling is only approximate since uncertainties and complexities that are likely to occur in nature are not reproducible in the laboratory.

We define the length scaling factor (L*) as the ratio of the final length of a sill in the experiment (l_m) to the typical length of an igneous sill in the shallow crust (l_p). In our case $L^* = l_m/l_p = 10^{-4}$ and 1 cm in the laboratory represents 100 m in nature. The density scaling factor ρ* = 0.357 is defined as the ratio between the density of LRD in the experiments and natural sedimentary host rocks. All experiments are carried out under the normal gravity field (1 g), therefore the gravity scaling factor, g* = 1. This gives a stress scaling factor

$$\sigma^* = \rho^* \, g^* \, L^* = 3.57 \times 10^{-5} \tag{1.1}$$

Comparing the average experimental model intrusion tip velocity of ~ 1 x 10^{-3} ms^{-1} to an estimated magma intrusion velocity of 0.2 ms^{-1} in nature (within a range between 0.1 ms^{-1} and 0.5 ms^{-1}; Spence and Turcotte, 1985; Kavanagh et al., 2013), gives a velocity scaling factor, $V^* = 5 \times 10^{-3}$. The time scaling factor can now be defined as:

$$t^* = L^*/V^* = 2 \times 10^{-2} \tag{1.2}$$

such that 1 min in the experiments represents 0.83 hr in nature. Using σ^* and t^*, the viscosity scaling factor becomes:

$$\mu^* = \sigma^* t^* = 7.2 \times 10^{-7} \qquad (1.3)$$

Hence, paraffin oil (magma analogue) with a viscosity of 0.16 Pas is equivalent to a magma in nature with a viscosity of 10^4 Pas, consistent with basaltic andesite with a low crystal content (Fig 2: Mathieu et al., 2008).

Chapter 2

Laponite® gels – Visco-elasto-plastic analogues for geological laboratory modelling

Uchitha N. Arachchige[1], Alexander R. Cruden[1], Roberto Weinberg[1]

[1]School of Earth, Atmosphere and Environment, Monash University, 9 Rainforest Walk, Clayton, VIC 3800, Australia

Tectonophysics, published manuscript (2021), doi: 10.1016/j.tecto.2021.228773

Abstract

Laponite® is a synthetic clay that, depending on concentration, temperature and curing time, forms a clear, transparent thixotropic fluid or brittle visco-elasto-plastic gel when mixed with water. Here we present the results of rheological and mechanical testing of gel-forming Laponite RD® (LRD) to evaluate its suitability as a rock analogue in laboratory analogue experiments. Rheological tests of 2 – 4 wt. % concentrations of LRD in deionised water were carried out at temperatures between 20 and 50 °C, and after curing times of 3 to 14 days. Our results show that LRD gels change from a brittle, elastic-dominant, linear viscoelastic material to a plastic material as shear strain increases. The linear viscoelastic region occurs at shear strains, $\gamma < 10$ % after which the material yields and then undergoes strain hardening before a peak stress occurs at $\gamma = 15 – 20$ %. LRD then strain softens up to $\gamma < 26.2$ %, beyond which it behaves as a plastic material. Empirical equations are provided that predict increases in the Young's and complex shear moduli of LRD with increasing concentration and ageing time. LRD can be used to model elastic deformation when $\gamma < 10$ % at a shear strain rate of 0.1 s^{-1} and plastic deformation when $\gamma > 26.2$%. LRD is an ideal material for modelling the behaviour of rocks during the emplacement of magma and the propagation of brittle fractures in the upper crust. Its ease of preparation, low surface tension, full transparency, chemical and biological stability and photoelastic properties provide further advantages for analogue laboratory modelling compared to other frequently used visco-elastic gels, such as pig skin gelatine.

Keywords: Laponite RD®; analogue material; rheology; yield stress; visco-elasto-plastic; magma emplacement and crack propagation

2.1. Introduction

Geological processes such as the transport and emplacement of magma in dykes and sills in the Earth's crust and associated host rock deformation are important for the development of upper crustal magma plumbing systems and the formation of magmatic ore deposits (Barnes et al., 2016; Magee et al., 2016). Although field and geophysical methods are used to study these processes either remotely or in exhumed ancient examples (e.g., Magee et al., 2018), direct, detailed and quantitative analysis of dyke and sill emplacement is typically carried out through analogue and/or numerical modelling (Galland et al., 2009; A P Bunger and Cruden, 2011; Kavanagh et al., 2015; Schmiedel et al., 2019). The reproducibility of natural geological structures at laboratory time and length scales, and the controllability of all relevant parameters using model scaling theory are powerful aspects of the analogue modelling approach (Kavanagh et al., 2006, 2018). Properly scaled materials and setups in laboratory experiments can therefore provide a better understanding of natural processes, and results can be compared to field and geophysical observations, and numerical analyses (Kavanagh et al., 2018b; Reber et al., 2020).

Visco-elasto-plastic Laponite® gels (3.3 wt. %) with short curing times (up to 240 min) were used as country rock analogues for two dimensional experiments of magma emplacement in a Hele-Shaw cell by Bertelsen et al. (2018). These authors noted that the material properties of Laponite® gels are not yet sufficiently well characterised for use as natural rock analogues in geological laboratory experiments. Here we report results of a systematic rheological study of Laponite RD® (LRD) gels in order to evaluate their suitability as host rocks in analogue modelling of magma emplacement processes, and other experimental tectonic applications.

Laponite® has been studied extensively in the polymer and clay sciences, and aqueous solutions of Laponite synthetic clays have attracted considerable interest as a rheological modifier for various applications such as surface coatings, consumer care products, paints, emulsion stabilisers, and mineral and hydrocarbon extraction technologies. Aqueous dispersions of Laponite with different concentrations and ionic strengths have received much attention in the colloid and polymer sciences, and their gel or glass-like behaviours (Bonn et al., 1999), surface chemistry, basic rheological properties (Pek-Ing and Yee-Kwong, 2015), and colloidal phase behaviour (Cummins, 2007; Ruzicka and Zaccarelli, 2011; Mohanty and Joshi, 2016) are well characterised.

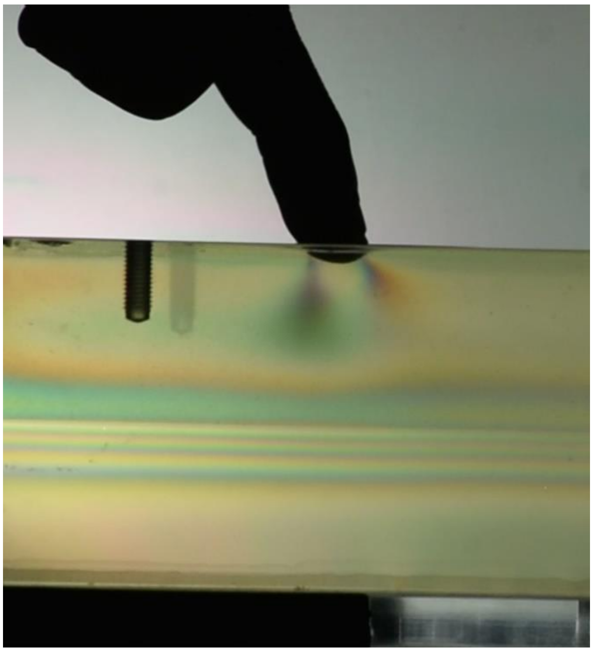

Figure 2.1. *Photo-elastic fringes within a container of layered Laponite RD® loaded from above, indicating the stress field induced by the applied force. Horizontal colour zones in the middle are due to photo-elastic effects caused by Laponite RD® multi-layers.*

LRD has several advantages as an elastic host rock analogue for laboratory modelling of magma transport and pressurized crack propagation compared to commonly used semi-transparent pig skin gelatine (Kavanagh et al., 2013; Brizzi et al., 2016; van Otterloo and Cruden, 2016). LRD is a gel forming grade of Laponite® that is fully transparent, regardless of concentration and sample age. LRD gels (Fig. 2.1) are chemically and biologically stable viscoelastic solids with photo-elastic properties (Ruzicka and Zaccarelli, 2011; Kaushal and Joshi, 2014; Galland et al., 2015; Kavanagh et al., 2018). They have lower surface tension with water (72.8 mJ/m^2, Norris et al., 1993) and glycerol (64 mJ/m^2, Norris et al., 1993) compared to pig skin gelatine (1 J/ m^2; Kavanagh et al., 2013), which minimizes surface tension effects in geological experiments. After initial preparation, LRD mixtures remain in a weak solution state after a few minutes of curing (0 – 60 min), while the gel state is reached after several hours (~ 120 min) (Kaushal and Joshi, 2014; Bertelsen et al., 2018a). The rheological properties reported here are for LRD gels that have been cured over 3 to 14 days.

2.2. General properties of Laponite RD®

2.2.1. Composition and structure

Laponite RD® (LRD; manufactured by BYK Additives and Instruments) is a gel-forming grade of a synthetic sheet silicate with a crystal structure and chemical composition similar to the natural clay mineral hectorite (Nuemann, 1965; Cummins, 2007; Wallace and Rutherford, 2015). Disc-shaped, nearly uniform Laponite crystals ($Si_8Mg_{5.45}Li_{0.4}O_{24}Na_{0.7}$) comprise one octahedral coordinated magnesium or aluminium oxide layer sandwiched in between two layers of tetrahedral coordinated silica (Fig. 2.2a). The unit cell has an overall net negative charge of approximately 700 electron charges, which becomes neutralised when interlayer Na+ ions are absorbed on to the surface of the crystal (Bonn et al., 1999; Cummins, 2007; Lapasin et al., 2017). As reported by BYK Additives and Instruments (2014), the bulk density of LRD is 1000 kg/m^3 and a single Laponite crystal is disc shaped with a typical diameter of 25 nm and height of 0.92 nm (Fig. 2.2b).

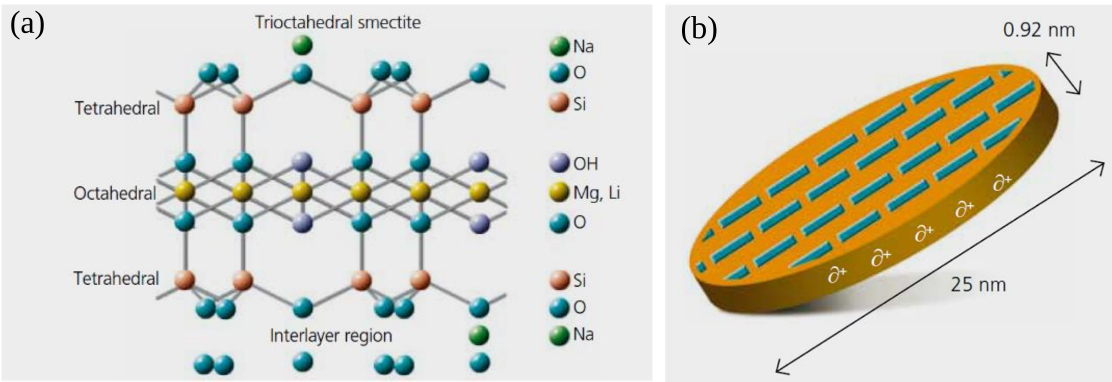

Figure 2.2. *(a) Empirical formula and layered structure of individual Laponite® particles. (b) Disc-shaped Laponite® crystal with thickness (0.92 mm) and diameter (25 mm) with negatively charged faces and positively charged edges (BYK additives and instruments, 2014).*

2.2.2. Sample preparation

In order to achieve full hydration when LRD powder is mixed with water, our sample preparation followed the laboratory-scale mixing procedure recommended by the manufacturer and the previous studies (Appendix 1). Room temperature (19 - 23°C), filtered, deionised water is first poured into a high-speed, 3L capacity commercial blender. Unlike gelatine, LRD can be mixed and forms a gel at room temperature without cooling, which is an added advantage. With the blender rotating, the desired amount of Laponite powder is gradually added to a known volume of deionised water over a period between 10 to 30 s. The sample is then blended for up to 20 min to achieve full hydration and dispersion of the LRD-water mixture. The LRD mixtures are then poured into containers and left to form transparent gels. The containers were sealed to prevent evaporation of water. Air bubbles typically form in the mixture during high-speed stirring, but they eventually rise to the surface resulting a bubble-free gel sample. Samples with >4 wt. % LRD are impossible to use because they rapidly form a gel before complete mixing occurs. For concentrations <2 wt. % LRD, samples remain in the solution state for much longer times (a few weeks) before a gel structure forms. Therefore, for practical purposes, batches with concentrations of 2, 2.5, 3, 3.5 and 4 wt. % of LRD in deionised water were prepared for rheological measurements.

2.3. Methods

2.3.1 Theoretical background

Combined solid and fluid dynamic approaches are required for complete characterisation of viscoelastic materials that are commonly used in experimental tectonics (Ranalli 1995; ten Grotenhuis et al., 2002; Boutelier et al., 2008; Di Giuseppe et al., 2009). The first approach uses Hooke's law for materials that behave as elastic solids, in which stress (σ) is proportional to the strain (γ) and independent of the strain rate ($\dot{\gamma}$). Elastic solids tend to store energy rather than dissipate it before failing by yielding or brittle fracturing.

A fluid dynamic approach is used to characterise viscous fluids, which dissipate energy. Newtonian viscous materials show a linear proportionality between stress (σ) and strain rate ($\dot{\gamma}$), while in non-Newtonian viscous materials the relationship is non-linear (ten Grotenhuis et al., 2002). Material is considered either shear thickening or shear thinning in the non-Newtonian viscous regime if the viscosity increases or decreases, respectively, with increasing strain rate.

2.3.1.1. Viscoelastic deformation

Viscoelastic materials respond to stress by a combination of elastic and viscous deformation. When subjected to an applied stress, a viscoelastic material may display strain-independent linear viscoelastic and strain-dependent non-linear viscoelastic regimes. The linear and non-linear domains of a viscoelastic material are usually characterised by an elastic storage modulus (G'), representing elastic energy stored during deformation and a loss modulus (G''), representing energy lost by viscous dissipation during and after deformation (Di Giuseppe et al., 2009; Mezger 2006; Xue et al., 2017). For a material in the linear viscoelastic regime, the resulting shear stress (τ) is out of phase with the applied shear strain according to the relationship (Ferry, 1980):

$$\tau = \gamma_0(G'\sin(\omega t) + G''\cos(\omega t)) \quad (2.1)$$

where ω is the frequency and γ_0 is the maximum amplitude of the shear strain. G′ and G″ are the frequency dependent elastic storage and viscous loss moduli, respectively.

The complex shear modulus is derived from the storage and loss moduli:

$$G^* = G' + iG'' \quad (2.2)$$

where the storage modulus is the real part and the loss modulus is the imaginary part and the moduli are perpendicular vectors (Mezger 2006; van Otterloo and Cruden, 2016). The complex shear modulus can be obtained from (Mezger 2006):

$$G^* = \sqrt{G'^2 + G''^2} \quad (2.3)$$

A typical rheological characterisation of a viscoelastic material is illustrated in Fig. 2.3a. This material shows viscous dominant viscoelastic behaviour in the lower frequency range where G″ > G′.

On the other hand, in the higher frequency regions where G′ reaches a plateau value and where the G′/G″ ratio is high (G′ >> G″), the material shows elastic dominant viscoelastic behaviour, which can be described by Hooke's Law. In the cross over region where the elastic and loss moduli have similar values (G′~G″), the material is viscoelastic. The point at which G′ and G″ cross over determines the frequency (ω_c) that gives the Maxwell relaxation time ($t_m = 1/\omega_c$) of the material.

The complex Young's modulus (E*) relates to the complex shear modulus according to (Timoshenko and Goodier, 1970; van Krevelen, 1990):

$$E^* = 2G^*(1+\nu) \quad (2.4)$$

where, ν is Poisson's ratio, which describes the compressibility of the material.

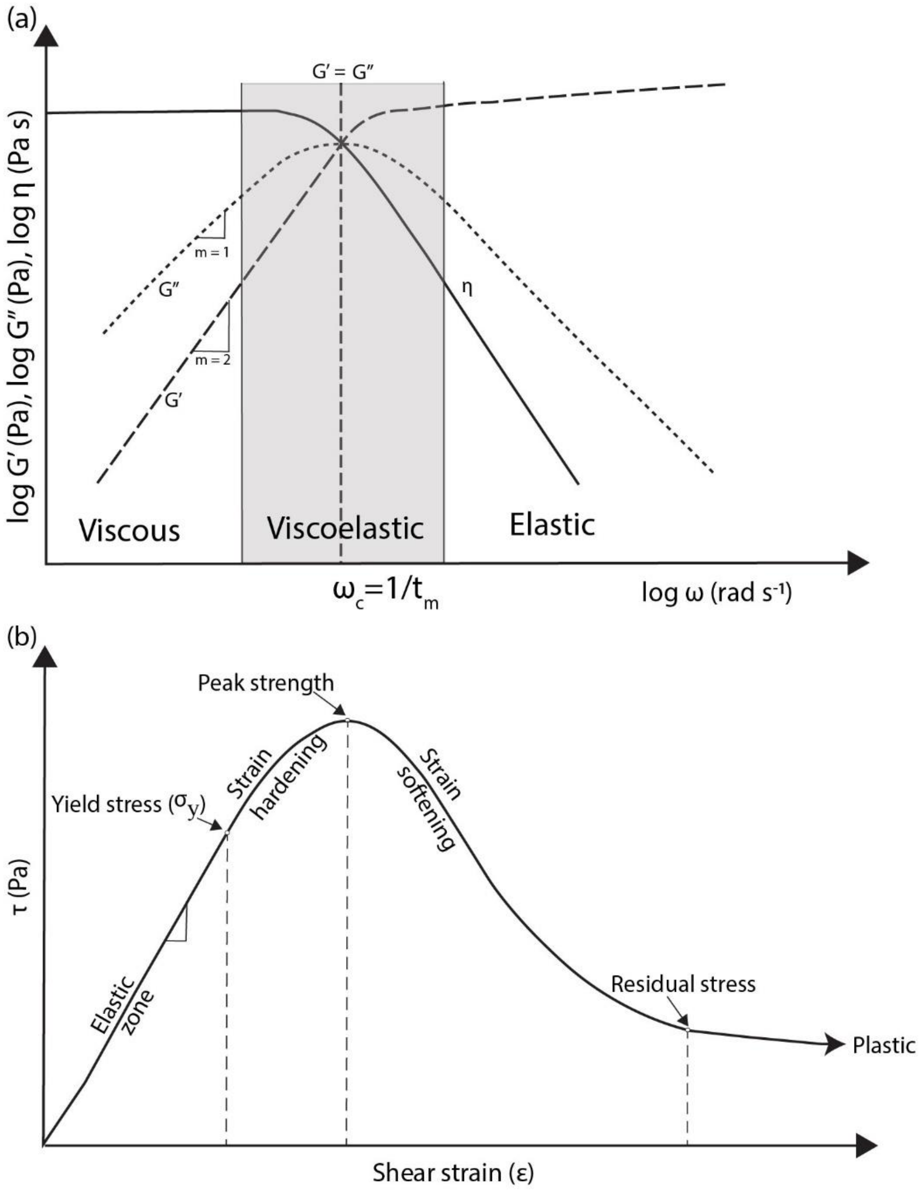

Figure 2.3. *(a) Typical rheological characterisation of an ideal linear viscoelastic material. Different fields indicate different mechanical behaviours, determined by the relation between storage (G') and loss moduli (G''). At lower frequencies (ω), dominantly viscous behaviour is characterised by G'' >> G' and the slopes of G'' and G' are 1 and 2 respectively. In this viscous region, the complex viscosity (η*) is constant and similar to the zero-shear viscosity (η_0). At higher frequencies, dominantly elastic behaviour is characterised by G' >> G'' and constant plateau of G'. Viscoelastic behaviour occurs at intermediate frequencies. The crossover point (ω_c) between G' and G'' determines the Maxwell relaxation time (t_m) of the material (modified from Di Giuseppe et al., 2009). (b) Ideal shear stress – shear strain behaviour of strain softening rocks (modified from Xue et al., 2017) depicting a transition from elastic to plastic behaviour with post yielding strain hardening and strain softening behaviours (see text for details).*

2.3.1.2. Plastic deformation

When the elastic limit is reached in most materials, strain is no longer proportional to the applied stress and atomic bonds start to break. When this occurs, the material can no longer return to its original structure and the deformation is permanent, known as plastic behaviour (Per et al., 1983; Irgens, 2008). The stress under which noticeable plastic deformation occurs is called the yield stress, τ_y. As the material deforms at stresses > τ_y, the corresponding strain is not recoverable (Fig. 2.3b).

2.3.1.3. Brittle elastic deformation

For complete characterisation of a material's properties it is also important to understand its behaviour at large strains and failure. At large strain, a material can fail by either forming brittle-elastic fractures or by permanent plastic flow. Brittle fractures are considered to originate in the elastic region at a critical stress (brittle strength), when all bonds between structural elements in a macroscopic plane within the material break. This results in failure of the structure of the material at larger scale and a sudden drop in stress (Di Giuseppe et al., 2009).

2.3.1.4. Rheological models

Common rheological models (Fig. 2.4) used to explain viscoelastic behaviours comprise a linear elastic component represented by a spring and a Newtonian viscous component represented by a dashpot. They can either be in series (Maxwell model; Fig. 2.4d) or in parallel (Kelvin-Voigt model; Fig. 2.4c) (Barnes et al.,1989; Chhabra, 2010). The viscosity to modulus of rigidity ratio (η/G) defines the Maxwell relaxation time (t_m) (Bailey, 2006; Chhabra, 2010) in the Maxwell model, and the retardation time (t_{kv}) in the Kelvin-Voigt model. After the application of a load, a Maxwell element will accumulate permanent viscous deformation over time, whereas a Kelvin-Voigt material will return to its undeformed state. However, both the Maxwell and Kelvin-Voigt models can be used to represent either the short-term, long-term or transient creep behaviour of a material, but not all of them together. To overcome this shortcoming, a Burgers model, which has Maxwell and Kelvin-Voigt elements in series, is commonly used to account for the steady-state creep behaviour of many materials (Fig. 2.4h).

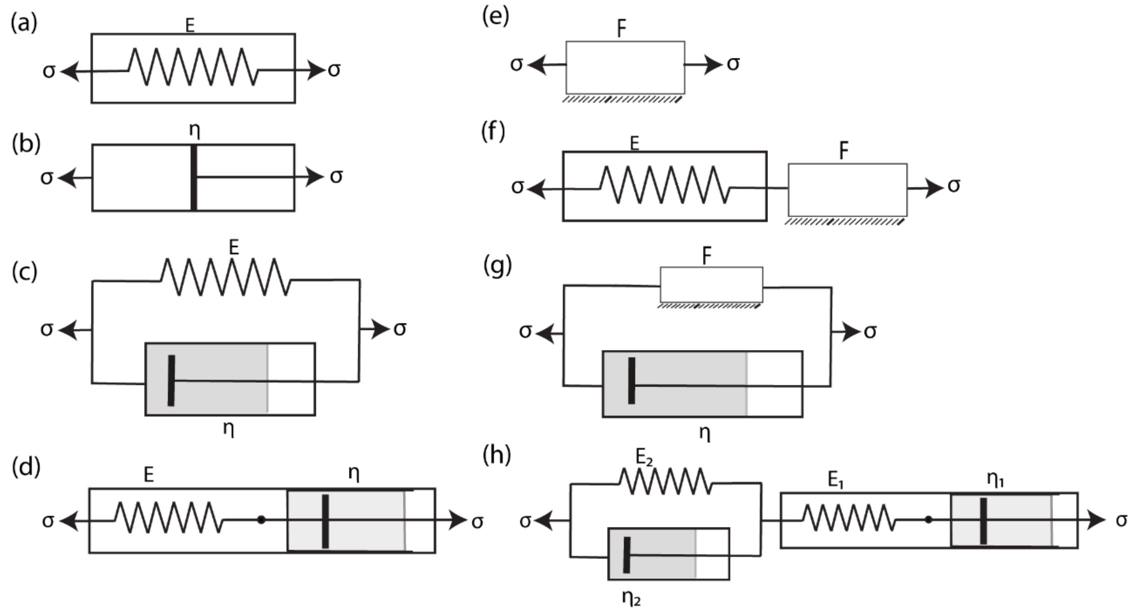

Figure 2.4. *Representation of basic rheological models. (a) Linear elastic (spring), (b) Linear viscous (dashpot), (c) Kelvin – Voight model (Visco-elastic), (d) Maxwell model (Visco-elastic), (e) Perfectly plastic (frictional element), (f) Linearly elastic- perfectly plastic model, (g) Bingham-Maxwell (Visco-plastic) model and (h) Burgers model.*

Perfectly plastic behaviour is modelled using a frictional element with a yield stress below which no strain occurs, analogous to a rigid block sliding on a rough surface (Fig. 2.4e). Rheological models for elastic-plastic behaviour (Fig. 2.4f) are made up of a spring and frictional element in series (Barnes et al., 1989; Irgens, 2008). This model behaves ideally elastic for stresses below the yield stress, τ_y, and perfectly plastic at stresses above τ_y. Visco-plastic rheological models (Fig. 2.4g) have a dashpot in parallel with a frictional element, also known as a Bingham plastic. When the applied stress in such a material is < τ_y, no deformation is possible; at higher stresses the material flows linearly.

3.3.2 Rheological testing methods

Samples of LRD were subjected to a series of rheological tests performed using an Anton Paar Physica MCR 301 rheometer. A flat parallel-plate geometry (Fig. 2.5) with 1 mm gap was used, and the instrument and measurement accuracy are < 0.1 % and 5 %, respectively (Di Giuseppe et al., 2009). After the desired curing time, a carefully sliced sample was placed on the bottom plate of the rheometer and the top plate was lowered slowly onto it. To minimise possible alterations of the structure of the sample during loading the sample was left for about 30 minutes between the parallel plates before starting the measurements. To control the effects of temperature and evaporation on the sample, the parallel plate measuring system was coupled with a closed Peltier hood during measurements. Both oscillation (a.k.a. dynamic) and rotational testing methods were used to impose shear stresses, shear strains and shear strain rates on the samples and to measure dynamic moduli and shear strength of the material, respectively. All tests were performed under constant zero normal stress from the upper plate. The shear strain, shear stress and shear strain rate are controlled by changing the angular displacement (amplitude), torque and angular velocity of the upper plate of the rheometer, respectively. Shear strain rate in oscillation tests is also controlled by varying the oscillation frequency, ω. In order to evaluate the reproducibility of the measurements and assess for possible rheometer plate slip effects, three separate tests were conducted on each LRD concentration, and signs of any detachment of the sample from the parallel plates were carefully assessed after each measurement. Moreover, we carefully compared our amplitude sweep and frequency sweep test results with those of Mourchid et al. (1998) and Morariu and Bercea (2011). We consistently found that the results for the three repeated tests for each sample were reproducible and very similar to previous studies, indicating that rheometer plate slippage is unlikely to have occurred. The following section provides a brief outline of each test method and its significance.

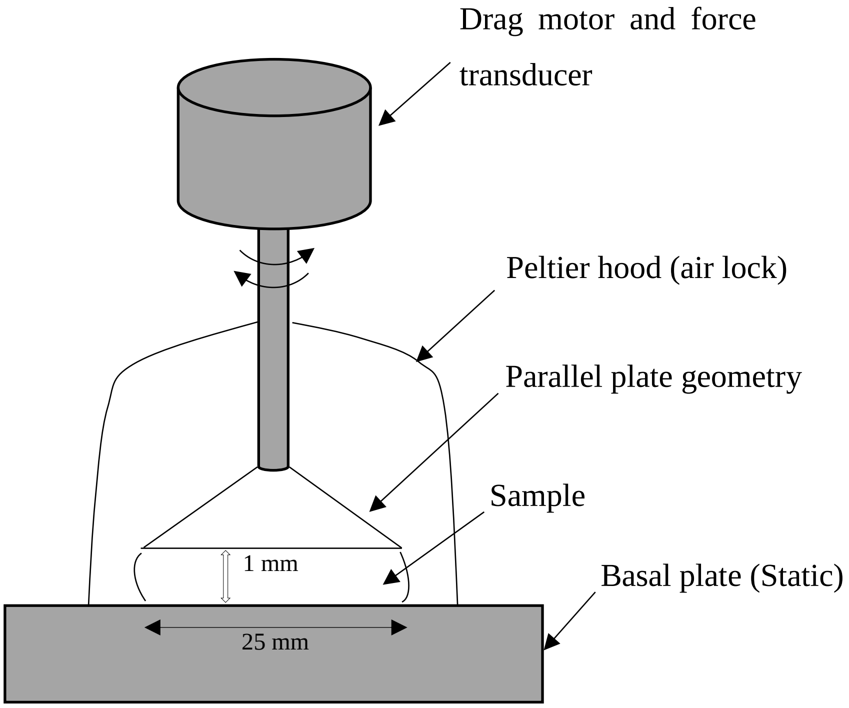

Figure 2.5. *Schematic diagram of a rheometer with a parallel-plate setup used for oscillation and rotational tests.*

2.3.2.1 Oscillatory tests

Oscillatory amplitude sweep tests were used to determine the linear viscoelastic range of LRD in its gel state. In these tests, the shear strain applied to samples of different concentration was varied from 0.01 to 100 % while the oscillation frequency and temperature were kept constant ($\omega = 0.1\ s^{-1}$, T = 22.5 °C; curing time = 3 days; See Table 2.1 for details of measurements). The linear viscoelastic range (Fig. 2.6) is defined as the region where the dynamic moduli have constant values over a range of imposed shear strain values below a shear strain threshold (γ_c). When γ_c is exceeded, the dynamic moduli either increase (G″; viscous component) or decrease (G′; elastic component) and the material behaviour becomes strain-dependent or non-linear. Furthermore, Brizzi et al. (2016) have shown that in amplitude sweep tests, constant plateau values of G′ and G″ reflect an equilibrium stage during which the structure of the material does not alter. Amplitude sweep results (Fig. 2.7) in our study show similar behaviour and provide further evidence that the structure of the material did not change during sample loading.

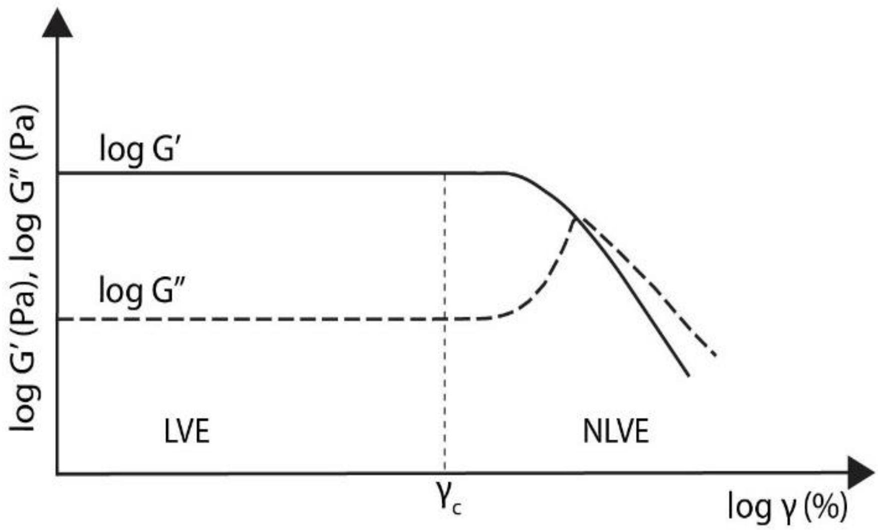

Figure 2.6. *Typical rheological behaviour of viscoelastic (VE) samples from oscillatory tests - here an amplitude sweep test for variable strain, γ (ω constant). Values of log G' and log G" show constant plateau values independent of strain amplitude (γ) in the linear viscoelastic (LVE) region, in which the structure of the sample is stable. Non-linear viscoelastic (NLVE) behaviour occurs above a critical shear strain (y_c). In this region the sample structure has been either irreversibly changed or destroyed.*

The frequency or shear strain-rate dependence of a material is characterised using *frequency sweep tests* (Fig. 2.3a), during which the oscillation frequency is varied between 0.01 to 100 s^{-1} while the shear strain and temperature are held constant (γ = 1%, T = 22.5 °C). In order to remain in the linear viscoelastic domain, shear strain in this test was kept below γ_c determined by amplitude sweep tests. The resulting values of G′ and G″ were used to calculate the complex shear modulus from Eqn. 3. The complex Young's modulus was calculated from Eqn. 4, assuming LRD is incompressible with a Poisson ratio ν = 0.5. This assumption is reasonable because LRD is similar to the natural clay mineral Hectorite, and for most saturated clays reported Poisson ratios are close to 0.5. Further, the Maxwell relaxation time of the material can be determined from the frequency where the G′ and G″ curves cross each other (Fig. 2.3a).

In order to identify the effects of temperature on LRD, *temperature sweep tests* were performed by applying a slow heating rate (2 °C per minute) to the sample from 20 to 50 °C. For each 2 °C step the measurement duration was 1.07 min, during which the shear strain and oscillation frequency were kept constant within the linear viscoelastic range to ensure reproducibility of the results.

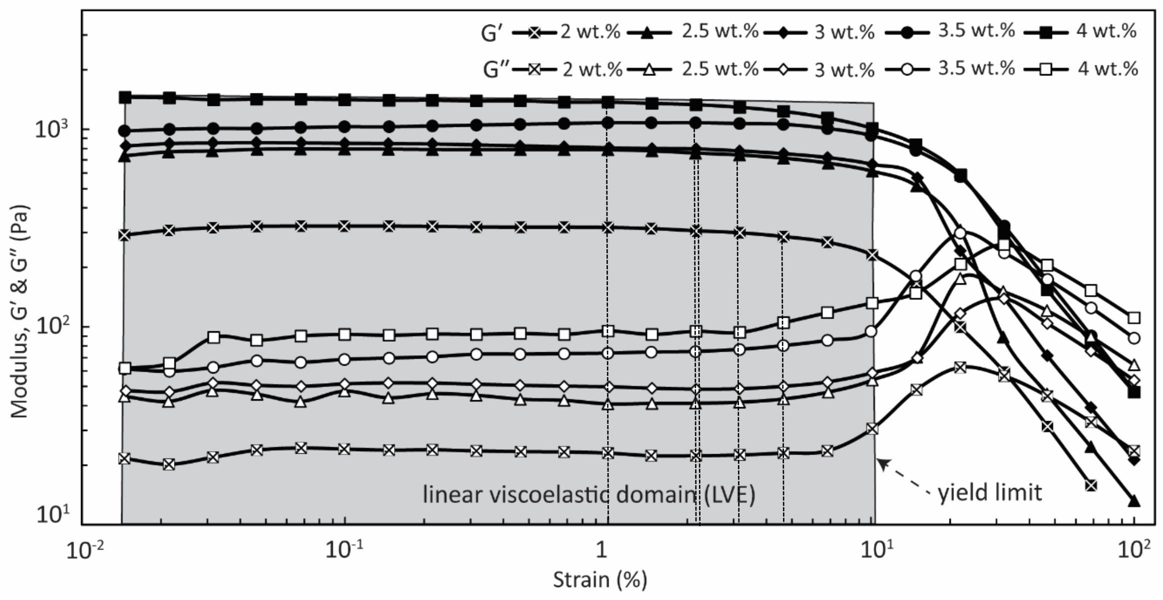

Figure 2.7. *Results from amplitude sweep tests showing variation of storage (G') and loss (G") moduli for Laponite RD with different wt. % concentrations and curing time of 3 days. Strain was varied from 0.01 % to 100 % at a constant strain rate (0.1 s^{-1}). The grey field (LVE domain) marks the values of the strain amplitude where the dynamic moduli, G' and G" remain nearly constant. The critical shear strains (γ_c) at which G' and G" start to change by 1 % from their constant plateau values are indicated by dotted lines for each concentration. The rapid change where G' and G" start to change by 15 % in between two adjacent measurements is considered here to define the yield limit.*

2.3.2.2 Rotational tests

The shear strength of LRD samples was measured using *rotational shear strength tests*, in which samples were deformed by imposing a shear strain up to 500 % at constant strain rate and temperature (0.1 s^{-1} and 22.5 °C). Shear stress of the material was recorded as a function of strain. The maximum shear stress here defines the shear strength or peak strength of the material.

Finally, *transient creep and recovery* tests were performed to measure the creep and recovery responses during the deformation of the material. A constant shear stress (τ = 70 Pa) was imposed on the sample for a pre-set time period (1210 s), and the shear stress was then removed abruptly (τ = 0 Pa) and the recovery of shear strain in the material was recorded over time. The initial constant shear stress value was selected based on the results of the amplitude and frequency sweep tests to ensure that the applied shear stress was within the linear viscoelastic region of the material.

Table 2.1. *Critical strain (γ_c) and corresponding G′ and G″ values for different concentrations (X wt. %) of Laponite RD® (curing time – 3 days) from amplitude sweep tests.*

X (wt. %)	γ_c (%)	G′ (Pa)	G″ (Pa)
2	4.65	286	23
2.5	3.16	740	41.60
3	2.16	796	48
3.5	2.15	1080	75
4	1	1370	95.40

2.4. Results

2.4.1. Amplitude sweep tests

The dynamic moduli of LRD mixtures (curing time = 3 days) determined by oscillatory amplitude sweep tests are presented in Table 2.1 and Figure 2.7. All concentrations of LRD are in the linear viscoelastic domain with constant G′ and G″ for shear strain amplitudes γ < 10 %. The critical shear strain, γ_c, under which the material is in the linear viscoelastic region decreases with increasing concentration (Table 2.1; Fig. 2.7 - dotted lines). This γ_c was considered as the point at which moduli values (G′ and G″) change by 1 % from their constant plateau values (van Otterloo and Cruden, 2016). The shear strain amplitude at which G′ and G″ change rapidly by 15 % between two adjacent measurements is considered to be the yield limit

(γ_L= 10 %). At this point, the material transitions from an effectively elastic regime to an effectively plastic regime. As shear strain increases above $\gamma_{L,}$ G′ decreases and G″ increases rapidly until elastic and viscous forces exactly balance at G′ = G″ (Di Giuseppe et al., 2009). This occurs at shear strains of 26 % and 46.9 % for 2 wt. % and 4 wt. % concentrations, respectively (Fig. 2.7).

2.4.2. Frequency sweep tests

The results of the frequency sweep tests are presented in Table 2.2 and the dependence of G′ and G″ on frequency in the viscoelastic regime is shown in Fig 2.8a. G′ is approximately constant for all LRD samples over the full range of frequencies tested and the corresponding value of G″ drops as frequency is increased. However, G′ dominates over G″ by more than one order of magnitude within this frequency range. Both the dynamic moduli (G′, G″) and the complex shear (G*) and Young's (E*) moduli calculated using Equations 3 and 5 increase with the concentration of LRD and the sample age (Table 2.2; Fig. 2.8b).

Table 2.2. *Results of frequency sweep tests applied to different concentrations and curing times of Laponite RD®. The complex viscosity, η*, is the average value for the range of frequencies at which G′ and G″ were measured.*

X (wt. %)	G′ (Pa)	G″ (Pa)	G* (Pa)	E* (Pa)	η* (Pa s)
3 days					
2	3.48×10^2	1.90×10^1	3.49×10^2	1.05×10^3	1.38×10^2
2.5	8.01×10^2	3.40×10^1	8.02×10^2	2.41×10^3	3.31×10^2
3	1.34×10^3	5.90×10^1	1.34×10^3	4.02×10^3	5.49×10^2
3.5	1.83×10^3	7.10×10^1	1.83×10^3	5.49×10^3	7.56×10^2
4	1.92×10^3	8.00×10^1	1.92×10^3	5.77×10^3	7.89×10^2
7 days					
2	4.05×10^2	2.00×10^1	4.05×10^2	1.22×10^3	1.64×10^2
2.5	7.77×10^2	3.58×10^1	7.78×10^2	2.33×10^3	3.20×10^2
3	1.67×10^3	6.60×10^1	1.67×10^3	5.01×10^3	6.88×10^2
3.5	2.77×10^3	1.16×10^2	2.77×10^3	8.32×10^3	1.86×10^2
4	3.84×10^3	1.73×10^2	3.42×10^3	1.03×10^4	1.88×10^2
14 days					
2	5.01×10^2	2.50×10^1	5.02×10^2	1.50×10^3	2.04×10^2
2.5	7.85×10^2	3.30×10^1	7.86×10^2	2.36×10^3	3.25×10^2
3	1.86×10^3	7.90×10^1	1.86×10^3	5.59×10^3	7.75×10^2
3.5	3.23×10^3	1.49×10^2	3.23×10^3	9.70×10^3	1.35×10^3
4	3.92×10^3	1.82×10^2	3.92×10^3	1.18×10^4	1.77×10^4

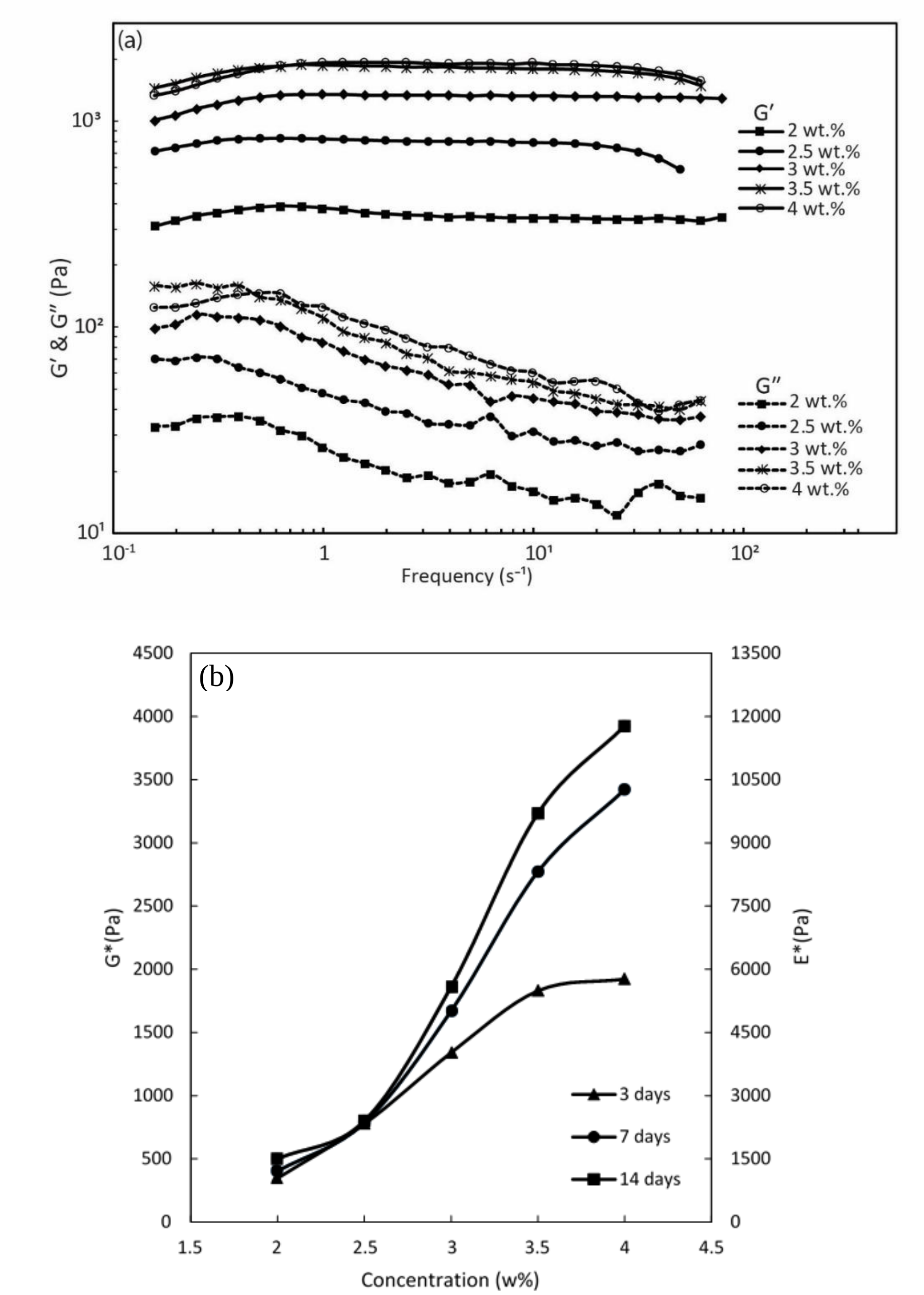

Figure 2.8. *Results from frequency sweep tests of Laponite RD® showing the frequency dependence of dynamic moduli (a) Variations of storage, G', and loss moduli , G", values in the LVE domain (γ < 1%) with change in frequency from 0.1 s^{-1} to 100 s^{-1}. (b) Calculated complex shear, G*, and Young's, E*, moduli values within the LVE domain for different Laponite RD® concentrations and curing (aging) times.*

2.4.3. Temperature sweep tests

The effective viscosity, η, of LRD mixtures measured at a slow heating rate of 2 °C per minute at constant shear strain rates, $\dot{\gamma}$, varies by 4 orders of magnitude as $\dot{\gamma}$ is increased from 0.01 s^{-1} (Fig. 2.9a) to 50 s^{-1} (Fig. 2.9b). The effective viscosity is nearly independent of temperature between 20 °C and 50 °C for LRD concentrations up to 2.5 wt.% for $\dot{\gamma}$ = 0.01 s^{-1} (Fig. 2.9a) and up to 3 wt.% for $\dot{\gamma}$ = 50 s^{-1}. Above these concentrations, the effective viscosity decreases significantly with increasing temperature at both strain rates. This decrease is greatest during the first few initial temperature increments for higher LRD concentrations (> 3.5 wt. %).

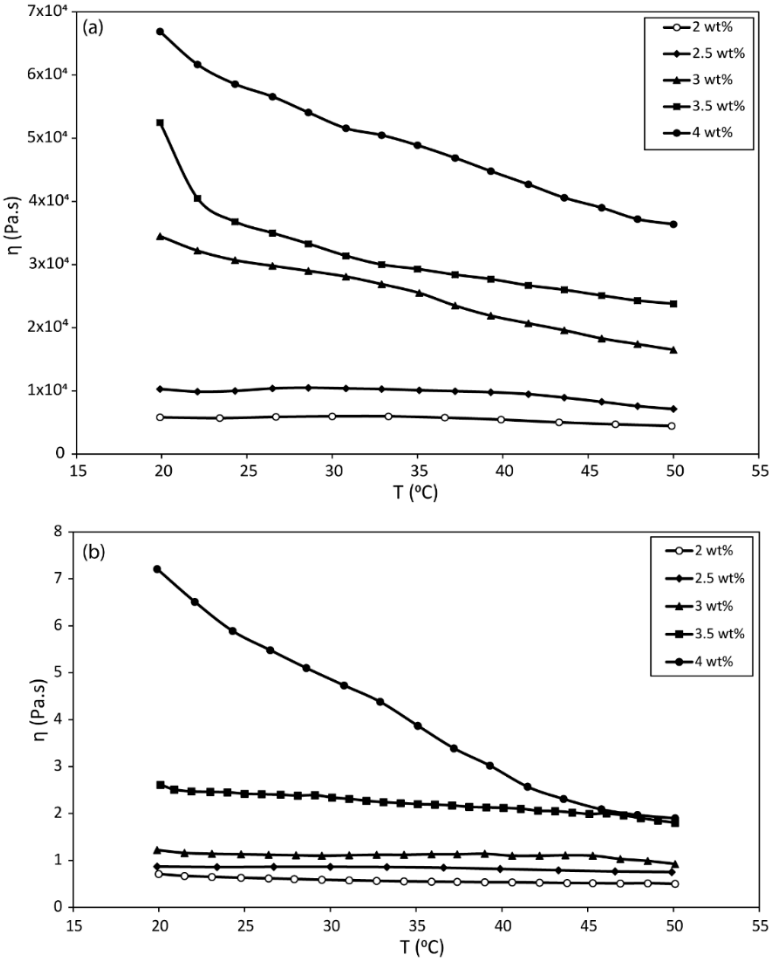

Figure 2.9. *Temperature dependence of viscosity for different concentrations of Laponite RD. Strain rate is constant at 0.01s^{-1} (a) and 50 s^{-1} (b). Note that the effective viscosity of LRD at low concentrations is not sensitive to temperature for both lower and higher strain rates. The effective viscosity does not vary at higher strain rate for all concentrations except 4 wt. %.*

2.4.4. Rotational strength tests

Results of the rotational strength tests are presented in Table 2.3 and Figure 2.10. The stress-strain curves show that there is a strength increase with longer curing times (compare Fig. 2.10a and b). All concentrations show a linear viscoelastic response up to shear strain values of 10 % (i.e. the yield strength or limit) followed by a phase of strain hardening until a peak strength, τ_m (Pa), is reached when $\gamma > 15$ - 20 % (Fig. 2.10c). The peak strength value in Fig. 2.10, increases with LRD concentration and age (Fig. 2.11), while the corresponding shear strain is roughly constant. A decrease in shear stress values at strains beyond the peak stress indicates a phase of strain softening (Fig. 2.10c). Shear stresses eventually reach constant values at high shear strains, corresponding to plastic deformation. The shear strength, τ_m (Pa) of different LRD concentrations is characterised by an empirical linear relationship with the sample age given in Fig. 2.11b.

Table 2.3. *Results of rotational strength tests and the corresponding maximum shear strength (τ_m) and shear strain (γ) for different sample ages and Laponite RD concentrations.*

X	**3 days**		**7 days**		**14 days**	
(wt. %)	γ (%)	τ_m (Pa)	γ(%)	τ_m (Pa)	γ (%)	τ_m (Pa)
2	20.2	26	20.2	40	20.2	59
2.5	20.2	37.2	15.2	55	15.2	84
3	15.2	103	15.2	143	15.2	183
3.5	20.2	150	15.2	223	15.2	238
4	20.2	194	15.2	258	15.2	385

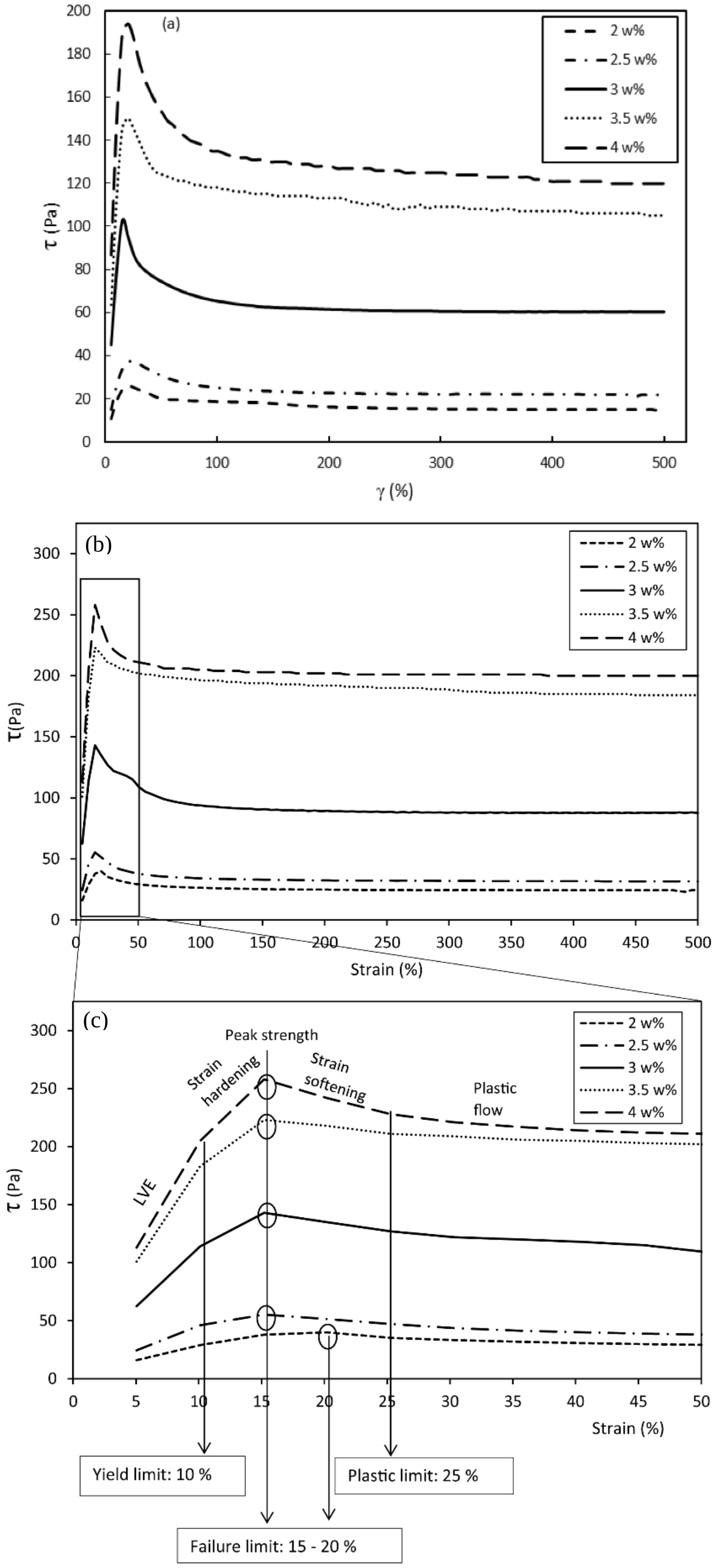

Figure 2.10. *Rotational strength test results for different Laponite RD® concentrations showing shear stress variation for shear strains up to 500%. Strain rate is constant at 0.1 s^{-1}. The curing time varies from (a) 3 days to (b) 7 days. (c) Interpreted section of the lower shear strain region of (b).*

2.4.5. Creep and recovery test

Results of the creep and recovery test for 4 wt. % LRD are presented in Fig. 2.12. During stress loading (τ = 70 Pa) at t = 0 s, shear strain (γ_0) increases instantaneously up to 0.0303 %. Then it shows a time dependent increase in viscoelastic (γ_{VE}) and visco-plastic (γ_{VP}) shear strain up to 0.0702 % when the shear stress is removed instantaneously (t = 1150 s). When the shear stress is removed, the recovery stage is characterized by an instantaneous drop in shear strain from 0.0702 % to 0.0454 %, corresponding to the elastic recovery (γ_E = 0.0248 %) of the sample. This elastic recovery is different from the initial instantaneous strain (γ_0 = 0.0303 %). The (γ_0 - γ_E) discrepancy is therefore considered to record an instantaneous time independent perfectly plastic strain, γ_P (Perl et al., 1983). After this, the material undergoes a period of time dependent, recoverable viscoelastic strain (γ_{VE}). During this recovery period between t = 1150 and 3840 s the shear strain decays, reaching a permanent, time independent shear strain ($\gamma_{VP} + \gamma_P$) of 0.0242 %. Results from the creep and recovery tests for different LRD concentrations (Table 5) at constant curing time (3 days) show a drop of the initial instantaneous strain, γ_0 from 0.0303 to 0.0228 % as concentration decreases from 4 to 3 wt. %, respectively. Moreover, as concentration is lowered, the values of γ_E and γ_{VP} decrease and the time independent plastic strain (γ_P) increases from 0.0055 to 0.0074 %. Similar shear strain ($\gamma_{E,}$ $\gamma_{VE,}$ γ_{VP} and γ_P) values are obtained for each concentration during the creep and recovery phases (see Table 4).

The shear strain versus time curve from this test shows the creep and recovery phases of the material, which are subdivided into different regions, representing characteristic mechanical behaviours of the sample. The creep phase has three distinct regions: (I) an initial instantaneous and time independent, elastic and perfectly plastic increase in shear strain in response to the applied instantaneous stress; (II) a secondary time-dependent viscoelastic response that will eventually be recovered when the stress is removed; and (III) a tertiary non-recoverable visco-plastic deformation. The recovery phase mirrors the same regions: an elastic recovery of the material due to the removal of the applied stress; delayed time-dependant viscoelastic recovery and a final non-recoverable component of permanent visco-plastic and plastic deformation, attributed to the visco-plastic response of the material.

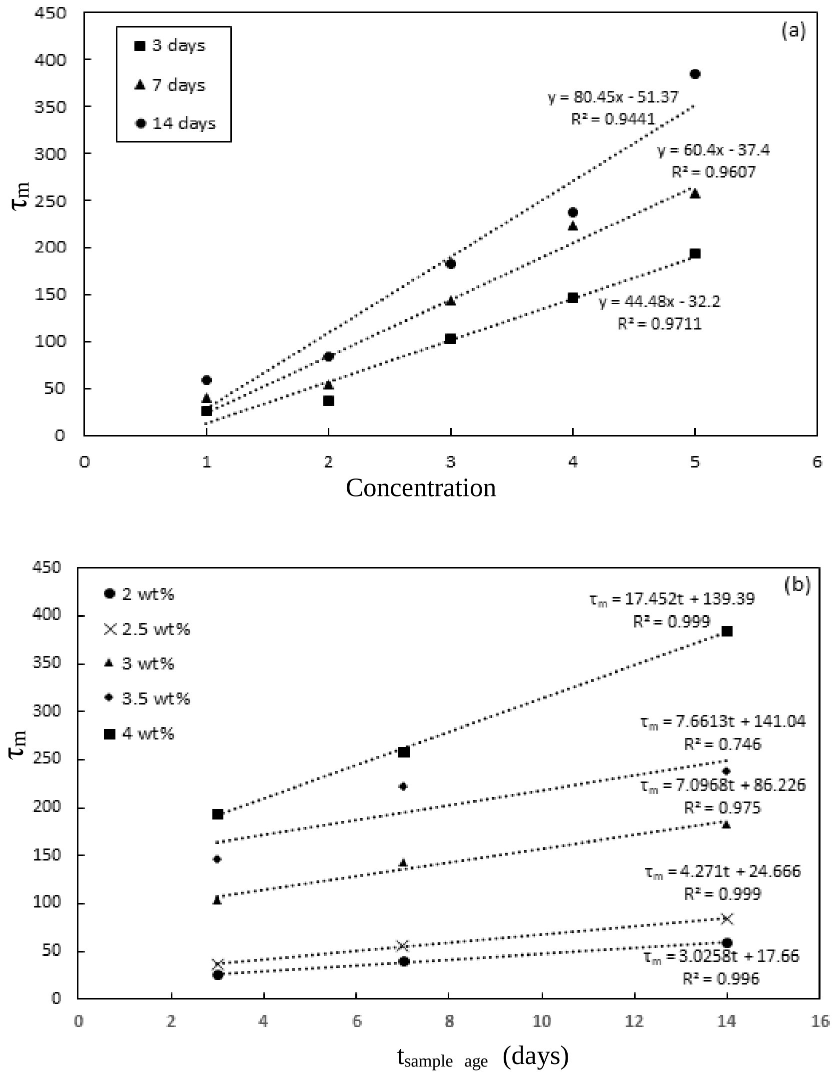

Figure 2.11. *(a) Maximum shear stress (i.e. shear strength, τ_m) versus Laponite RD® concentrations for different curing times ($t_{sample\ age}$). (b) Shear strength versus curing time for each Laponite RD® concentration.*

Table 2.4. *Shear strains under different mechanical regimes measured during creep and recovery phases for different LRD concentrations. Curing time is constant (3 days). See text for the definition of symbols.*

LRD	**Creep phase**					**Recovery phase**			
(wt. %)	γ_0	γ_E	γ_{VE}	γ_{VP}	γ_P	γ_E	γ_{VE}	γ_{VP}	γ_P
4	0.0303	0.0248	0.0214	0.0187	0.0055	0.0248	0.0214	0.0187	0.0055
3.5	0.0261	0.0194	0.0239	0.0097	0.0067	0.0194	0.0239	0.0097	0.0194
3	0.0228	0.0154	0.0255	0.0067	0.0074	0.0154	0.0255	0.0067	0.0074

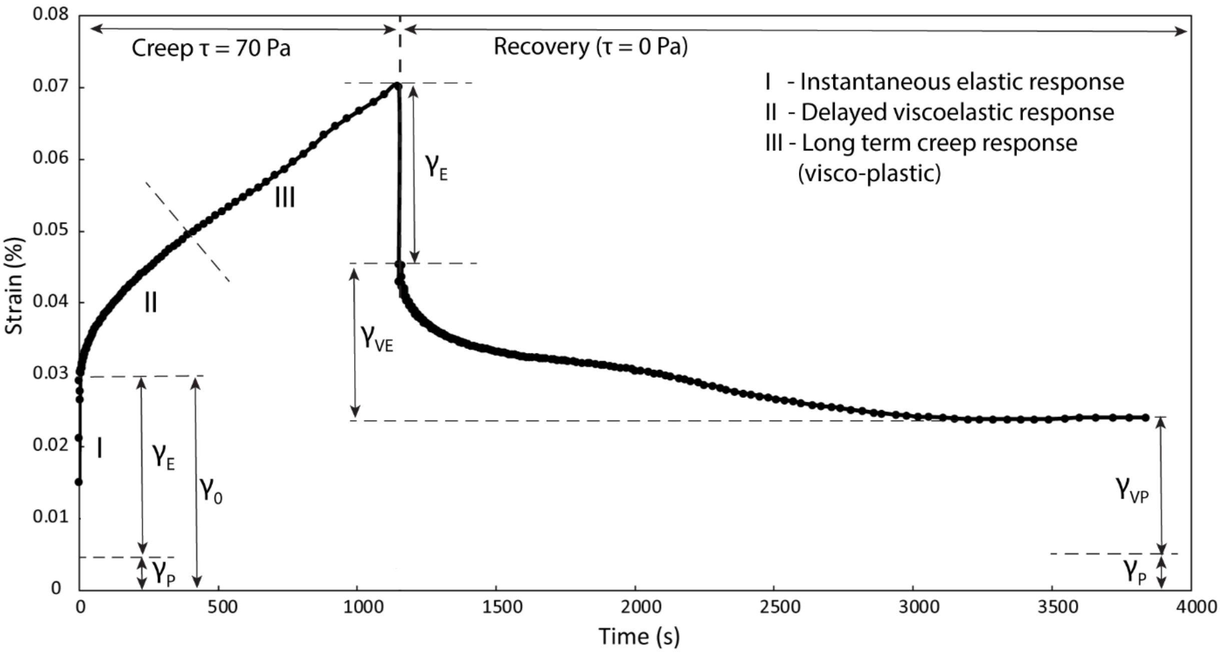

Figure 2.12. *Results of a creep and recovery test for 4 wt. % Laponite RD® after 3 days of curing. Creep lasted $t = 1150$ s at a shear stresses $\tau = 70$ Pa, after which the shear stress was set to 0 Pa and recovery started. Shear strains are marked as linear elastic (γ_E), perfectly plastic (γ_P), viscoelastic (γ_{VE}) and visco-plastic (γ_{VP}). γ_0 is the total instantaneous shear strain upon stress loading to $\tau = 70$ Pa.*

2.5. Discussion

We investigated the rheological properties of LRD in order to assess its suitability as a crustal analogue for use in analogue modelling experiments. Physical parameters such as concentration, temperature and ageing time have been considered to fully characterise its range of mechanical properties, discussed below.

2.5.1. Rheology of Laponite RD®

According to the rheological results presented above, LRD shows complex mechanical behaviours that vary from linear viscoelastic, non-linear viscoelastic, visco-plastic to plastic. The tests demonstrate that at low strains, characterisation of the linear and non-linear viscoelastic response of a material is important for predicting its deformation behaviour. As observed from the oscillatory tests, all measured concentrations of LRD in the gel state are viscoelastic (Figs. 2.7, 2.8). However, the linear viscoelastic region occurs below a critical strain amplitude, γ_c, which decreases from ~ 3% to ~ 1 % as concentration is increased from 2 to 4 wt. % (Table 2.1). In this LVE domain, the elastic storage modulus (G′) of LRD dominates over the loss modulus (G″), a measure of viscous dissipation, by two orders of magnitude (Fig. 2.7).

Beyond the critical shear strain that limits the LVE domain, the elastic properties of LRD decrease and its viscous properties become more important. Non-linear viscoelastic behaviour starts at this point, resulting in permanent deformation of the material. These behaviours can be explained by a Maxwell viscoelastic model (Fig. 2.4d), with a linear elastic component (spring) in series with a viscous component (dashpot). In this model the spring accommodates low amounts of recoverable elastic strain, and above γ_c permanent strain is accumulated in the viscous dashpot.

From the frequency sweep tests (Fig. 2.8) it is clear that, within the LVE domain, G′ is almost independent of the measured frequency range, except at very low frequencies (< 0.8 s^{-1}). At frequencies below 0.8 s^{-1}, G′ starts to decrease and G″ continuously increases. The Maxwell relaxation time (t_m), defined as the inverse frequency (i.e., $1/\omega = t_m$) at the crossover points of G′ and G″, could not be determined within the tested frequency range because such a crossover is not reached. Around the lowest frequency we could achieve (~2×10^{-1} s^{-1}, i.e., t = 5 s), G′ and G″ are still approaching each other. This places an upper bound on the Maxwell relaxation time of $t_m > 5$ s, which is higher than that of pig skin gelatine (0.3 – 1.5 s; van Otterloo and Cruden, 2016).

The storage (G′) and loss modulus (G″) values of LRD determined here (G′ = $6.28 \times 10^1 – 3.23 \times 10^3$ Pa and G″ = 29 – 295 Pa at $\omega = 10^{-1}$ s^{-1} – 10^2 s^{-1}) are very similar to measurements by Willenbacher (1996), Mourchid et al. (1998) and Morariu and Bercea (2011) which used cone and plate geometry. However, Willenbacher (1996) and Mourchid et al. (1998) used LRD samples with different ionic strengths by adding NaCl, and Morariu and Bercea (2011) tested aqueous solutions of polyethylene glycol (PEG) containing LRD.

2.5.2. Comparison of the rheological properties of Laponite RD® and gelatine

The G′ and G″ values of pig skin gelatine measured by frequency sweep tests (van Otterloo and Cruden, 2016) with a smaller frequency range ($\omega = 1 – 500$ s^{-1}) vary from 4.25×10^4 - 2.88×10^4 Pa (T = 5 – 20 °C, $\omega = 1 – 500$ s^{-1} and X = 1 - 10 wt.%) and 4.22 - 49.6 Pa respectively, which are similar to values for LRD. The storage and loss modulus values are also similar to those reported for pig skin gelatine by Di Giuseppe et al. (2009; G′ 1.76×10^1 - 2.15×10^3 Pa and G″ 0.3 – 23.4 Pa at T = 10 °C and X = 1- 4 wt. %) and Brizzi et al. (2016; G′ 4.64×10^1 – 7.23×10^2 Pa and G″ 1.37 – 14.1 Pa at T = 10 °C and X = 2.5 wt. %). However, Brizzi et al. (2016) used pig skin gelatine (2.5 wt. %) with different concentrations of NaCl, finding that, for the same gelatine concentration, G′ and G″ values decrease as the NaCl concentration increases. The maximum shear strain (γ_c) at which LRD deforms in the linear viscoelastic domain is similar to pig skin gelatine. In LRD γ_c is higher (> 2.16 %) for concentrations < 3 wt. % and lower for concentrations > 3 wt. % (see Table 2.1). In pig skin gelatine, γ_c is higher (10 % - 21.5 %) for lower concentrations < 3 wt.% and lower (3.16 %) for concentrations > 5 wt.% (van Otterloo and Cruden, 2016). However, γ_c values for pig skin gelatine are higher than those of LRD at similar concentrations. Hence, for similar concentrations, the critical shear strain (γ_c) of LRD is lower than that of gelatine.

The calculated Young's modulus values of LRD (1.05×10^3 - 1.18×10^4 Pa at T = 22. 5 °C) are similar to those reported for gelatine by Kavanagh et al. (2013; 4.4×10^3 - 1.5×10^4 Pa at T = 5 °C and X < 4 wt. %) and Van Otterloo and Cruden (2016; 10^3 - 10^4 Pa at T = 5 °C and X < 5 wt. %). The complex shear modulus values of LRD (3.49×10^2 - 3.92×10^3 Pa at T = 22. 5 °C) are also similar to those reported for pig skin gelatine (Van Otterloo and Cruden, 2016; 6.34×10^2 – 7.02×10^3 Pa at T = 5 °C and X = 3-10 wt. %).

The peak shear strength values of 4 wt.% LRD samples after 7 and 14 days of curing are 258 Pa and 385 Pa, respectively, similar to the those reported by Wallace and Rutherford (2015; 300 Pa and 360 Pa) who used a shear vane method to measure the peak undrained shear strength of LRD. The maximum shear strength values of gelatine (823 – 12,000 Pa at T = 5 °C, X = 1-4 wt. %) are one to two orders of magnitude higher than the LRD concentrations measured here (Van Otterloo and Cruden, 2016). Shear strain values corresponding to the peak strength of gelatine vary from 167 – 127 % as concentrations increase from 1 – 4 wt.% (Van Otterloo and Cruden, 2016), while the maximum peak strength shear strain values of the LRD concentrations measured here vary between 15 and 20 %.

2.5.3. Implications for the use of Laponite RD® as a rock analogue

Our results reveal that the stress-strain behaviour of all LRD concentrations changes from linear viscoelastic to plastic, after undergoing a sequence of yielding, strain hardening, peak strength and strain softening processes (Fig. 2.10), similar to the low temperature stress-strain behaviour of natural rocks under confining pressure (Giuseppe et al., 2009). At shear strain rates of 0.01 s^{-1} and shear strain amplitudes γ < 10 %, all LRD concentrations behave predominantly elastically and can therefore be used to model brittle elastic deformation of rocks with different mechanical properties (e.g., Young's modulus). These properties will depend on the concentration of LRD and the curing time (Equations 6 -10). At shear strain rates of 0.1 s^{-1} and strain amplitudes γ > 26.2 %, LRD can be used to model plastic deformation of rocks (Fig. 2.10c).

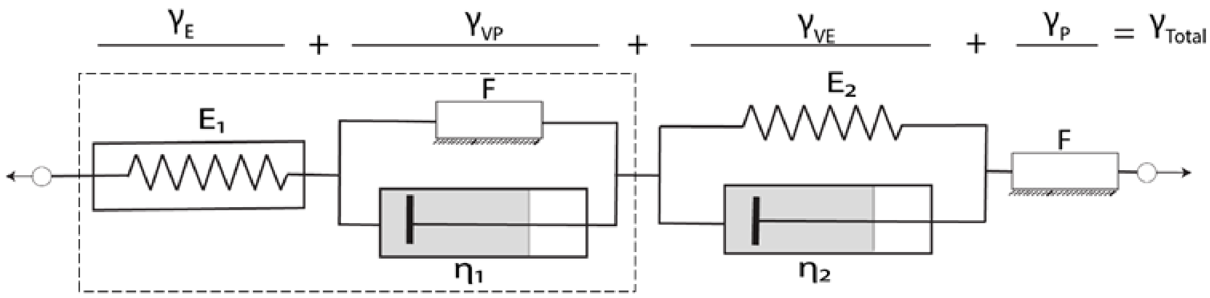

Figure 2.13. *Rheological model of Laponite RD based on creep and recovery tests (Fig. 2.12) and other rheological analyses. A Bingham - Maxwell model (E_1, η_1 and F; outlined in dotted line box) and Kelvin-Voigt (E_2, η_2) units are in series with an additional frictional element (F).*

Figure 2.13 presents a rheological model for 2 – 4 wt. % concentrations of LRD based on the various test results reported here. LRD is best described as combining a Bingham-Maxwell (elasto-visco-plastic) model and a Kelvin-Voight (viscoelastic) model in series with an additional frictional element. This behaviour is linked to the creep and recovery test results in Fig. 2.12. During the initial stress loading, the instantaneous and time independent elastic (γ_E) and plastic strains (γ_P) in region I are represented by the E_1 spring and the frictional element (F). The recoverable and time dependant viscoelastic (γ_{VE}; region II) behaviour is modelled by the Kelvin-Voigt viscoelastic element (E_2, η_2). The non-recoverable and time dependant visco-plastic (γ_{VP}; region III) response of LRD during the steady state creep phase is described by dashpot (η_1) and plastic (F) elements are in parallel. This creep and recovery behaviour is similar to a Burgers model (see Fig. 2.4h). However, a Burgers model only accounts for the instantaneous elastic strain component, not the instantaneous plastic strain component observed in our creep and recovery tests (Fig. 2.12).

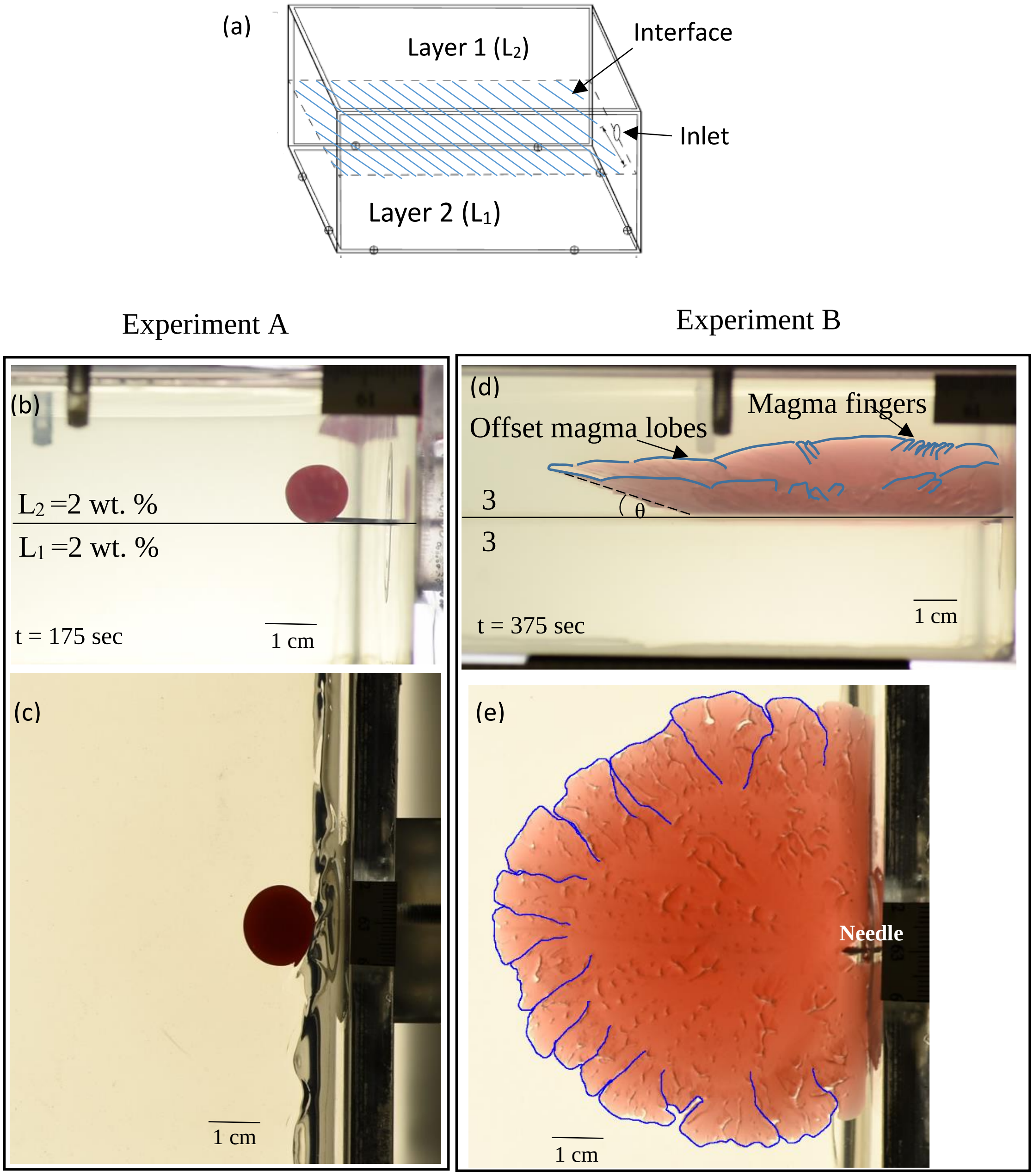

Figure 2.14. *Magma intrusion experiments in which analogue magma (paraffin oil) is injected, via a needle and peristaltic pump, into LRD with different concentrations. Experimental set up (a) and results of experiment A (b, c) and B (d, e). Magma and host rock analogues are paraffin oil (red colour) and LRD (pale yellow colour) respectively. (b) side and (c) overhead view of experiment A with 2 wt.% LRD in both layers. (d) side and (e) overhead view of experiment B with 3 wt.% LRD layers. In experiment B (d, e), blue lines are traces of tip propagation geometries and θ (~25°) is the angle of the inclined sheet that formed at later stages. In (d) and (e) the intrusion formed a saucer-shaped sill, where the originally flat sill expanded along the L_1/L_2 interface until the tip changed orientation and propagated upwards forming a saucer-shape.*

Table 2.5. *Experimental variables and their corresponding values in nature.*

Parameter	Dimension	Definition	Value		
			Nature (n)	Model (m)	Ratio*(m/n)
ρ_h	Kg m^{-3}	Host rock density	2800	1000	0.357
ρ_i	Kg m^{-3}	Intrusion (magma) density	2700	850	0.3
g	m s^{-2}	Gravity acceleration	9.81	9.81	1
V_i	m s^{-1}	Intrusion velocity	0.2	10^{-3}	5×10^{-3}
L	m	Length	100	0.01	10^{-4}
t	s	Time	-	900-2700	$2 \cdot 10^{-2}$
μ	Pa s	Magma viscosity	2.2×10^5	0.16	7.14×10^{-7}
Q_i	m^3 s^{-1}	Intrusion volumetric flow rate	(0.02 - 13.28)	1.66×10^{-9}	(6.25×10^{-10} - 3.75×10^{-7})

Scaling factors: model/nature	**$L^* = 10^{-4}$; $\rho^* = 0.357$; $g^* = 1$**
Stress scaling factor	**$\sigma^* = \rho^* g^* L = 3.57 \times 10^{-5}$** Model is 10^5 times weaker than in nature
Time scaling factor	**$t^* = L^*/V^* = 2 \times 10^{-2}$** 1 min in model ~0.83 hr in nature
Viscosity scaling factor	**$\mu^* = t^* \sigma^* \rightarrow \mu^* = 7.14 \times 10^{-7}$** Intrusion liquid represents magma with viscosity ~10^4 Pa s
Volumetric flow rate scaling factor	**$Q^* = \Delta\rho^* L^{*3} E^{*-1} V^* = (6.25 \times 10^{-10} - 3.75 \times 10^{-7})$** Experimental volumetric flow rate scales to 0.02 – 13.28 m^{3}s^{-1} in nature

2.5.4. Application to magma intrusion experiments

Different types of gels are commonly used as crack formation and propagation media to model sill and dyke emplacement in laboratory experiments (Kavanagh et al., 2006; Bertelsen et al., 2018b). Here we present two examples of how different concentrations of LRD may be used as crustal analogues for magma intrusion experiments. The experimental setup (Fig. 2.14a) is designed to facilitate lateral emplacement of sills at different crustal levels. Two layers (L_1 - bottom, L_2 - top) of LRD with the same concentration were placed into an open-topped plexiglass tank (30 cm x 30 cm x 6 cm) approximately one hour after each other. The top layer solution was slowly poured through a tube along the walls of the tank to avoid any impact on the interface. Both the bottom and top layers at the time of pouring were at room temperature (22.5 °C). Therefore, temperature differences between the layers will have a negligible influence on the interface strength. This is further supported by temperature sweep test results (Fig. 2.9a, b), where the effective viscosity of LRD is either independent or varies only slightly

(LRD 4wt. %) within a temperature range of 20 – 50 °C. Room temperature paraffin oil BP (Newtonian viscous; density = 0.85 g/cm^3) was then injected horizontally into the interface between the LRD layers via a nozzle at the side of the tank, fed by a peristaltic pump at a controlled flow rate (1 ml/min).

2.5.4.1. Scaling of magma intrusion experiments

We scaled our experiments to nature (Table 2.5) using the methods developed by Hubbert (1937) and Ramberg (1982), and used by Merle and Borgia (1996), Mathieu et al. (2008) and Galland et al. (2009). The principle is to define scaling factors and dimensionless numbers for the model, which simulates similar geometric, kinematic and dynamic processes in nature.

We have defined the length scaling factor (L*) as the ratio of the final length of a sill in the experiment (l_m) to the length of a sill in the shallow crust (l_p). In our case $L^* = l_m/l_p = 10^{-4}$ (1 cm represents 100 m). The density scaling factor ρ* = 0.357 is the ratio between the density of LRD in the experiments and natural sedimentary host rocks, and the gravitational acceleration scaling factor g* = 1. This gives a stress scaling factor

$$\sigma^* = \rho^* g^* L^* = 3.57 \times 10^{-5} \tag{2.5}$$

Natural magma intrusion velocities range from 0.1 m s^{-1} to 0.5 m s^{-1} (Spence and Turcotte, 1985; Kavanagh et al., 2013). Taking a lower intrusion velocity of 0.2 m s^{-1} and the average model intrusion velocity in our experiments of ~$1 \cdot 10^{-3}$ m s^{-1} gives a velocity scaling factor, $V^* = 5 \times 10^{-3}$. We can now define the time scaling factor as

$$t^* = L^*/V^* = 2 \times 10^{-2} \tag{2.6}$$

Using σ* and t*, the viscosity scaling factor is

$$\mu^* = t^* \sigma^* = 7.14 \cdot 10^{-7} \tag{2.7}$$

To scale the volumetric flow rate of the intruding magma we consider the density difference (Δρ*) and Young's modulus (E*) ratios. Firstly, Δρ* ~ 1.5 is calculated using the ratio of the density differences between the host rock and the magma in the model and nature (Table 2.1). The Young's modulus measured for LRD concentrations used in the experiment after 7 days curing time is in the range 10^3 - 10^4 Pa. Young's moduli for upper crustal rocks ranges from 10^9 to 10^{10} Pa (Kavanagh et al., 2013), so E* in our study is in the range 10^{-7} – 10^{-5} Pa.

Using $\Delta\rho^*$, L^*, $V^*$and E^* we can define the volumetric flow rate ratio:

$$Q^* = \Delta\rho^* L^{*3} E^{*-1} V^* = 6.25 \times 10^{-10} - 3.75 \times 10^{-7} \tag{2.8}$$

Therefore, our experiments represent host rocks that are ~$10^5 – 10^7$ times weaker than nature, and 1 min in our models represents 0.83 hrs in nature. The intruding liquid in the experiments corresponds to a magma with a viscosity of 10^4 Pas, which represents a basalt or basaltic andesite with low crystal content. The volumetric flow rate scaling factor gives values from 0.05 to 26.56 m^3s^{-1} in nature, which is in the range of natural values recorded for volcanic systems (Traversa et al., 2010; Chanceaux and Menand, 2016).

2.5.4.2. Experimental observations

In experiment A (L_1 = 2 wt.%, L_2 = 2 wt.% LRD), the injected paraffin oil formed a perfect sphere or blob (Figs. 2.14b, c) at the needle tip, which then expanded upward through L_1 by increasing its diameter. From Figures 2.8b and 2.10 it is clear that the Young's modulus and yield stress of 2wt. % LRD are low. Therefore, 2 wt. % LRD is capable of undergoing visco-plastic flow after yielding and its behaviour is almost fluid-like. Due to this visco-plastic flow behaviour under low stresses, the elastic strain energy of the growing intrusion is dissipated before a crack can form. Since there was no evidence for brittle failure in this experiment, we interpret the paraffin oil intrusion to have been emplaced by visco-plastic yielding of the LRD and ballooning.

In experiment B, with higher concentration LRD (L_1 = 3 wt. %, L_2 = 3 wt. %) the paraffin oil was emplaced by brittle sill propagation. An initial flat inner sill formed at the L_1/L_2 interface, followed by the formation of an inclined sheet (after 190 s) to define a saucer-shaped intrusion (Figs. 2.14d,e). Finger-like geometries and offset lobate segments (Figs. 2.14d,e; blue lines) formed during sill propagation, resembling features observed at the margins of sill complexes in nature (Thomson and Hutton, 2004; Magee et al., 2016). The horizontal inner sill (at the interface) and the inclined outer saucer segments indicate brittle, tensile fracture propagation mechanisms. Therefore, under the experimental conditions reported here, higher concentrations of LRD behave like solids and form tensile brittle cracks, which are favoured over spherical intrusions to minimise elastic strain energy. This is because the elastic strain energy of a penny-shaped crack is significantly less than that of a sphere (Kato et al., 1996). The formation of finger-like geometries and lobe segments may be related to the development of elasto-viscoplastic instabilities at the propagating sill front (e.g., Eslami and Taghavi, 2017;

Pihler-Puzović et al., 2018). However, further discussion of such instabilities is beyond the scope of the present paper and is the subject of future work in preparation (Chapter 4).

The 3D intrusion experiments presented here show different structural and geometrical behaviours to the experiments reported by Bertelsen et al. (2018), in which oil was injected vertically into Laponite bounded by two vertical, parallel glass plates spaced 5 mm apart (i.e., a Hele-Shaw cell). At high concentrations (3.5 wt. %) and very low curing times (~0 min), the oil intrusions have round shapes, which Bertelsen et al. (2018) attributed to viscous flow of the LRD. In our experiments, lower LRD concentrations (2 wt. %) and longer curing times (3 days result in 3D blob-like intrusions (Figs. 2.14b, c), which we argue were controlled by plastic yielding and flow of the gel. At such low concentrations in our experiments, the intrusion shape is not influenced by the relatively weak interface between the two layers (Kavanagh et al., 2015), suggesting that the gel structure of LRD may not be fully formed, but still behaving like a weak solid with very low Young's Modulus and complex shear modulus values (Fig. 2.8). This is further supported by rotational strength tests of 2 and 2.5 wt. % LRD, which determined very low yield stress and peak strength values, and almost ideally plastic post-yielding behaviour (Fig. 2.10).

For longer curing times (40 – 240 min) and a higher LRD concentration (3 wt. %), oil intrusions in Bertelsen et al.'s (2019) experiments propagated either by viscoelastic fracturing, shear faulting or elastic tensile fracturing, or a combination of all three. At higher concentrations (Experiment B; 3 wt. %) and longer curing times, our experiment displayed a complex intrusion behaviour, forming a sill with finger-like segments at the propagating front, which eventually developed into a saucer-shape intrusion (Figs. 2.14d, e). In this case, the propagation of the intrusion was directly controlled by the interface between the layers. We infer from these observations that the LRD gel responded to the injection of oil by brittle elastic fracturing.

The combination of rheological measurements and preliminary experimental results presented here indicate that LRD is an ideal analogue material for modelling magma intrusions and fracture propagation in shallow crustal rocks. There is also considerable potential for the use of LRD in other analogue modelling applications such as fault development within landslides, studies of localized versus distributed faulting within the upper crust, as well as earthquake and subduction simulations. The mechanical properties of LRD vary significantly with concentration and curing time, displaying elastic, visco-elasto-plastic to plastic rheological behaviours depending on the applied strain and strain rates.

2.6. Conclusions

LRD is well suited as a brittle-elastic rock analogue for modelling upper crustal rocks during magma emplacement and fracture propagation. It has low surface tension, which minimizes surface tension effects in geological experiments and is chemically and biologically stable, which is advantageous for safe laboratory work. LRD is also fully transparent and photo-elastic so it can be used to visualise stress patterns in host-rock analogues (e.g., Bertelsen et al. 2018).

The rheological tests reported here characterise the mechanical behaviour of different concentrations of gel-forming LRD. Our results show that LRD is linear viscoelastic with elasticity dominated mechanical properties at low shear strains (<10 %, shear rate = 0.1 s^{-1}). At higher shear strains (>26.2 %) all LRD concentrations show permanent plastic deformation as shear strain increases. The transitions between these behaviours depend on the applied strain and strain rate, composition and curing time of the sample, and are much less effected by temperature.

LRD with concentrations from 2.5 wt. % to 4 wt. % are suitable analogues to model brittle elastic and plastic deformation of rocks in the Earth's crust. Concentrations above 4 wt. % are not recommended as they form a gel structure too quickly, which prevents proper mixing, resulting in clumps and trapping of air bubbles. To model brittle viscoelastic behaviour in the laboratory, shear strain amplitudes γ must be < 10% (at shear strain rate 0.1 s^{-1}). Plastic deformation occurs at shear strain amplitudes γ > 26.2 % and a more complex behaviour develops in between these strain limits. Hence, LRD has significant potential as a laboratory analogue modelling material because it reproduces the full range of upper crustal rock behaviours from elastic, visco-elasto-plastic to plastic.

Acknowledgements

We gratefully acknowledge financial support from an Australian Research Council Discovery Grant (DP190102422) to A.R.C. A PhD scholarship (DIPRS) from Monash University (Melbourne) to U.S.N.A is greatly appreciated. We greatly thank Dr. Anja Slim (Monash University) for very useful discussions about material rheology.

Chapter 3

Laboratory Modelling of Sill Emplacement: Part 1 – saucer-shaped intrusions

Uchitha N. Arachchige[1], Alexander R. Cruden[1], Roberto Weinberg[1], Anja Slim[1], Jonas Köpping[1]

[1]School of Earth, Atmosphere and Environment, Monash University, 9 Rainforest Walk, Clayton, VIC 3800, Australia

Abstract

Igneous sills with characteristic saucer shapes are observed in sedimentary basins worldwide. Previous sill emplacement models using end-member rheological properties (i.e., brittle elastic or plastic) have produced saucer-shaped sills with simple planar geometries. However, these models either do not fully reproduce the profiles of natural saucer-shaped sills, or they require high horizontal stresses to account for sill geometries in nature. Furthermore, field and 3D seismic observations indicate that saucer-shaped sills have non-planar margins, which are characterised by the presence of lobate or finger-like segments. Here we present the results of a series of scaled laboratory experiments that model magma emplacement into layered rocks, such as those found in sedimentary basins, with a particular focus on the formation of saucer-shaped sills. The experiments employ visco-elastic-plastic Laponite RD® (LRD) gels to model upper crustal rocks, and Newtonian paraffin oil as the magma analogue. Both homogenous and layered analogue upper crust is considered, where layering is simulated by varying the concentration and strength of LRD. Paraffin oil is injected from the side wall of the experimental tank. In homogenous 3 wt. % LRD, the injected oil formed a saucer-shaped intrusion with the shortest inner sill observed among all of the experiments. Saucer-shaped sills always formed in experiments with a two-layer upper crust, in which paraffin oil is injected along or adjacent to the contact between layers. These experiments show sharp transitions from an inner flat sill to outer inclined sheets, which are characterised by non-planar margins. The experimental results show that: (1) the transition from an inner flat sill to outer inclined sheet occurs when the sill radius to overburden depth ratio (r/H) is between 0.5 and 2.5; (2) the inclined sheets propagate upwards with angles, θ = 15° to 25°; (3) the ratio of the Young's modulus (E^*) between the layers controls when the inner flat sill to outer inclined sheet occurs; and (4) irregular finger-like and/or lobe segment geometries form at the propagating tip of the intrusion. The results also suggest that there is no strict requirement for high horizontal stresses to form natural saucer-shaped sill geometries. We conclude that the experimental saucer-shaped intrusions emplaced into layered visco-elastic-plastic crustal analogues better represent natural, complex saucer-shaped sill geometries. Furthermore, the observed sharp transitions between inner and outer sills are compatible with brittle-elastic fracture mechanisms operating at the intrusion scale.

3. 1. Introduction

Igneous sheet intrusions such as dykes and sills are broadly planar structures that are the principal pathways for the migration of magma through the upper crust. Although dykes have traditionally been considered to play the dominant role in magma plumbing systems, recent three dimensional (3D) seismic reflection studies of offshore sedimentary basins suggest that mafic sill complexes play a major, and perhaps leading, role in the vertical and horizontal transport of magma in the shallow crust (Magee et al., 2016, 2019). Such sill complexes often comprise non-planar, interconnected saucer-shaped sills and inclined, strata-discordant intrusions (Thomson and Hutton, 2004; Hansen and Cartwright, 2006).

Saucer-shaped sill morphologies are regarded to be a fundamental feature of mafic intrusions in shallow sedimentary basins (Galland et al., 2009; Galland & Scheibert, 2013; Chen et al., 2017). Field observations (e.g., Golden Valley Sill Complex, South Africa; Chevallier and Woodford, 1999; Planke et al., 2005; Planke, 2008) and two-dimensional (2D) and 3D seismic reflection observations (Hansen et al., 2004; Thomson and Hutton, 2004; Hansen and Cartwright, 2006; Hansen et al., 2008) of saucer-shaped sills indicate that they comprise a sub-horizontal, strata-concordant, inner sill, forming the base, and an inclined, strata-discordant, concave upward outer section (Figs. 3.1a, 3.2a). Field observations and 3D seismic surveys have also found that these intrusions have non-planar, segmented outer margins consisting of lobes and fingers that range in scale from metres to kilometres (Pollard et al., 1975; Thomson and Hutton, 2004; Hansen and Cartwright, 2006; Magee et al., 2016).

The emplacement mechanisms of saucer-shaped sills are mainly attributed to either the elastic or plastic properties of the host rocks, as well as interaction with Earth's free surface. By considering the Mode I and Mode II stress intensity factors at the tip of a horizontal fluid-filled fracture in an elastic medium with a free upper surface, Pollard and Holzhausen (1978) showed that horizontal sills transition into inclined sheets when their depth is less than two-times their radius. This finding is supported by numerical (e.g. Malthe-Sørenssen. et al., 2004; Walker and Gill, 2020) and analogue models (e.g. Bunger et al., 2008) using elastic host rocks, which found that saucer-shaped sills form due to the mechanical interplay between elastic deformation around the growing sill and upward displacement of the overburden towards a free upper surface (Figs. 3.1b, d). However, models of Walker and Gill (2020) and Bunger et al. (2008)

require quite high horizontal stresses to produce geometries that approach those observed in nature (Fig. 3.2c).

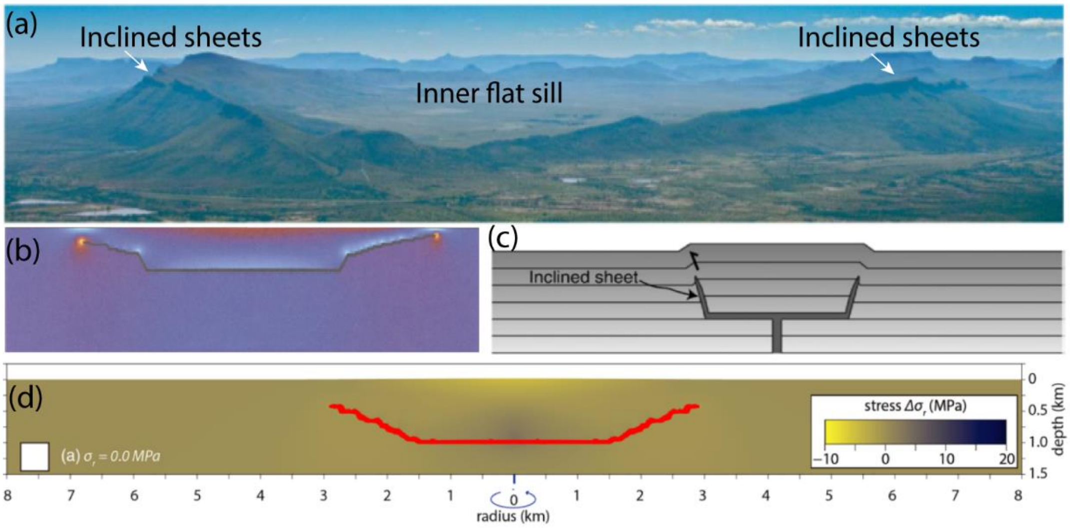

Figure 3.1. *(a) Oblique aerial view of the Golden Valley sill in the Karoo basin, South Africa showing an inner flat sill and outer inclined sheets (from Polteau et al. 2008). (b) Numerical simulation by Malthe-Sørenssen et al. (2004) showing upward deflection due to the elastic interaction with the overburden. (c) Schematic showing the overburden uplift and corresponding shear fault development due to sill inflation, resulting in inclined sheets (from Galland et al. 2009). (d) Numerical simulation by Gill and Walker. (2020) showing the morphology of a saucer-shaped sill in the absence of a horizontal tectonic compressional stress.*

A recent numerical analysis by Haug et al. (2017) using rigid-plasticity theory in a homogenous Mohr-Coulomb material showed that saucer-shaped sills can also be created due to inelastic damage (i.e., shear failure) caused by an inflating flat sill (Fig. 3.2c). Furthermore, analogue experiments using granular Mohr-Coulomb host-rock materials that undergo plastic deformation also formed saucer-shaped sills (Mathieu et al., 2008; Galland et al., 2009) (Fig. 3.1c). However, inner sill to inclined sheet transitions, sill inclinations and overall geometries of saucer-shaped sills of these numerical (Fig. 3.2b) and experimental models (Fig. 3.2c) do not match with those in nature (Fig. 3.2a). Furthermore, experiments using brittle-elastic gelatine, a common host rock analogue, have successfully produced sills and dykes but not saucer-shaped sills (Kavanagh et al., 2006, 2015, 2018a).

All of these saucer-shaped sill emplacement models assume ideally elastic or plastic end member rheological behaviour of host rocks. However, Earth's crust is thought to behave as a complex visco-elastic-plastic material (Ranalli, 2001; Bertelsen et al., 2018a). Therefore, the models summarised above are likely not able to fully simulate the natural diversity of intrusion geometries, including the formation of saucer-shaped sills. Moreover, some models require quite high horizontal stresses to get those in nature (Fig. 3.2) (Bunger et al., 2008; Gill and Walker, 2020; Walker and Gill, 2020).

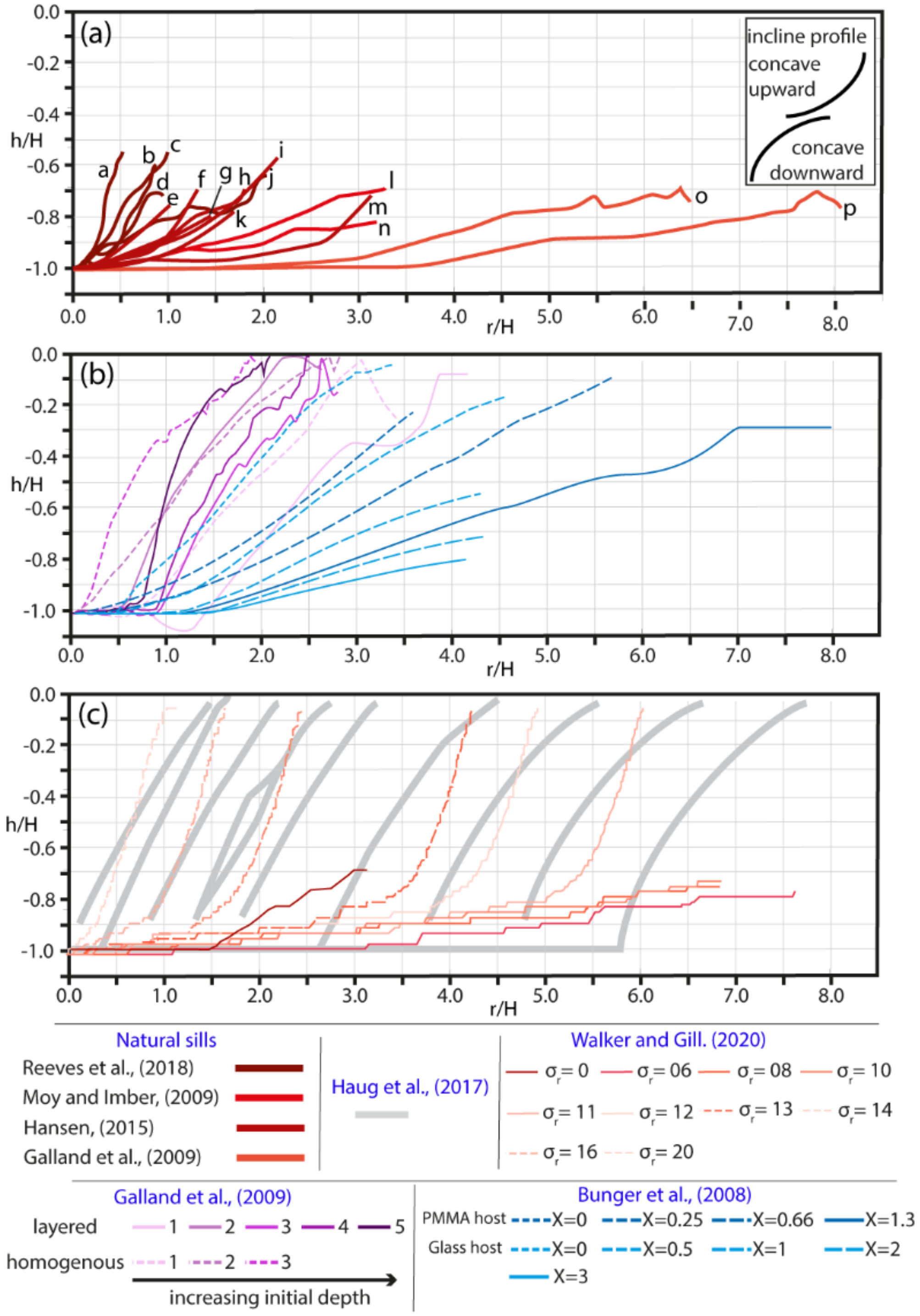

Figure 3.2. *A comparison of saucer-shaped sill geometry in (a) nature, (b) experimental and (c) numerical models (modified after Walker and Gill, 2020). The axes plot sill radius (r) against intrusion depth (h), normalised by the overburden depth (H). Experiments by Galland et al. (2009) (purple curves*

in Fig. 3.2b) used elasto-plastic silica powder as the host-rock analogue, while Bunger et al. (2008) used brittle-elastic glass or polymethyl methacrylate (PMMA) (blue curves in Fig. 3.2b). Numerical models by Walker and Gill (2020) (red curves in Fig. 3.2c) investigated how a horizontal compressive tectonic stress (σ_r) in an elastic host influences saucer-shaped sill geometries. Haug et al. (2017) used a rigid-plasticity approach to simulate sills in a homogenous Mohr-Coulomb material – grey curves in Fig. 3.2c plot damage zones, where magma is expected to intrude the host rocks, formed by inflation of horizontal cracks of variable starting length. Labels of saucer-shaped sills in nature represent; (a) Sill 2, (b) Sill 1, (c) Sill 3 and (d) Sill 4 in Canterbury Basin, offshore SE New Zealand (Reeves et al., 2018); (e) Morskranes Sill, (f) Sundini Sill, (g) Kvívík Sill, (h) Fugloy Sill, (i) Eysturoy Sill, (k) Streymoy Sill and (m) Svínoy-Fugloy Sill in Faroe Islands (Hansen, 2015); (l) Eocene Sill 1 and (n) Eocene Sill 2 in Faroe-Shetland Basin (Moy and Imber, 2009); (o) Golden Valley Sill, South Africa and (p) Tulipan , Møre basin (Galland et al., 2009).

Most saucer-shaped sills in nature form in sedimentary basins that contain mechanically layered strata (Malthe-Sørenssen et al., 2004; Kavanagh et al., 2006; Galland et al., 2009). Sill intrusions modelled by Kavanagh et al., (2006, 2015) show that a layered system with a stiffer upper layer is required to create experimental sills. According to their experimental results, a weaker interface and the rigidity contrast (i.e., Young's modulus ratio) between the layers play major roles in the formation and propagation of sills. This has been further supported by analogue experiments of saucer-shaped intrusions using granular materials (Galland et al., 2009), which found that mechanical layering is required to create the inner sills of saucer-shaped intrusions. However, Galland et al. (2009) did not test the effects of rigidity contrasts on saucer-shaped intrusion formation and propagation. Therefore, the effect of layering and its mechanical properties such as the Young's modulus ratio on the emplacement of saucer-shaped intrusions remain poorly understood.

Although field and 3D seismic reflection data have yielded a wealth of information about the geometries of saucer-shaped sills, field observations are limited due to the lack of well-preserved outcrops. Furthermore, 3D reflection seismic observations are limited by their spatial resolution, making it challenging to characterize intrusion geometries and associated structures related to their propagation. The geometries and emplacement mechanisms of saucer-shaped sills are therefore still poorly constrained and many fundamental questions remain to be answered. Such as, is it possible to reproduce the geometry of natural saucer-shaped sills in the laboratory using host rock analogues with complex visco-elastic-plastic rheology? What emplacement mechanisms control the development of saucer-shaped sills within complex host rock analogues? How do rigidity contrasts between stratigraphic layers influence the propagation of intrusions? Are high horizontal stresses strictly required to form natural saucer-shaped geometries? Understanding of these questions will provide fundamental knowledge and insights on the formation and propagation of magmatic intrusions in volcanic plumbing systems.

Answering these questions requires experiments that simulate injection of a viscous liquid into a visco-elastic-plastic host material, and the ability to analyse the geometry of the resulting intrusions and associated host rock deformation. In this paper, we document the results of laboratory experiments in which paraffin oil (the magma analogue) is injected into visco-elastic-plastic Laponite RD® gels, simulating the upper crust. Our objectives are to simulate the emplacement of saucer-shaped sills and to better constrain the mechanisms governing their fundamental geometry, including the effects of mechanical layering. The complex segmentation patterns that are observed at the margins of our model sills are the subject of a companion paper (Chapter 4) and only briefly presented here.

3. 2. Experimental methods

3. 2. 1. Experimental setup

Our experiments are designed to simulate the horizontal propagation of sills in the laboratory and to visualise the resulting lateral flow of analogue magma. The main objective of the experiments reported here is to investigate the emplacement and propagation of saucer-shaped intrusions in layered analogue host rocks. The experimental setup comprises a plexiglass tank (30 cm x 30 cm x 6 cm) filled with layers of Laponite RD® (LRD) gel as the upper crustal analogue (Layer 1 and Layer 2, Fig. 3.3). The upper surface of LRD in the tank is a free surface, while the vertical side walls and base of the tank are no-slip boundaries.

Paraffin oil (magma analogue) is injected horizontally into the LRD using a tapered needle (2 mm diameter) via a nozzle at the side of the tank fed by a peristaltic pump at a controlled volumetric flow rate. The experiments involve varying the volumetric flow rate of the intruding fluid, and the rigidity of the LRD layers. Fluid propagation is monitored by high resolution

DSLR cameras (Fig. 3.3) placed above and at the side of the tank to capture the intrusion geometry and its evolution in plan and cross-sectional view, respectively.

3. 2. 2. Image processing

We use blue-channel pixel intensity values to map contour lines of the intrusion margin over time. Pixel intensity values at each time step (I) are normalised by pixel intensity values at time step 0 (before the intrusion starts) (I_0), resulting in $I/I_0 = 1$ for the LRD host and $I/I_0 < 1$ for the intruding fluid. The I/I_0 ratio is used to define a threshold for the intruding fluid, which is used to determine growth contour lines using a built-in ‘contour’ function in MatLab. Since growth contours have irregular shapes, we calculate best-fit circles to the contour line at each time step and use the resulting radius to quantify horizontal sill growth rates. However, the intrusion radius measurements are not corrected for the slope of the outer sill. Since the images are captured in map view, growth contours for inclined outer sheet intrusions therefore appear closer.

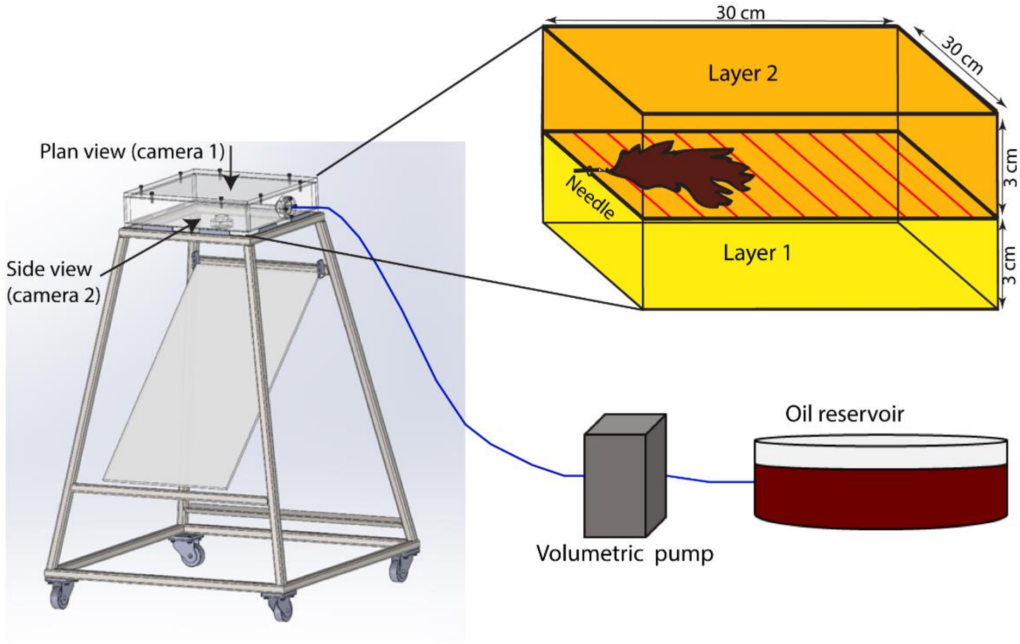

Figure 3.3. *Schematic diagram of the experimental setup used in this study. A volumetric peristaltic pump injects paraffin oil horizontally via a needle into either homogenous or two-layer Laponite RD® gel. Two DSLR cameras capture the geometric details of sill propagation from top and side views.*

3.2.2. Analogue materials

3.2.2.1. Crustal host rock analogue

The host rock analogue used in the experiments is Laponite RD® (LRD), a gel-forming grade of synthetic smectite clay manufactured by BYK Additives and Instruments (2014). Depending on its concentration, curing time and pH, LRD displays a wide range of viscoelastic properties, with purely elastic and viscous domains (Bonn et al., 2002; Ruzicka and Zaccarelli, 2011; Kaushal and Joshi, 2014; Arachchige et al., 2021). When mixed with water, LRD forms a transparent gel, which is similar to gelatine but is colourless and more transparent. Like gelatine, its photo-elastic properties can be used to visualize and map stresses associated with propagating fractures. LRD is a chemically and biologically stable material and it is easy to alter its mechanical properties, such as the Young's modulus, by changing its concentration. LRD has lower surface energy values (24 - 44 mJ/m^2; Norris et al., 1993) compared to gelatine, a frequently used intrusion host rock analogue (1 J/m^2; Kavanagh et al., 2013). This ensures that surface tension dynamics are minimized in geological analogue experiments using LRD. Rheological measurements of LRD reported by Arachchige et al. (2021) indicate that it is suitable for modelling the visco-elastic-plastic deformation of rocks, including elastic and plastic end members. Linear visco-elastic (LVE) behaviour occurs for shear strains, $\gamma < 10\%$ and strain rate of up to 0.01 s^{-1} for concentrations from 2 wt. % to 4 wt. % and a curing time of 72 hours. LRD starts to yield at shear strain, $\gamma = 10$ % for concentrations 2 wt. % to 4 wt. % with yield strength of 25 to 200 Pa, respectively. Higher shear strains ($\gamma > 26.2$ %) and strain rate $\dot{\gamma} \geq 0.01$ s^{-1} must be maintained to model plastic deformation. The Young's modulus of 2 wt. % to 4 wt. % LRD, with a curing time of 72 hours vary from 1.05×10^3 to 1.18×10^4 Pa, respectively. Here we use Young's modulus values of LRD as the main host rock variable and following Arachchige et al. (2021) assume that LRD is incompressible with Poisson's ratio = 0.5.

3.2.2.2. Magma analogue material

We use paraffin oil at 22.5 °C as the magma analogue due to its non-reactive stability with LRD. Paraffin oil has a viscosity of 0.16 Pa s and the density of 850 kg m^{-3} at this temperature. The magma analogue was mixed with red dye without altering its viscosity to provide a better visual contrast with the host material.

3.2.3. Scaling

Our experiments are approximately scaled to nature (Table 3.1) using methods developed by Hubbert (1937), Ramberg (1982), Merle and Borgia (1996), Mathieu et al. (2008), Galland et al. (2009) and Arachchige et al. (2021). The principle is to define scaling factors and dimensionless numbers for the model, which ensure approximate geometric, kinematic and dynamic similarity to processes in nature.

Table 3.1. *Symbols, units and values of variables in nature and model for scaling factors and dimensionless ratios. See equation 3.4 and 3.5 for Π_4 and Π_5.*

Parameter	Units	Definition	Value		
			Nature (p)	Model (m)	Ratio*(m/p)
ρ_c	kg m^{-3}	Density of host rock	2800	1000	0.357
ρ_m	kg m^{-3}	Density of magma	2700	850	0.3
g	m s^{-2}	Gravity acceleration	9.81	9.81	1
V_i	m s^{-1}	Velocity of intrusion	0.2	10^{-5}	$5 \cdot 10^{-5}$
L	m	Length	100	0.01	10^{-4}
t	s	Time	-	900-2700	$2 \cdot 10^{-2}$
μ	Pa s	Viscosity of intrusion	2.2×10^5	0.16	7.14×10^{-7}
Q_i	m^3 s^{-1}	Volumetric flow rate of intrusion	(0.02 - 13.28)	8.3×10^{-9}	(6.25×10^{-10} - 3.75×10^{-7})

	Definition of dimensionless ratios	Nature	Model
Π_1	Intrusion thickness (T)/length (L)	~ 10^{-2}	~ 10^{-2}
Π_2	Intrusion thickness (T)/depth (H)	0.06 – 0.66	0.03 – 0.10
Π_3	Intrusion height (h)/length (L)	0.2 – 0.3	0.3
Π_4	Inertial/viscous forces	2.5×10^{-6} – 270	(5.6 – 12.4) x 10^{-4}
Π_5	Magma/country rock densities	–0.08 – 0	0.14

Stress scaling factor	**$\sigma^* = \rho^* g^* L^* = 3.57 \times 10^{-5}$** Model is 10^5 times weaker than in nature
Time scaling factor	**$t^* = L^*/V^* = 2 \times 10^{-2}$** 1 min in model ~ 0.83 hr in nature
Viscosity scaling factor	**$\mu^* = t^* \sigma^* = 7.14 \times 10^{-7}$** Model intrusion represents a magma viscosity of 10^4 Pas
Volumetric flow rate scaling factor	**$Q^* = \Delta\rho^* L^{*3} E^{*-1} V^* = 6.25 \times 10^{-10} - 3.75 \times 10^{-7}$ m^3s^{-1}** Model volumetric flow rates = 0.02 – 13.28 m^3s^{-1} in nature

We define the length scale factor (L*) as the ratio between the overburden depth of the sill in the model (subscript m) to one in the shallow crust (subscript p), which is initially taken as 10^{-4} (1 cm represents 100 m). The ratio between the density of LRD in our experiments and that of the natural host rocks (ρ*) is ~ 0.36 and the gravitational acceleration is the same in our experiments and in nature (g* = 1). Thus, the stress scaling factor is:

$$\sigma^* = \rho^* g^* L^* = 3.6 \times 10^{-5} \tag{3.1}$$

Comparing the average model intrusion tip velocity of ~ 1 x 10^{-3} ms^{-1} to an estimated natural magmatic intrusion velocity of 0.2 ms^{-1} (range between 0.1 ms^{-1} and 0.5 ms^{-1}; Spence and Turcotte, 1985; Kavanagh et al., 2013) gives a velocity scaling factor, $V^* = 5 \times 10^{-3}$. We can now define the time scaling factor as

$$t^* = L^*/V^* = 2 \times 10^{-2} \tag{3.2}$$

Therefore, 1 min in our experiments represents 0.83 hr in nature. Using σ^* and t^*, the viscosity scaling factor becomes

$$\eta^* = \sigma^* \, t^* = 7.2 \times 10^{-7} \tag{3.3}$$

So paraffin oil (magma analogue) with a viscosity of 0.16 Pas (Arachchige et al., 2021) is equivalent to a magma in nature with a viscosity of 10^4 Pas, consistent with basaltic andesite with low crystal content (Persikov, 1991; Mathieu et al., 2008).

The measured Young's modulus, E, of LRD concentrations after 7 days curing time used in the experiments is 10^3 - 10^4 Pa (see Chapter 2) . Since E of upper crustal sedimentary rocks is typically in the range of 10^9 - 10^{10} Pa (Kavanagh et al., 2013), the Young's modulus scaling factor, E* in our experiments is $10^{-7} – 10^{-5}$. Therefore, based on σ^* and E* our model host rock is ~10^5 times weaker than in nature.

With the exception of one experiment (10A), the volumetric flow rate of intruding magma in our experiments is kept constant, and only the Young's modulus of the host rock layers is varied between experiments. The only input geometric variable is the Layer 2 overburden depth, H (Fig. 3.2). Output geometric variables are the intrusion length, L, thickness, T, and the vertical height of the intrusion, h, relative to the interface between the horizontal layers or the injection needle.

Following the Buckingham-Π theorem (Barenblatt, 2003; Galland et al., 2009), we define five independent dimensionless numbers that characterise the system (Table 3.1), which are used to assess the geometrical, kinematic and dynamic similarities between the experiments and nature. The first three dimensionless numbers are the geometric ratios of the system:

$$\Pi_1 = T/L,$$
$$\Pi_2 = T/H, \tag{3.4}$$
$$\Pi_3 = h/L.$$

The length, L, and the thickness, T, of shallow crustal sills in nature are typically in the range of 10 – 100's km and 20 – 200 m respectively (Galland et al., 2009; Cruden et al, 2017). Therefore, Π_1 in nature is in the order of 10^{-2}. Experimental sill lengths and thicknesses vary between 5 – 9 cm and 1 – 3 mm, respectively, so Π_1 is also on the order of 10^{-2}. Overburden depth, D, is 3 cm in the experiments and 100 – 3000 m in nature. Thus, Π_2 ranges between 0.03 – 0.1 and 0.006 – 2 in the experiments and nature, respectively. Calculated Π_3 values range from 0.22 to 0.56 for the experiments, and are estimated to be around 0.3 in nature (Mathieu et al., 2008). The geometric dimensionless numbers of the models are therefore close to the natural values, indicating approximate geometric similarity.

The Reynolds number, which is the ratio of inertial to viscous forces in a flow, establishes if the flow regime within the intrusion is laminar or turbulent:

$$\Pi_4 = Re = \frac{\rho_m T V}{\eta} \tag{3.5}$$

where ρ_m is the density and η is the viscosity of magma. In the experiments, Π_4 varies between 8×10^{-3} to 1.6×10^{-2}. Therefore, viscous forces are dominant, inertial forces are negligible and the flow is laminar (i.e., Re << 2300; Eslami and Taghavi, 2017). Reynolds numbers for magma flow within dykes and sills in nature varies from 2.5×10^{-6} to 270 for felsic and mafic magma respectively (Galland et al., 2009). Therefore, the Reynolds numbers in our experiments are consistent with those in nature, where magma flow is usually laminar.

The final dimensionless number is the ratio of the magma and the host rock density, corresponding to the buoyancy of the magma, which can be expressed by:

$$\Pi_5 = 1 - \frac{\rho_m}{\rho_c} \tag{3.6}$$

Where ρ_c the density of the upper crustal host rocks. In our experiments, $\Pi_5 = 0.15$ and in nature it varies between -0.8 to 0 in the shallow crust (Galland et al., 2009), indicating that magma is neutrally to negatively buoyant. In the experiments the analogue magma is slightly positively buoyant. However, as most sills form and propagate as horizontal to sub-horizontal cracks, buoyancy effects are negligible (Lister and Kerr, 1991; Kavanagh et al., 2006; Galland et al., 2009) in both nature and experiments.

3.3. Experimental results

Here we present the outcomes of experiments with two different initial setups. In the first setup, the upper crust is represented by a single homogeneous layer. In the second setup, the crust comprises two layers with different LRD concentrations and therefore different Young's moduli (Table 2.2). In both setups the viscosity of the intruding fluid and the intrusion depth were kept constant, as was the volumetric injection rate, with the exception of Exp. 10A.

Table 2.2. *Summary of experiments and parameters.*

No	X_{LL}	ρ_{LL}	E_{LL}	X_{UL}	ρ_{UL}	E_{UL}	E_{L2}/E_{L1}	θ	comments
7	3	1050	5013	-	-	-	-	71	Planar crack
3	2.5	1045	2405	4	1075	10266	4.27	-	Vertical crack in bottom layer
5	3	1050	5013	4	1075	10266	2.05	18.5	Flat sill to inclined saucer
6	3	1050	5013	3	1050	5013	1	17.8	Flat sill to inclined saucer
9	3.5	1060	8317	4	1075	10266	1.23	21.7	Flat sill to inclined saucer
10	4	1075	10266	4	1075	10266	1	16.3	Flat sill to inclined saucer
19	3.5	1060	8317	4	1075	10266	1.23	24.5	Flat sill to inclined saucer
23	2	1040	1216	4	1075	10266	8.44	-	Vertical crack in bottom layer
30	3.5	1075	8317	3.5	1060	8317	1	17.1	Flat sill to inclined saucer
10A§	4	1075	10266	4	1075	10266	1	19.5	Flat sill to inclined saucer

X = concentration of Laponite RD® (LRD) in deionised water (wt. %); ρ is density of LRD (kg m^{-3}); E = Young's modulus of LRD (Pa); θ = inclination.

Subscripts L1 = lower layer and L2 = Upper Layer.

§The injection volumetric flow rate in all experiments, Q = 1 ml/min, except experiment 10A where Q = 5 ml/min

3.3.1. Single layer experiments

When paraffin oil was injected into homogenous LRD with concentration of 3 wt. % (Exp. 7, Table 2.2), the intrusion formed a horizontal crack (i.e., a sill) that propagated away from the injection point and then at ~360 s deviated upwards toward the free surface as a steeply inclined sheet (Fig. 3.4a). The propagating front of the intrusion developed irregular finger-like protrusions at the onset of steep upward propagation. At this stage, a narrow high-flow channel also started to form from the injection point, which migrated through the flat sill into the inclined sheet (Fig. 3.4a).

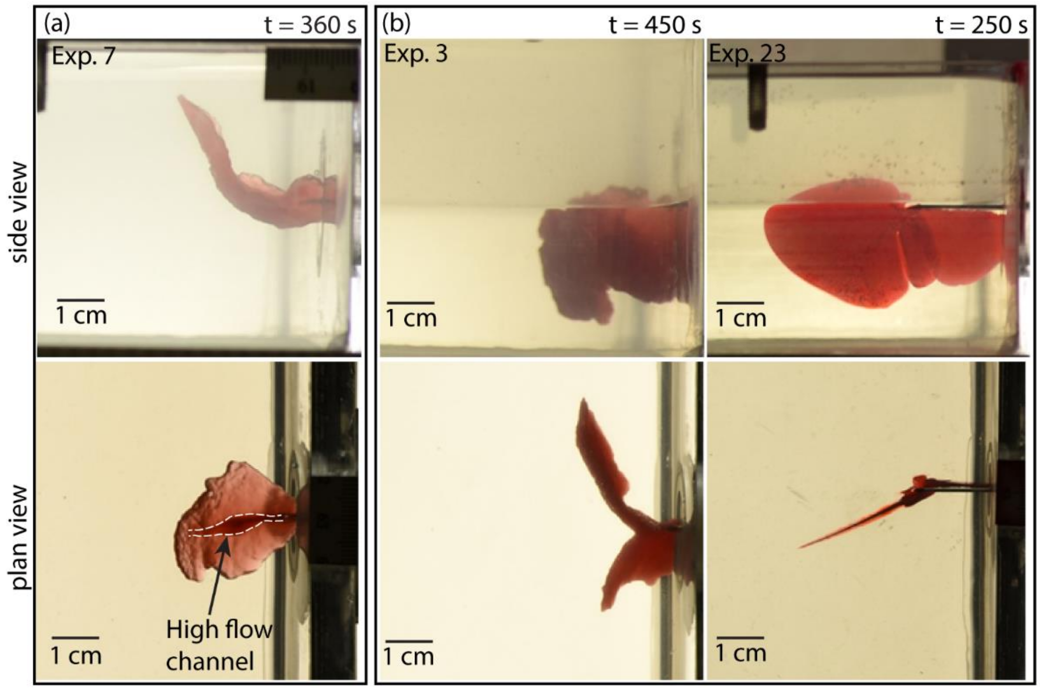

Figure 3.4. *(a) Intrusion propagation styles in a homogenous Laponite RD® gels with concentrations 3 wt. % (Exp. 7). (b) Plan and side views of layered experiments with high rigidity ratio (E_r > 4); Exp. 3 (left panel) and Exp. 23 (right panel). Vertical cracks (dykes) formed within the lower concentration (Layer 1). See Table 3.2 for details.*

3.3.2. Two-layer experiments

In two-layer experiments, the magnitudes of the Young's moduli of the LRD layers (L1 and L2), and the rigidity ratio, $E_r = E_{L2}/E_{L1}$ were varied systematically, while the viscosity of the intruding fluid and the volumetric flow rate were kept constant, with the exception of Exp. 10A

(Table 3.2). The non-dimensional Young's modulus ratio, E_r, was found to be useful for explaining the first-order morphology of the model intrusions. However, second order features of the intrusions, such as marginal lobes and fingers are controlled by additional parameters, which are discussed in more detail in Arachchige et al. (Chapter 4). In most two-layer experiments, an initial planar, sub-horizontal crack formed along the L1/L2 interface and, at a certain point, turned upwards to form an inclined sheet, making a saucer-shaped sill that eventually erupted at the upper free-surface.

3.3.2.1. Case 1: Two-layer experiments with high rigidity ratio ($E_r > 4$)

In two-layer experiments with $E_r > 4$ (Fig. 3.4b), the injected paraffin oil formed vertical cracks that propagated outwards and downwards from the injection point. These dyke-like intrusions were limited to the much weaker, lower layer, which had LRD concentrations X_L = 2. 5 and 2 wt. % in Exp. 3 and 23, respectively (Fig. 3.4b: Table 3.2). The propagating fronts of these intrusions were smooth, without segmentation or finger-like protrusions.

3.3.2.2. Case 2: Two-layer experiments with low rigidity ratio ($E_r < 4$)

In all two-layer experiments with $E_r < 4$, model intrusions initially propagated along the L1/L2 interface as inner flat, penny-shaped sills (Fig. 3.5a). These sills subsequently bent upwards together with dome shaped overburden uplift as they intruded the upper layer, forming inclined sheets (Fig. 3.5b). The inclination, θ_i of these inclined sheets relative to the L1/L2 interface was 15° - 25°, becoming steeper as they approached the free surface (Fig. 3.5c). The propagating fronts of both the inner flat sill and the outer inclined sheets consisted of lobes and finger-like segments that appeared at early stages of growth. When primary individual lobes reach a critical width, they bifurcate into secondary smaller lobes and finger-like segments (Fig. 3.5d). During the propagation of the inner flat sill these lobes and fingers were confined to the 2D plane of the L1/L2 interface. However, once the inclined sheets entered the upper layer, these segments developed 3D morphologies, forming vertically offset, en-echelon structures.

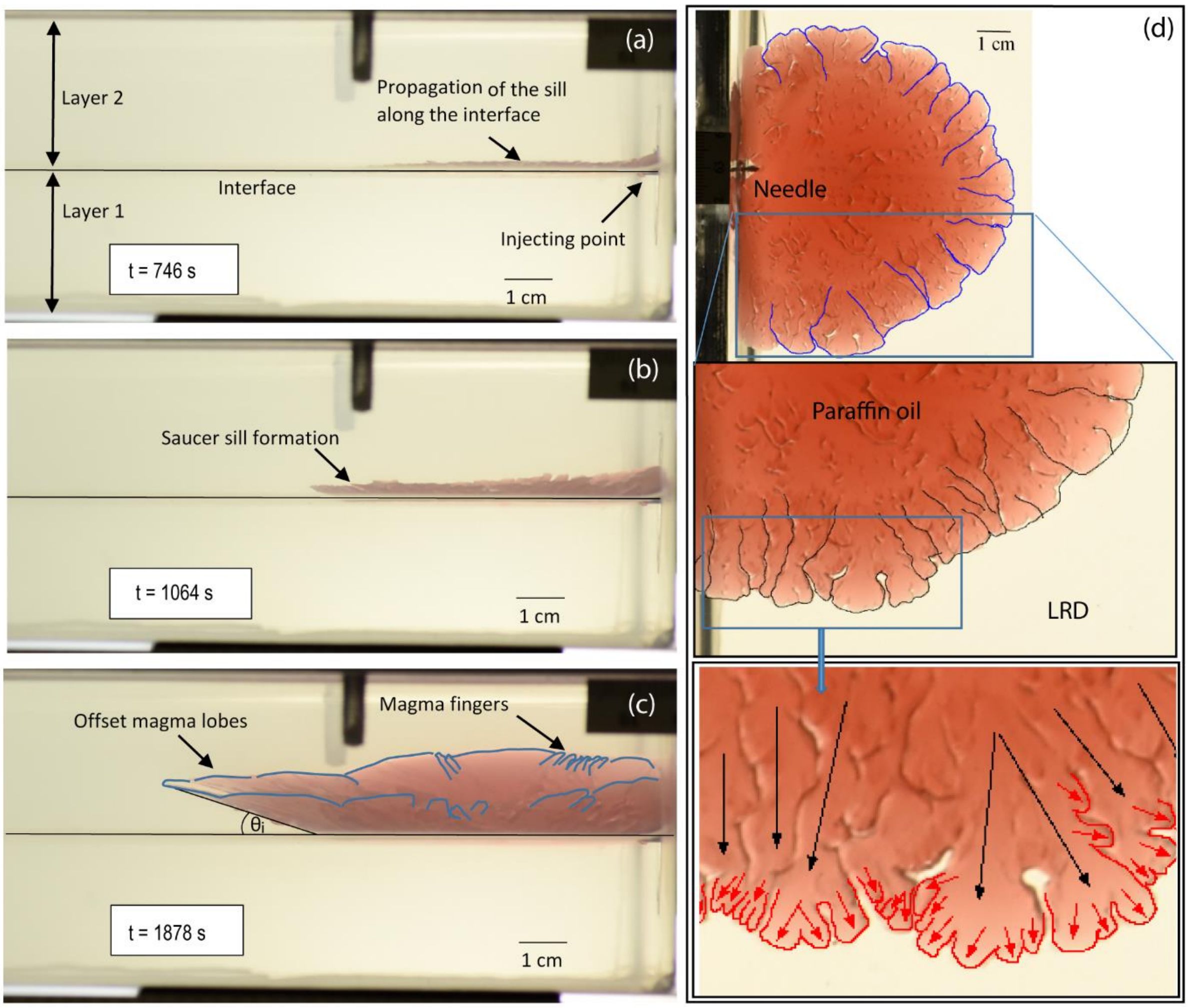

Figure 3.5. *Side views (left panels) and top views (right panels) of sill propagation in a two-layer experiment (Exp. 6) as a function of time (T). (a) Propagation of the inner sill along the two layer interface. (b) Onset of outer, inclined sill formation. (c) Offset lobes and fingers forming at the propagating sill margin. θ_i is the dip of the inclined sheet. (d) Formation and propagation of lobes and magma fingers and associate magma pathways. Paraffin oil (red) is injected from the left through a needle into transparent Laponite RD®. The sill expands radially and breaks into lobes and fingers. Lobe segments show distinct primary (blue) and secondary margins (black) and final magma transport directions (black and red arrows).*

Figure 3.6 plots the vertical profiles of all saucer-shaped sills formed in the one- and two-layer experiments, in which the intrusion height (h) and the radius (r) are normalised by overburden depth (H). The transition radius from the inner sill to the outer inclined sheet occurs over a range of r/H values and the inclined sheets have variable inclinations, θ_i. The single layer experiment (Exp. 7) has the smallest transition radius (r/H < 0.5) and the steepest outer sheet inclination (71°). In two-layer experiments with $1 < E_r < 4$ (Exp. 5, 9 and 19), the transition radius occurs at r/H = 0.5 – 1.25, with much shallower outer sheet inclination angles (15°-25°). However, these inclination angles vary by 2° – 3° in Experiments 5, 9 and 19, indicating a small degree of uncertainty. Experiments 9 and 19 differ from experiment 5 in that E_{LL} is ~81% of E_{UL}, whereas in Experiment 5 this is ~49%. Therefore, sill inclinations are substantially different between experiments, reflecting the relative difference in stiffness between layers. In experiments with E* = 1 (Exp. 6, 10, 10A, 30), the inner flat sills are considerably wider and the transition to the outer inclined sheet occurs at r/H = 1 - 1.5 with similar θ_i angles to the $1 < E_r < 4$ experiments. However, as the relative stiffness increases between Experiment 6 to 30, the inner sill appears to increase in length and the inclination angles are similar. By comparison, the only difference between Experiments 6 and 7 is the interface between the layers in Experiment 6, but it has a much longer inner flat sill with same inclination angle (Fig. 3.6).

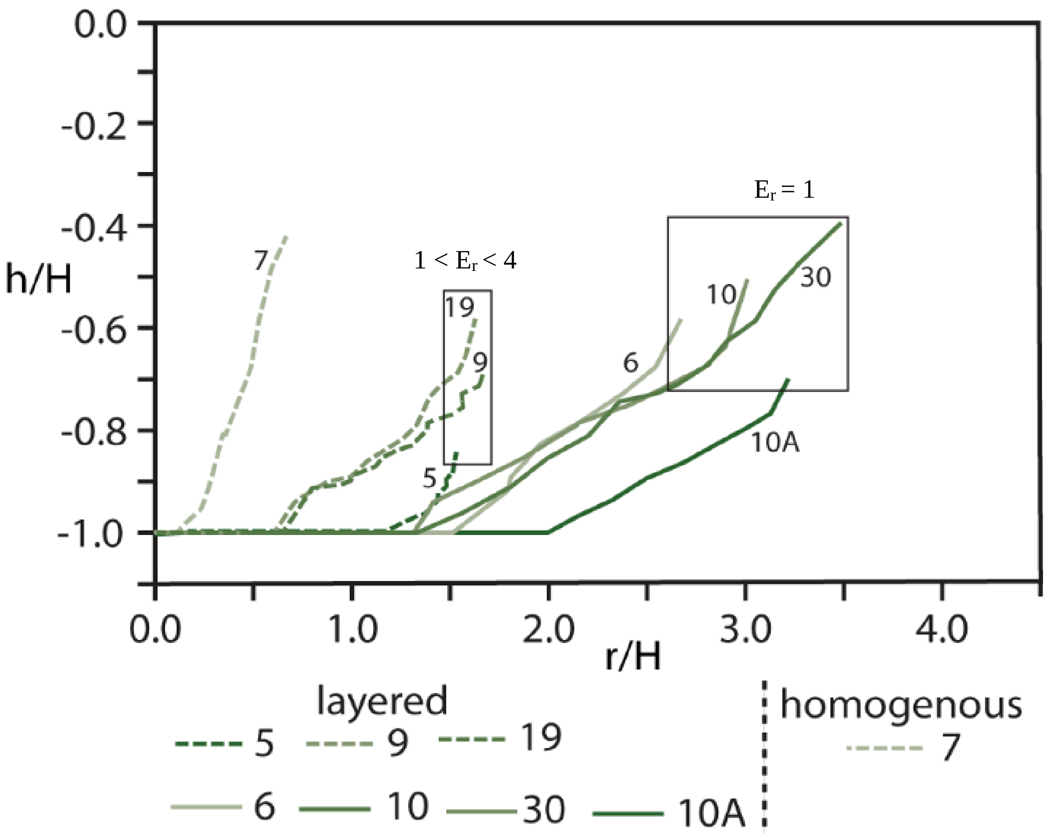

__Figure 3.6.__ Normalised vertical profiles of sills observed in homogeneous and two-layer experiments. Shortest inner sill and the steepest outer sill are form by the homogenous layer experiment (Exp. 7). In layered experiments, the outer sill profiles are concave upward, becoming steeper toward the upper surface.

3.3.3. Growth and propagation of the inner and outer sills

Growth contour maps of the propagating fronts of saucer-shaped sills with rigidity ratios E_r < 4 are shown in Figure 3.7. Because the maps are in plan view, growth contours within the inclined sheets appear more closely spaced than the inner flat section of the sill. Propagation styles for experiments with E_r = 1 (Exp. 6, 30, 10) vary systematically as the absolute value of E and concentration of LRD increases within Layer 2. For E_r = 1 and an LRD concentration of 3 wt. % in L1 and L2 (Exp 6; Fig. 3.5d and 3.7a, Table 3.2), the intrusion propagated with a highly segmented margin characterised by finger-like and lobe structures. The absence of contours at early time steps is due to the unavailability of images due to a momentary camera failure. In Exp. 30 (Fig. 3.7b), with L_1 and L_2 concentration = 3.5 wt. %, growth contours indicate a propagation front with moderately developed segments. When the L_1 and L_2 LRD concentration = 4 wt. % in Exp. 10, the growth contours are smooth, indicating a planar propagation front with very weak to no segmentation (Fig. 3.7c). Two-layered experiments with E_r > 1 also have moderately segmented propagating fronts (Figs. 3.7d-f, similar to those in Exp. 30 (Fig. 3.7b).

The intrusion radius measured in plan view from best fit circles to the growth contours at each time step are plotted against time in Figure 8 for all two-layer experiments with E_r < 4. The inner-outer sill transition radius is marked for each experiment. The horizontal growth rates (i.e. slopes) of the intrusions with Q_i = 1 ml/min vary between 0.45 and 0.55 mm/s.

3.3.4. Influence of volumetric flow rate, Q_i

In order to determine the effect of a higher volumetric injection flow rate, we repeated Exp. 10 (Fig. 3.7c) in Exp. 10A with Q_i = 5 ml/min rather than 1 ml/min. This resulted in the largest inner-outer sill transition radius r/H ~ 2 observed in the two-layer experiments and a similar θ_i angle (Fig. 3.6). As expected, the horizontal growth rate of Exp. 10A is higher than the experiments with Q_i = 1 ml/min, with a value of 0.61 mm/s compared to ~0.5 mm/s (Fig. 3.8).

In contrast to the planar sill margin developed in Exp. 10, growth contours for Exp. 10A (Fig. 3.7f) indicate a complex and strongly segmented propagation front, similar to Exp. 6 (Fig. 3.7a). This implies that the nature of the propagating front is controlled not only by the absolute value of E in Layers 1 and 2 (cf. Figs. 3.7a-c and f), but also on the volumetric injection flow rate of the analogue magma.

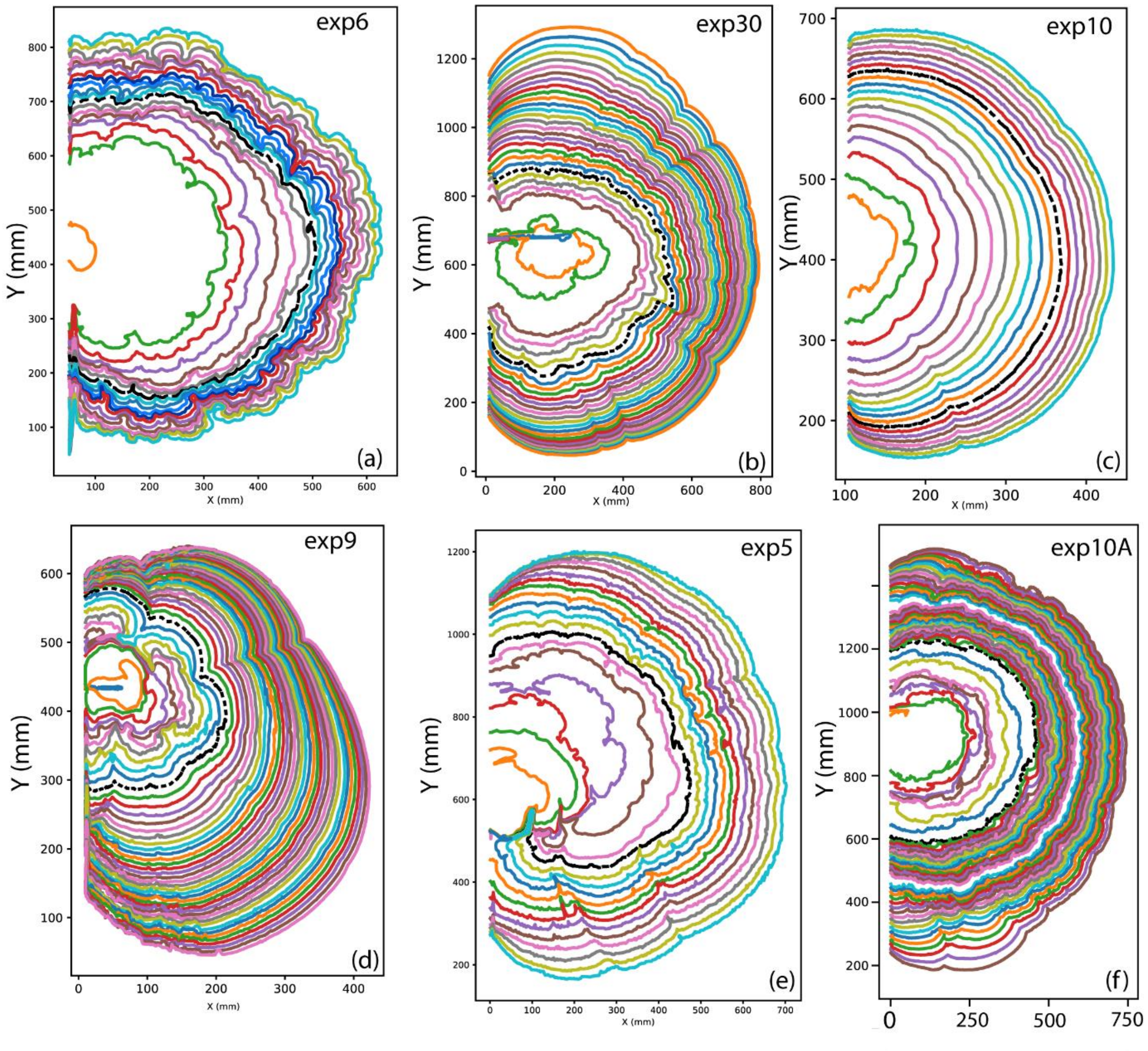

Figure 3.7. *Contour maps of sill margins over time calculated with image analysis. The contour interval is 25 s for all panels except exp.10A (10 s) and the dotted black lines on each map represent the contour at the inner to outer sill transition. The empty space in (a) (Exp. 6) is due to missing images due to camera failure at the early stages of the experiment.*

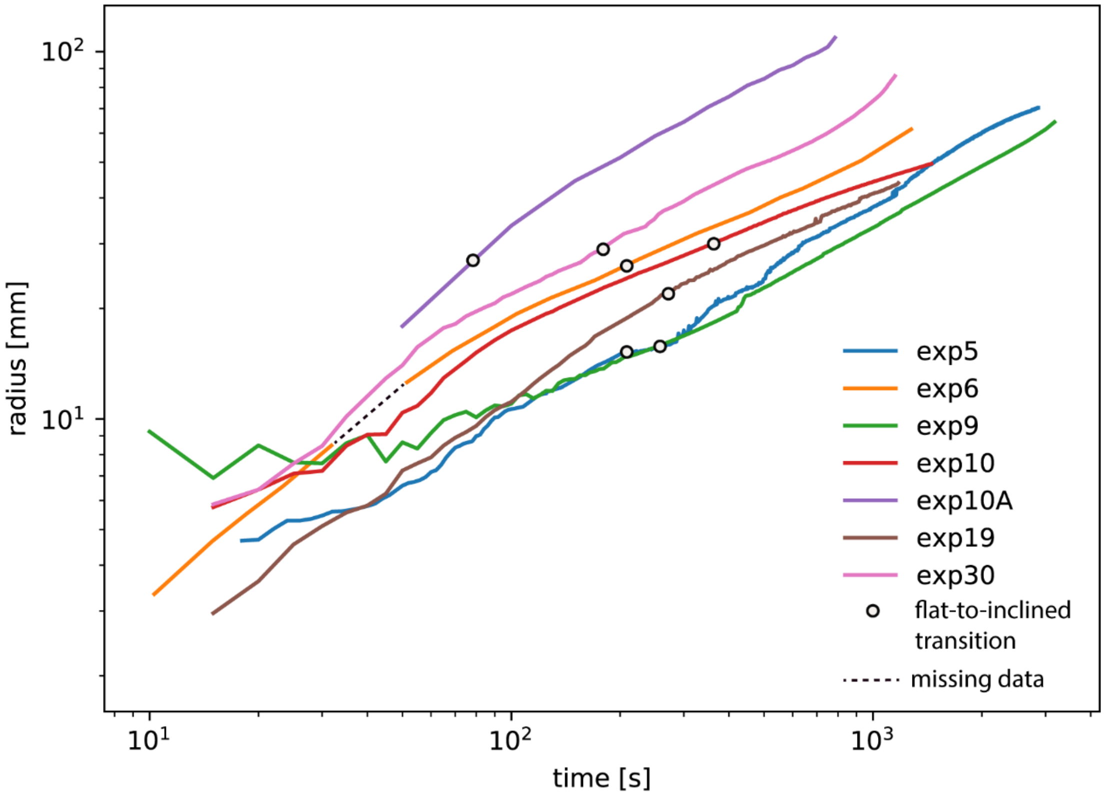

Figure 3.8. *Horizontal growth rates for sills in experiments (in map view) with rigidity ratio* E_r *< 4 plotted as the best fit radius against time. The black open circles on each curve represent the transition from inner flat sill to inclined sheet of saucer-shaped intrusions. See Table 2 for the details of the experiments.*

3.4. Discussion

3.4.1. General considerations

The first-order geometries of intrusions formed in our experiments match the major features of mafic sills observed in nature, particularly those in sedimentary basins. Our homogenous and two-layer experiments (except the vertical dyke in Fig. 3.4b) reproduced the three-dimensional shape of saucer-shaped sills with a horizontal inner sill, emplaced along a horizontal interface in two-layer experiments, followed by a sharp transition to an outer, inclined sheet. Furthermore, the margins of both inner sills and outer inclined sheets in the experiments developed non-planar intrusion fronts with lobes and finger-like structures that are similar to marginal features of saucer-shaped sills observed in 3D seismic reflection seismic data (Thomson and Hutton, 2004; Hansen and Cartwright, 2006) and the marginal lobes developed on propagating sills during solidification experiments (Chanceaux and Menand, 2016). Our 3D experimental results also support the results of 2D numerical simulations of saucer-shaped intrusions (Malthe-Sørenssen. et al., 2004; Walker and Gill, 2020). We therefore suggest that our model results provide insights into mechanical processes governing the emplacement of mafic sills in sedimentary basins.

3.4.2. Emplacement of the inner sill

In homogenous layer experiments, paraffin oil that was injected into low and moderate concentrations of LRD formed either a spherical blob (Arachchige et al., 2021) or a very short inner sill followed by a very steep outer sheet (Fig. 3.4a), respectively. In contrast, in two-layer experiments with low rigidity ratios ($E_r < 4$), paraffin oil injection always resulted in the formation of flat inner sills with large diameters (Fig. 3.4), whereas in experiments with high rigidity ratios ($E_r \geq 4$), a sub-vertical intrusion only propagated in the weaker lower layer (L1; Exp. 3 and 23, Fig. 3.4b). These results suggest that the formation of larger diameter, flat-lying sills requires the presence of layering in host rocks with low rigidity ratios ($E_r < 4$). This conclusion is supported by previous experiments with a layered setup (Kavanagh et al., 2006, 2015; Galland et al., 2009) and numerical calculations (Barnett and Gudmundsson, 2014). In detail, the propagating margin of the inner sill in both homogenous and layered experiments is typically non-planar and often consists of finger-like and lobate segments (Fig. 3.5d). Such complex segmentation was not observed in previous laboratory experimental models of sills using gelatine or granular host media (Mathieu et al., 2008; Galland et al., 2009; Kavanagh et al., 2015). However they are often described from mafic sills in sedimentary basins (Magee et al., 2016; Spacapan et al., 2017) and 3D seismic reflection data (Hansen and Cartwright, 2006; Hutton, 2009). A detailed discussion of these irregular short-wavelength (in relation to the total intrusion length scale) features and their formation is beyond the scope of the present paper and they are analysed in detail in Arachchige et al. (Chapter 4).

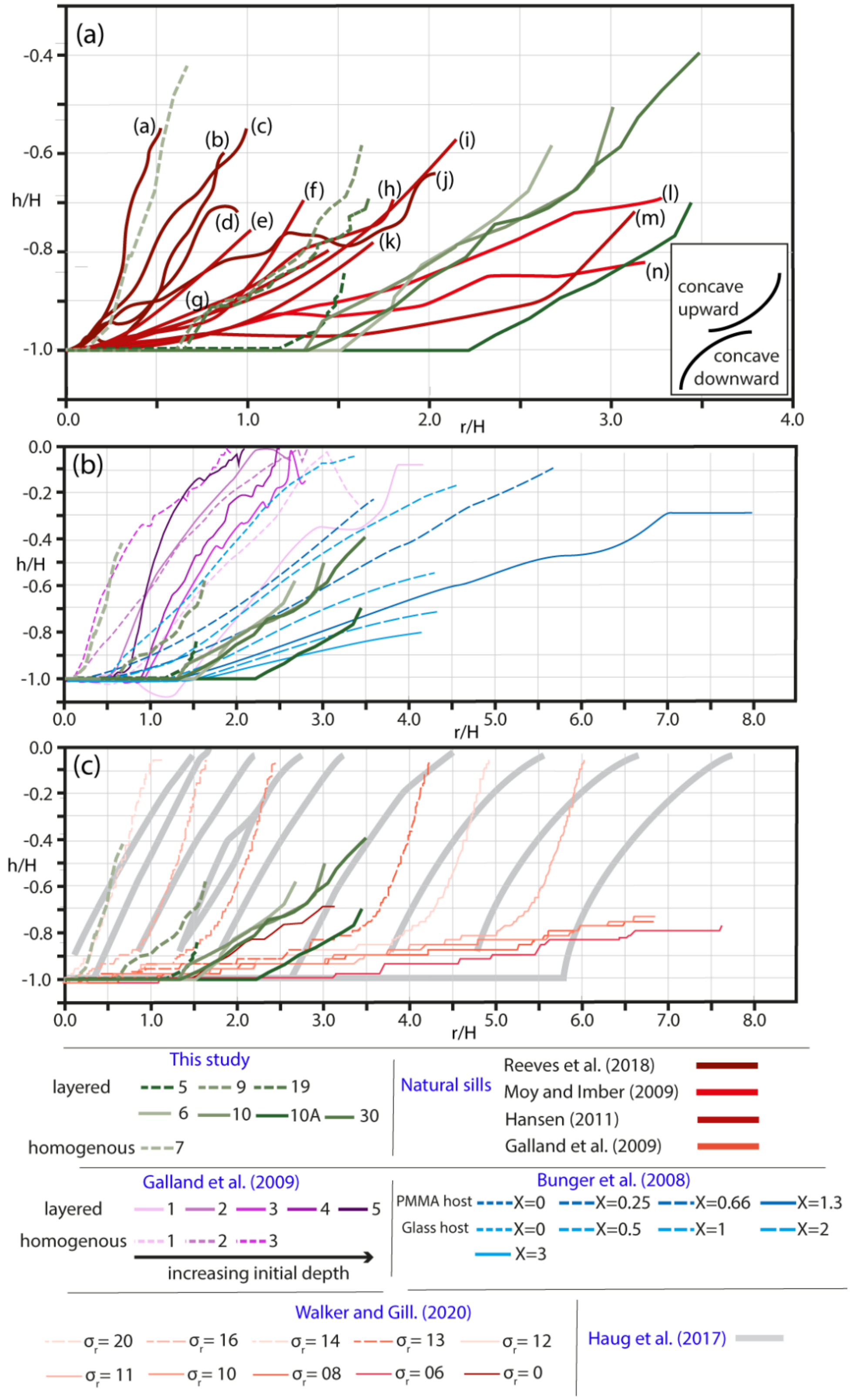

Figure 3.9. *A comparison of normalised saucer-shaped sill profiles from this study with (a) nature, (b) laboratory experimental and (c) numerical models (modified after Walker and Gill, 2020). Except for the Golden Valley and Tulipan Sills (Fig. 3.2a), saucer-shaped sill profiles in this study are similar to*

natural examples with concave upward shapes (Fig. 3.9a). See fig. 3.2 for the details of the saucer-shaped sills in nature (fig. 3.9a; a – o).

3.4.3. Inner sill to inclined sheet transition

The transition from a flat inner sill to an inclined outer sheet, characteristic of all saucer-shaped sills, has been discussed in previous analytical, numerical and laboratory modelling studies (Pollard and Holzhausen, 1979; Polteau et al., 2008; Galland et al., 2009; Gill and Walker, 2020). These previously published models of saucer-shaped sills display either smooth (curved) or sharp inner to outer sill transitions when the magma or magma analogue intrudes homogenous or layered host rocks, respectively. Our experiments produce similar smooth (Figs. 3.4a, 3.6) and sharp (Figs. 3.5, 3.6) transitions in homogenous and two-layer experiments, respectively. This suggests that layering exerts a primary control on the formation of sharp transitions to inclined sheets, but it is not a prerequisite to form saucer-shaped sills. Field observations of sills in layered host rocks also confirm the presence of sharp inner to outer sill transitions (e.g. Chevallier and Woodford, 1999; Polteau et al., 2008).

Several hypotheses have been proposed to explain the mechanics of the inner to outer sill transition. Inspired by the behaviour of near surface hydraulic fractures, linear elastic fracture mechanics (LEFM) approaches interpret this transition in the framework of the interaction between horizontally growing cracks and Earth's free surface (Pollard and Holzhausen, 1979; Fialko et al., 2001; Malthe-sørenssen et al., 2004; Bunger and Detournay, 2005; Bunger et al., 2005, 2008; Gill and Walker, 2020). Numerical experiments by Malthe-Sørenssen et al. (2004) show that when sills reach a radius approximately equal to the overburdan thickness (i.e., $r/H \sim 1$), their shapes start to become asymmetrical, which results in inflation induced bending of the overburdan. Consequently, the stress in front of the sill tip becomes asymmetrical and the sill branches upwards. Fialko (2001) theoritically predicted that the inclination, θ_i, of the outer sill should vary from 1° to 35° as r/H changes from 0.5 to 5, respectively. These theoretical θ_i values are within the range of those observed in natural saucer-shaped sills, where θ_i = 10° to 30° (Malthe-Sørenssen. et al., 2004; Galland et al., 2009).

In comparison, in assuming that the host rocks are Mohr-Coulomb materials, numerical limit analysis by Haug et al. (2017) which turned off the tensile criterion, suggests that the inner to outer sill transition occurs due to the formation of a localized plastic shear damage zone (or shear failure zone) at the tip of a growing sill. In this model, the inflating inner flat sill triggers the formation of shear failure zones that propagate from the sill tip to the Earth's surface, which then provides an inclined pathway for subsequent magma flow and outer sill formation. However, all of the saucer-shape sill profiles of Haug et al. (2017) have inclination angles, $\theta_i \geq 60°$, which is much steeper than those observed in nature. The magma overpressure required for shear failure of the overburden in Haug et al.'s (2017) model varies from 100's of MPa to 60MPa for sills with $r < 2$ km and few MPa for larger sills with $r > 2$ km. However, magma overpressure estimates in nature are typically in the range of 1 – 20 MPa (Rubin, 1995). Therefore, Haug et al. (2017) argue that localized shear failure of the overburden is only favoured for larger sills ($r > 2$ km) when $r/H > 1$. Localized shear failure of the overburden during saucer-shaped sill formation has also been verified in laboratory experiments that used Mohr-Coulomb, elasto-plastic host rock analogues, in which the formation of inclined outer sheets was attributed to plastic deformation and the formation of shear zones (Galland et al., 2009; Mathieu et al., 2008).

In comparison, our experimental saucer-shaped sills have outer sill inclination angles, $\theta_i = 15°$-$25°$ and the inner to outer sill transition occurs when $0.5 \leq r/H \leq 2.5$, with no evidence for shear faulting in the LRD host material at the onset of inclined sheet formation. Therefore, the experiments reported here do not support a model of inelastic damage as a mechanical precursor for inclined sheet emplacement. Our experimental results are more compatible with LEFM models, in which saucer-shaped sills form as a consequence of asymmetrical stress fields generated by inflation of the inner flat sill and its elastic interaction with its surroundings and the free surface (Pollard and Holzhausen, 1979; Malthe-Sørenssen et al., 2004). This is supported by the sill profiles in Figure 3.5, which show that the outer inclined sills start to propagate upwards when r/H reaches values of 0.5 to 2.5. At this point, the sills climb upward with shallow inclinations (i.e. $15° \leq \theta_i \leq 25°$) due to a change of the stress field, which is linked to the onset of overburden uplift.

3.4.4. Comparison of experimental and natural saucer-shaped sill profiles

Vertical profiles of the experimental sills reported here are compared with natural saucer-shaped sill profiles in Figure 3.9a (modified after Walker and Gill, 2020) in which the intrusion height, h, and radius, r, are normalised by the overburden depth, H. The inner sill to inclined outer sheet transition in natural saucer-shaped sills occurs when r/H = 1 to 4 (Fig 3.9a; Malthe-Sørenssen. et al., 2004; Galland et al., 2008) and the corresponding outer sill inclination angles,

θ_i = 10 - 30°, are similar to our experimental results. Inclined outer sheets in nature typically initiate with a lower inclination angle that increases towards the surface, so they have concave upward profiles (Gill and Walker, 2020). Except for the Golden Valley and Tulipan Sills, which have r/H > 3.5 (Fig. 3.2a), all of the normalised natural saucer-shaped sill profiles plotted in Figure 3.9a share similar geometric features (i.e., h/H and r/H ratios, θ_i angles and concave upward shapes) with our experimental results.

The normalised profiles of saucer-shaped sills modelled in the laboratory by Bunger et al. (2008) and Galland et al. (2009) have steeper outer sill inclination angles with concave downward shapes in contrast to the experiments reported here (Fig. 3.9b). Bunger et al. (2008) used glass and polymethyl methacrylate (PMMA) as brittle-elastic host rock analogues and water, glycerine or glucose syrup as the magma analogue. They also introduced a dimensionless fracture toughness number, $\chi = \frac{\sigma_r \sqrt{H}}{K_c}$ where K_c is the fracture toughness of the host material (Fig. 3.8b). In their experiments, the inner to outer sill transition occurs when $0 \leq r/H \leq 2$, increasing with increasing χ-value (i.e., with increasing emplacement depth, horizontal compressive stress, or decreasing fracture toughness). Bunger et al.'s (2008) experimental sills have inclined outer sheet inclinations 15° < θ_i < 30°, which, except for their concave down profiles, is similar to both our model results and natural saucer-shaped sills (Fig. 3.9b).

Galland et al.'s (2009) laboratory experiments used elasto-plastic silica powder and vegetable oil as host rock and magma analogues, respectively (Fig. 3.9b). The injected oil formed cone sheets or vertical dykes within homogenous models whereas saucer-shaped intrusions formed in layered experiments where a mesh is placed between the layers. The inner to outer sill transition in their layered models occurs when r/H ~ 0.5 - 1.5 with outer sill inclinations 40° < θ_i < 50°. However, these inclinations are steeper than those in nature and they also have strongly concave downward profiles.

In the numerical experiments by Haug et al. (2017), the inner-outer sill transition is prescribed by a fixed initial sill radius, which varied effectively from ~ 0.5 to 6 km. In their models, the outer sheet inclinations (θ_i) adjacent to the inner sill are much steeper ($\theta_i \geq 60°$) than that those observed in this study and in nature, and they also have strongly concave downward profiles (Fig. 3.9c).

Recent numerical modelling by Gill and Walker (2020) and Walker and Gill (2020) used axisymmetric finite-element calculations to investigate how a compressive horizontal tectonic stress (σ_r) changes the geometry and aspect ratio of saucer-shaped sills (Fig. 3.9c). Their model considered tensile fracture and shear failure crack tip separation mechanisms, and the input parameters were magma overpressure, host rock elasticity and the externally applied tectonic stress. In their analysis, when $\sigma_r = 0$ MPa, the inner to outer transition occurs when r/H = 1.5, $\theta_i \sim 25°$, and the resulting outer sheet has a concave upward profile, in good agreement with our results. Walker and Gill (2020) showed that as σ_r increases (0 MPa $\leq \sigma_r \leq$ 5 MPa), saucer-shaped sills form with increasingly wider inner sills (1.5 $\leq$ r/H $\leq$ 4.5) and shallower outer sill inclinations (25° $< \theta_i <$ 1°). However, for 5 MPa $\leq \sigma_r \leq$ 10 MPa, θ_i is constant at 1° and r/H reduces to 0.5 from 4.5 (Fig. 4 in Walker and Gill, 2020). Furthermore, they concluded that the model results for 5 MPa $\leq \sigma_r \leq$ 10 MPa show a good fit to natural saucer-shaped sills, and that the sill tips propagate by Mode I tensile failure. However, when $\sigma_r >$ 10 MPa, r/H < 0.5 and θ_i increases up to 45°, and sill tips propagate by host rock shear failure (Fig. 3.8c).

In many of the laboratory (Bunger et al., 2008; Galland et al., 2009) and numerical simulations (Haug et al., 2017) reviewed above, the resulting saucer-shaped sills have concave downward inclined outer sheets with steep inclination angles. This contrasts with inclined outer sheets in most natural examples, which are concave upward with shallow inclination angles (Walker and Gill, 2020) (Fig. 3.9a). Numerical simulations by Gill and Walker (2020) and Walker and Gill (2020) show that a strong compressive stress regime is required to match the geometry of natural saucer-shaped sills. However, the h/H and r/H ratios, outer sheet inclination angles and concave upward shapes observed in our experiments closely match the geometries of natural saucer-shaped sills, without the imposition of a horizontal tectonic stress. Therefore, the experiments presented here highlight the importance of host-rock rheology (i.e., visco-elastic-plastic) for saucer-shaped sill formation, in addition to the possible contribution of horizontal stress boundary conditions.

3.5. Conclusions

We have described the results of laboratory modelling of saucer-shaped sill intrusions, in which paraffin oil (magma analogue) was injected at a constant volumetric flow rate into a homogenous or two-layer model crust made of visco-elastic-plastic Laponite RD® (LRD) gel. The resulting experimental saucer-shaped sills form by the interaction between the outwardly propagating and vertically inflating sill and the overburden its overlying free surface. Our main findings are:

1. Saucer-shaped sills emplaced into homogenous LRD have the shortest inner sill diameter, a smooth transition into inclined sheet and steeply inclined outer sill compared to two-layer experiments.

2. In two-layer experiments, saucer-shaped sills develop with a flat-lying inner sill that followed the L1/L2 interface and an inclined outer sheet that propagates through the upper layer towards the model surface. The inner sill to inclined outer sheet transition is sharp and occurs over a range of inner sill radius to overburden depth (r/H) ratios between 0.5 and 2, which increase with decreasing Young's modulus or rigidity ratio (E_r) and increasing volumetric injection rate.

3. The horizontal growth rate of all saucer-shaped sill intrusions is uniform for all values of E_r and a constant volumetric flux rate (Q_i = 1ml/min). However, for the same E_r, the growth rate increases when Q_i is increased (Exp 10A; Q_i = 5 ml/min).

4. The saucer-shaped sills that formed in our experiments are compatible with brittle-elastic (LEFM) models in which the inner sill to outer inclined sheet transition occurs due to an elasticity-dominated interaction between the growing inner sill and the surrounding material and free surface. However, as discussed in Arachchige et al. (Chapter 4), marginal lobes and finger-like segments observed in most experiments are more likely linked to small-scale visco-plastic instabilities occurring at the tip of the propagating sills. This suggests the operation of scale-dependent deformation processes, with brittle-elastic (LEFM) processes dominating at the whole of intrusion scale and visco-plastic processes dominating at the crack tip scale.

5. Experiments suggest that there is no strict requirement of high horizontal stresses to form natural saucer-shaped sill geometries and show the importance of host rock rheology of making complex sill geometries.

Acknowledgements

We gratefully acknowledge support from an Australian Research Council Discovery Grant (DP190102422) to A.R.C. and Dean's International Postgraduate Research Scholarship (DIPRS) and Graduate Research Completion Award (GRCA) scholarship from Monash University (Melbourne) to U.S.N.A.

Chapter 4

Laboratory Modelling of Sill Emplacement: Part 2 – sill segmentation

Uchitha N. Arachchige[1], Alexander R. Cruden[1], Roberto Weinberg[1]

[1]School of Earth, Atmosphere and Environment, Monash University, 9 Rainforest Walk, Clayton, VIC 3800, Australia

Abstract

It is increasingly recognised that most sheet-like igneous intrusions such as sills and dykes have segmented, rather than planar margins. The geometry of these segments and their connectors can provide insights into magma propagation pathways and host-rock deformation mechanisms during their emplacement. Here we report the results of scaled laboratory experiments on the emplacement of shallow-crustal, saucer-shaped sills with a focus on their propagation and segmentation. Visco-elasto-plastic Laponite RD® (LRD) and Newtonian paraffin oil were used as analogues for layered upper crust rocks and magma, respectively. Our results indicate that: 1) experimental saucer-shaped intrusions are highly segmented with marginal lobes and fingers; 2) the evolution and geometry of marginal segments and their connectors are different within the horizontal inner sill and the inclined outer sill; and 3) the bimodal nature of segment aspect ratios is linked to propagation of the inner sill along a horizontal host-rock interface versus interaction of the inclined outer sill with a homogenous upper layer. Measurements of inlet magma pressure and structural analysis suggest that marginal finger and lobe segments propagate in a repetitive sequence that starts with segmentation, followed by merging of segments and new growth of fingers/lobes. Based on the 3D geometry of segments, we suggest that sill segmentation is linked to smaller scale visco-plastic instabilities that occur within the inner sill and large scale mixed mode (I+III) fracturing during the inclined sheet propagations.

4.1. Introduction

Igneous sheet intrusions, such as sills and dykes, play a dominant role in magma transport over large distances within the Earth's crust (Anderson, 1937; Ernst et al., 1995). These intrusions are genreally considered to be planar bodies that interconnect to build complex sub-horizontal and sub-vertical magma plumbing systems (Magee et al., 2016; Muirhead et al., 2016; Cruden and Weinberg, 2018). However, field observations and 3D seismic surveys find that most sheet intrusions are segmented at their propagating margins into laterally and/or vertically offset magma lobes or fingers (Fig. 4.1) (Pollard et al., 1975; Thomson and Hutton, 2004; Hansen and Cartwright, 2006; Magee et al., 2016). The geometries of these segments are important because they are an indicator of magma propagation directions and emplacement mechanisms (Magee et al., 2019). However, determining the links between igneous intrusion mechanisms and segmentation is challenging because: i) field and seismic observations only reflect the final stage of the emplacement process; and ii) laboratory and numerical experiments have yet to produce complex segmentation patterns that are similar to those observed in nature.

Most research on the segmentation of igneous dykes and sills has taken a Linear Elastic Fracture Mechanics (LEFM) approach, in which segments are idealised as Mode I elastic fractures with tapered (wedge-shaped) or sharp tips (Pollard, 1973; Delaney and Pollard, 1981; Rubin, 1993). However, field and seismic studies indicate that sheet intrusions have segmented margins with finger-like or lobate forms with rounded and/or blunt tip geometries (Pollard et al., 1975; Hutton, 2009; Schofield et al., 2010; Spacapan et al., 2017; Galland et al., 2019). Various anelastic mechanisms, such as host rock fluidization (Schofield et al., 2010, Köpping et al., 2021), viscous indentation (e.g. Spacapan et al., 2017), and brittle shear faulting and/or ductile flow (e.g. Pollard and Johnson, 1973; Eide et al., 2017) have been proposed for segmentation of sheet intrusions with rounded or blunt tips. Therefore, the mechanisms that explain the formation of marginal intrusion segments are still debated.

Analogue experiments of igneous intrusions such as sills and dykes are important because their geometrical evolution can be monitored in three dimensions (3D). This can enable links to observations in nature to better understand their emplacement mechanisms and propagation pathways. Previous laboratory experiments on sill emplacement using granular materials (elasto-pastic; Galland et al., 2009; Mathieu et al., 2008), polymethyl methacrylate (PMMA) and glass (elastic; Bunger et al., 2008) and gelatine (visco-elastic; Kavanagh et al., 2006) as host rock analogues, mainly focused on the formation of planar and saucer-shaped intrusions. Lobate marginal segments were produced in experiments by Chanceaux and Menand (2016) and Currier and Marsh (2015) that included the effects of solidification during the emplacement and growth of sills and laccoliths. Such previous experimental work has yet to reproduce the complex segmentation of sill margins observed in nature (Thomson and Hutton, 2004; Magee et al., 2016), and with exception of work by Bertelsen et al. (2018) has usually neglected the complex visco-elasto-plastic rheological behaviour of rocks in Earth's upper crust. The mechanics of marginal segmentation in igneous intrusions is therefore poorly constrained and many fundamental questions about segmentation processes remain unanswered. For example, is it possible to produce lobes and finger segments in a laboratory experiments of sills? How does host rock rheology influence sill segmentation geometry and processes? How do marginal segments develop in space and time during the lateral propagation of sills?

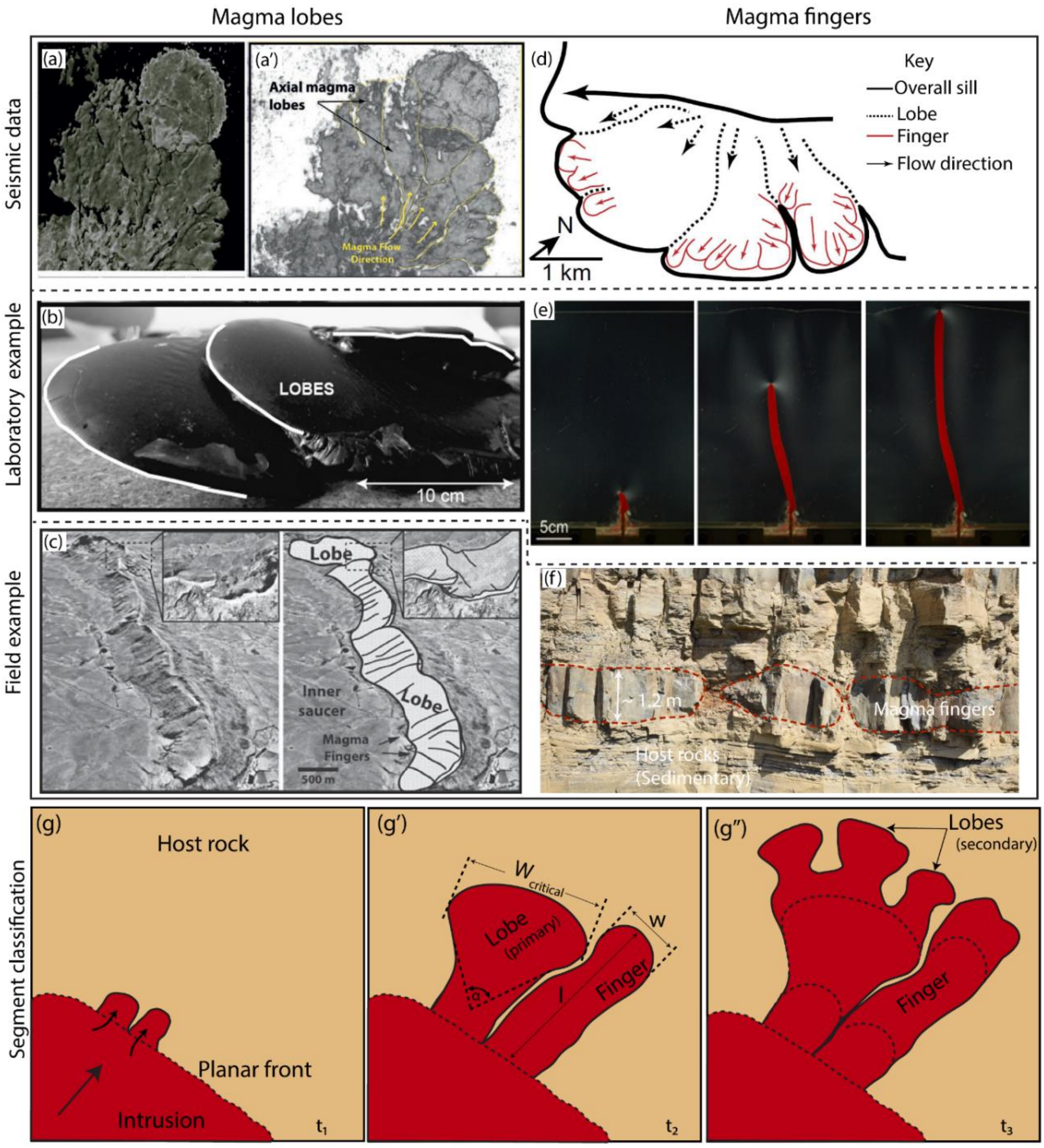

Figure 4.1: *A selection of sill segments observed in 3D seismic reflection data, field studies and laboratory experiments. (a) Magma lobes observed in 3D seismic reflection image of the Flat Ridge Sill, Faroe-Shetland Basin showing non-planar margins (from Schofield et al., 2012) and (a′) an alternative view of (a) highlighting magma lobes and flow directions. (b) Lobes formed in a solidification experiment using hot vegetable oil injected into gelatine (from Chanceaux and Menand, 2014), and (c) lobes observed at the margin of the Golden Valley sill, Karoo Basin (from Schofield et al., 2010). (d) Magma lobes and fingers mapped in 3D seismic reflection data of a sill, Rockall Trough (from Magee et al., 2015, modified after Thomson and Hutton, 2004). (e) An analogue magma finger formed in a 2D Hele-Shaw cell experiment (from Bertelsen et al., 2018), and (f) magma fingers observed in the Shonking Sag laccolith, Montana (photo curtsey of Jonas Köpping). (g) Diagram illustrating the onset of non-planar margin at time step t_1, (g′, g″) definition of lobes, with an opening angle (α) and fingers, with sub-parallel sides (α ~ 0°) at time step t_2 to t_3.*

Conversely, laboratory experiments on hydrofracturing within clay (ideally plastic material; Murdoch, 1993a, 1993b) and silica flour (elasto-plastic material; Chang, 2004; Wu, 2006) have generated complex non-planar fractures with lobe and finger segments. In a companion paper, Arachchige et al. (Chapter 3) report the results of analogue experiments using Laponite RD® (LRD), a visco-elasto-plastic host rock analogue, that focus on the formation and growth of saucer-shaped sills. Here, using a similar experimental approach, we focus on the 3D geometry and formation mechanisms of complex marginal sill segmentation. Specifically, the aims of this contribution are to: (i) identify modes of sill segmentation that occur in visco-elasto-plastic host rock materials; (ii) determine how marginal segments develop in space and time during sill propagation; and (iii) investigate how marginal segments can be used to provide insights on the kinematics and dynamics of sill emplacement.

4.2. Background

4.2.1. Segments, lobes and fingers

Many igneous sheet intrusions have highly segmented, non-planar margins (Pollard et al., 1975; Delaney and Pollard, 1981; Schofield et al., 2010; Magee et al., 2019). This segmentation often refers to the separation of originally planar intrusion margins into laterally and/or vertically offset, overlapping and/or underlapping individual structures known as *segments*, which are further subdivided into lobes and fingers (Fig. 4.1). These segments are also considered to form parallel to the propagation direction of the sheet intrusion (Schofield et al., 2012a). Moreover, at any given time during its propagation, the intrusion front may comprise two or more different segment types (i.e., lobes or fingers) with a range of sizes, which we will refer to as "complex segmentation".

In the context of igneous sills, the term *magma lobe* (Fig. 4.1) refers to a near-circular to elongated lobe-shaped geometry (Miles and Cartwright, 2010; Schofield et al., 2012). Here, we define a lobe to be a segment that widens in the intrusion propagation direction, with a positive opening angle, α between the two sides of the lobe (Fig. 4.1g′). Indeed, the formation of lobes in intrusions has been compared to pahoehoe lobes in lava flows, which form due to magma cooling and solidification at the flow front (Griffiths, 2000; Miles and Cartwright, 2010). During flow of lava, a partially chilled front is formed at the lava-water or lava-air contact, which inhibits the lateral spreading of lobes due to an increase in tensile strength. However, during continuous lava supply, internal pressure overcomes the local tensile strength of the solidified front and lava bursts open through previously solidified lobes resulting in lateral growth and formation of new pahoehoe lobes. An analogous process has also been used to explain near-circular lobe-shape geometries in sills emplaced at shallow levels, such as the Solsikke Sill (Hansen and Cartwright, 2006), Vigra sill complex (Miles and Cartwright, 2010) and Golden Valley Sill (Schofield et al., 2010).

The term *magma finger* (Fig. 4.1) commonly describes elongated, narrow segments with an array of blunt and/or bulbous-ended tubes in dykes and sills (Pollard et al., 1975; Schofield et al., 2010; Spacapan et al., 2017; Galland et al., 2019). Here we define a finger as a parallel sided segment with an opening angle $\alpha \sim 0°$. Fingers mostly propagate along the same stratigraphic level and can be a few centimetres to hundreds of meters long (Magee et al., 2018a). However, small vertical offsets of fingers may occur due to the exploitation of preferentially oriented, pre-existing weaknesses, which result in inconsistent stepping directions (Magee et al., 2019). Vertically and horizontally separated fingers can later coalesce, developing cusp-shaped grooves in between them (Pollard et al., 1975; Schofield et al., 2010, 2012a). The emplacement of magma fingers is commonly attributed to: i) viscous fingering instabilities (e.g., Saffman-Taylor instability) between a propagating magma front and a fluidised host rock (Pollard et al., 1975; Schofield et al., 2010); or ii) mixed mode (Mode I+III) fracturing within an elastic host material (D. Pollard and Johnson, 1973; Pollard et al., 1982).

4.2.2. Segment connectors

Segment *connectors* connect overlapping and/or underlapping segments. Known as steps, bridges, broken bridges and en-echelon structures (Fig. 4.2), they are often attributed to brittle magma emplacement mechanisms (Schofield et al., 2012a; Nicholson and Pollard, 1985; Hutton, 2009). Delaney and Pollard (1981) defined bridges as ‘curved slabs of rock that separate two neighbours in the echelon array’. Bridges of host rock strata (Fig. 4.2a) occur when two separate overlapping, vertically offset segments propagate simultaneously. As continuous magma supply inflates the segments, bending of the intervening host rock strata occurs, resulting in a bridge structure (Schofield et al., 2012a). If further inflation and bending occurs, tensile fractures eventually develop perpendicular to the bridge axis, close to the zones of maximum flexure, forming a broken bridge between overlapping segments. Once bridges detached from both ends, they become xenoliths, or ‘bridge xenoliths’ within segments (Rickwood, 1990).

Steps form from initially vertically offset segments or en-echelon intrusion tips, which later coalesce into a single sheet as an intrusion propagates and inflates (Fig. 4.1b) (Schofield et al., 2012a; Eide et al., 2017). Steps between connected segments are oriented perpendicular to the direction of magma flow (Schofield et al., 2012b).

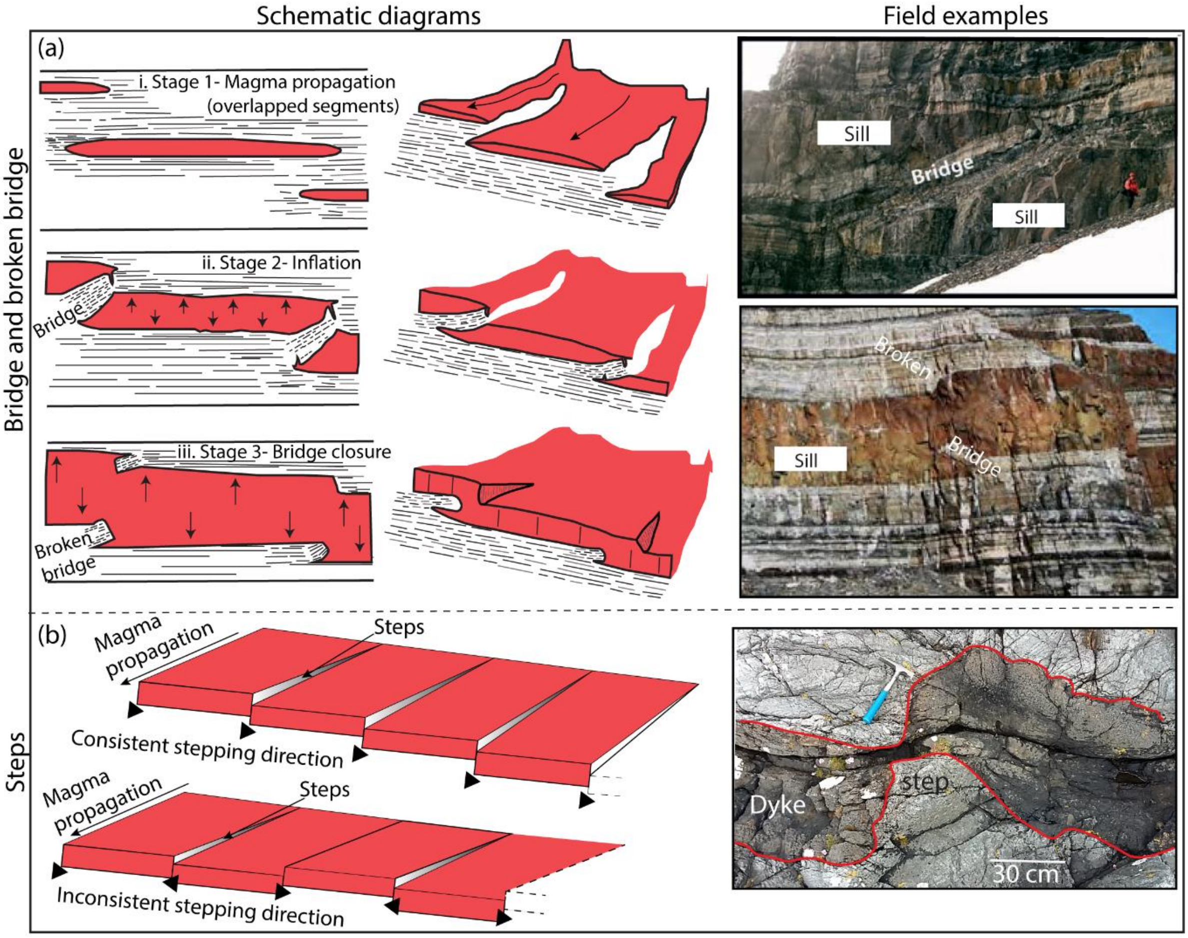

Figure 4.2: *A summary of segment connectors. (a) Left: schematic diagrams of bridge and broken bridges in cross-section and 3D in relation to: (i) overlapping segments; (ii) segment inflation; and (iii) bridge closure (after Eide et al., 2016). Right: field examples from the Theron Mountains, Antarctica (modified after Hutton, 2009). (b) Left: schematic diagrams of en-echelon steps in sills with consistent and inconsistent stepping directions. Right: steps developed in Mesozoic limestone and shale metasedimentary strata on Ardnamurchan, NW Scotland (modified after Magee et al. 2018).*

4.3. Experimental methods

This is the second of two companion papers that report the results of scaled laboratory experiments on the emplacement of sills in layered and non-layered elasto-visco-plastic analogue host rock materials. The complete series of laboratory experiments are described in Part 1 (Arachchige et al., Chapter 3), which focuses on the development of saucer-shaped sills. Here, in Part 2, we focus mainly on experiments in which saucer-shaped sills propagate with highly segmented margins with complex geometries.

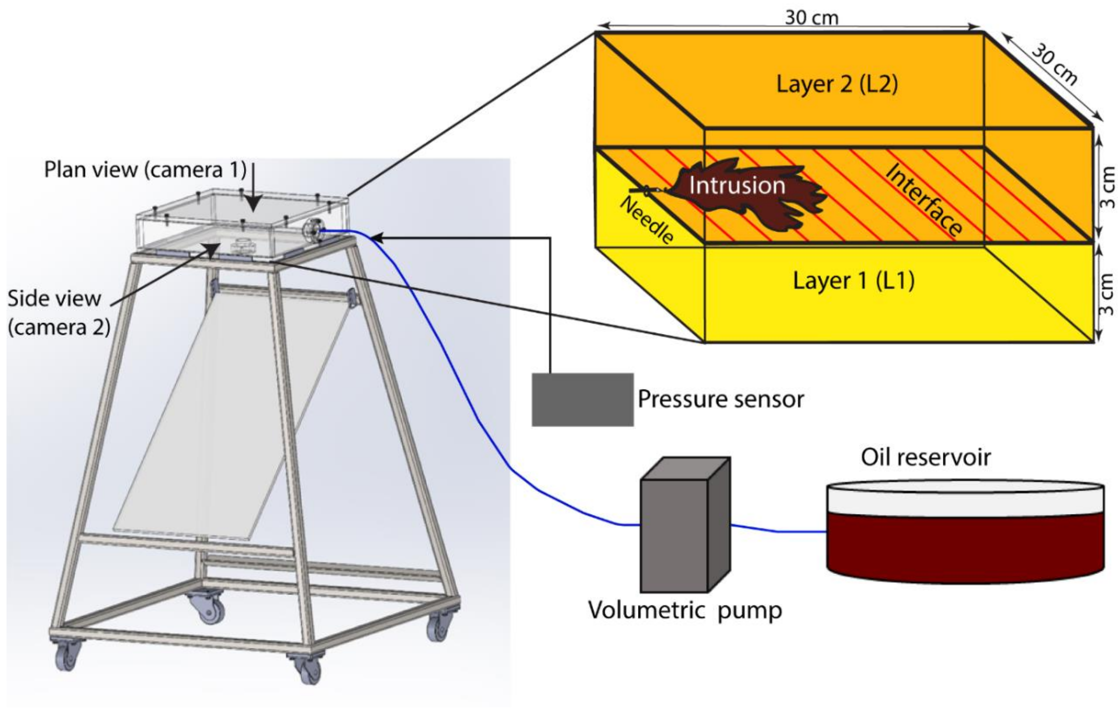

Figure 4.3: *Schematic diagram of the experimental setup (modified after Arachchige et al., Chapter 2). A volumetric pump injects paraffin oil into homogenous or layered Laponite RD® though a fixed hole using a needle. Two DSLR cameras capture the intrusion growth from top and side views respectively. The pressure sensor connects to the fluid flow just before the injection needle.*

The experimental setup comprises a plexiglass tank (30 cm x 30 cm x 6 cm) filled with elasto-visco-plastic Laponite RD® (LRD; Arachchige et al., 2021), the upper-crustal rock analogue (Layer 1 [L1] and Layer 2 [L2], Fig. 4.3). Paraffin oil (magma analogue) is injected horizontally into the interface between two 3 cm thick layers of LRD using a 2 mm diameter tapered needle via a nozzle at the side of the tank, which is fed at a controlled volumetric flow rate either by a peristaltic pump or a syringe pump. In all experiments, the Young's modulus of the upper (E_u) and the lower (E_L) layers are varied by changing the wt. % concentrations X_u and X_L of LRD in water. All other parameters such as the analogue magma volumetric flow rate (Q_i) and viscosity (μ), and the intrusion depth (3 cm) are constant. Propagation of the model intrusions is monitored by high-resolution DSLR cameras (Fig. 4.3) placed above and at the side of the experiment, providing plan and cross-sectional views, respectively. Two experiments (exp. 5, 6) were repeated using a syringe sump and a digital pressure sensor to measure pressure variations at the inlet of the intrusion (Fig. 4.3). The pressure sensor was calibrated to correct for any background signals from the syringe pump. Therefore, the pressure signals reported here only represent the fluid pressure at the inlet during the emplacement and growth of the model intrusions.

4.3.1. Model materials and scaling

We use Laponite RD® (LRD), a gel-forming grade of synthetic smectite clay manufactured by BYK Additives and Instruments (2014) and paraffin oil as the crustal host rock and magma analogues, respectively. When mixed with water, LRD forms a colourless, transparent and photo-elastic gel, which is similar to gelatine but chemically and biologically more stable (Ruzicka and Zaccarelli, 2011). LRD has lower surface energy values (24 - 44 mJ/m^2; Norris et al., 1993) compared to gelatine, a frequently used intrusion host rock analogue (1 J/m^2; Kavanagh et al., 2013). This ensures that surface tension dynamics are minimized in geological analogue experiments using LRD. The mechanical properties of LRD, such as Young's modulus, can be easily varied by changing its concentration and curing time (Arachchige et al., 2021). Arachchige et al. (2021) recently showed that LRD is suitable for analogue modelling of visco-elasto-plastic rock deformation, including elastic and plastic end member behaviours. Shear strains, $\gamma < 10\%$ and strain rates of up to 0.01 s^{-1} for concentrations from 2 wt. % to 4 wt. % and a curing time of 72 hours must be maintained to model elastic dominant deformation. LRD starts to yield at a shear strain $\gamma = 10$ % for concentrations 2 wt. % to 4 wt. % with yield strength values varying from 25 to 200 Pa, respectively. Higher shear strains ($\gamma > 26.2$ %) and strain rates $\dot{\gamma} \geq 0.01$ s^{-1} must be maintained to model plastic deformation. We use the Young's modulus value of LRD as the main host rock variable and, following Arachchige et al. (2021), assume that LRD is incompressible with Poisson's ratio = 0.5. Paraffin oil (magma analogue) has a viscosity of 0.16 Pa s at 22.5 °C and, unlike water, it does not react with LRD. Paraffin oil was mixed with red dye to provide a better visual contrast with the host material without altering its viscosity.

Table 4.1. *Symbols, units and values of variables in nature and model*

Parameter	Dimension	Definition	Value		
			Nature (p)	Model (m)	Ratio*(m/p)
ρ_h	Kg m^{-3}	Density of host rock	2800	1000	0.357
ρ_i	Kg m^{-3}	Density of intrusions	2700	850	0.3
g	m s^{-2}	Gravity acceleration	9.81	9.81	1
V_i	m s^{-1}	Velocity of intrusion	0.2	10^{-5}	5 x 10^{-5}
L	m	Length	100	0.01	10^{-4}
t	s	Time	-	900-2700	2 x 10^{-2}
µ	Pa s	Viscosity of intrusion	2.2 x 10^5	0.16	7.14 x 10^{-7}
Q_i	m^3 s^{-1}	Volumetric flow rate of intrusion	(0.02 - 13.28)	8.3 x 10^{-9}	(6.25 x 10^{-10} - 3.75 x 10^{-7})

Stress scaling factor	**$\sigma^* = \rho^* g^* L^* \rightarrow \sigma^* = 3.57 \times 10^{-5}$** Model is 10^5 times weaker than in nature
Time scaling factor	**$t^* = L^*/V^* \rightarrow t^* = 2 \times 10^{-2}$** 1 min in model ~ 0.83 hr in nature
Viscosity scaling factor	**$\mu^* = t^*\sigma^* \rightarrow \mu^* = 7.14 \times 10^{-7}$** Model intrusion represents a magma viscosity of 10^4 Pa s
Volumetric flow rate scaling factor	**$Q^* = \Delta\rho^* L^{*3} E^{*-1} V^* \rightarrow Q^* = (6.25 \times 10^{-10} - 3.75 \times 10^{-7})$** Model represents natural flux range (0.02 – 13.28) m^3s^{-1}

The scaling of the experiments and the suitability of the model materials (Table 4.1) are described in detail by Arachchige et al. (2021) and Arachchige et al. (Chapter 3). The principle we follow is to define scaling factors for the models, which satisfy approximate geometric, kinematic and dynamic similarity to processes in nature (Hubbert, 1937; Ramberg, 1967; Galland et al., 2009).

We define the length scale factor (L*) as the ratio between the overburden depth of the sill in the prototype (subscript p) to one in the shallow crust (subscript n), which is initially taken to be 10^{-4} (1 cm in the laboratory represents 100 m in nature). The ratio between the density of LRD in the experiments and that of natural host rocks (ρ*) is ~ 0.36 and the gravitational acceleration is the same in our experiments and in nature (g* = 1). Thus, the stress scaling factor is:

$$\sigma^* = \rho^* g^* L^* = 3.6 \times 10^{-5} \quad (4.1)$$

We compare the average model intrusion velocity of ~ 1 x 10^{-3} ms^{-1} to an estimated natural magmatic intrusion velocity of 0.2 ms^{-1} (within a range between 0.1 ms^{-1} and 0.5 ms^{-1} ;Spence and Turcotte, 1985; Kavanagh et al., 2013), which gives a velocity scaling factor, V* = 5 x 10^{-3}. We can now define the time scaling factor as

$$t^* = L^*/V^* = 2 \times 10^{-2} \tag{4.2}$$

Therefore, 1 min in our experiments represents 0.83 hr in nature. Using σ* and t*, the viscosity scaling factor becomes

$$\mu^* = \sigma^* t^* = 7.2 \times 10^{-7} \tag{4.3}$$

so paraffin oil (magma analogue) with a viscosity of 0.16 Pas is equivalent to a magma in nature with a viscosity of 10^4 Pas, consistent with basaltic andesite with low crystal content (Mathieu et al., 2008).

The measured Young's modulus, E, of LRD concentrations after 7 days curing time used in the experiments is 10^3 - 10^4 Pa. Since E of upper crustal sedimentary rocks is typically in the range of 10^9 - 10^{10} Pa (Kavanagh et al., 2013), the Young's modulus scaling factor, E* in our experiments is 10^{-7} – 10^{-5}. Therefore, based on σ* and E* our model host rock is 10^5 times weaker than in nature.

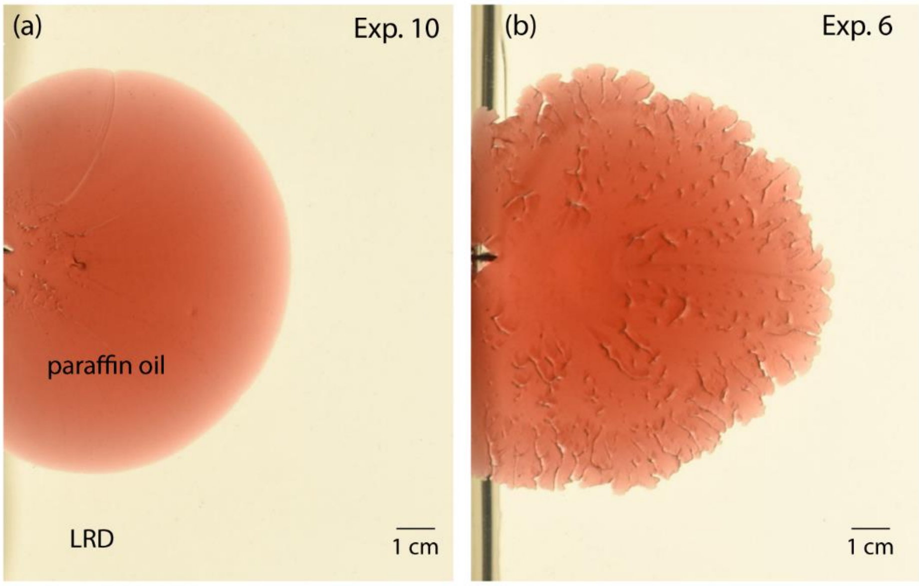

Figure 4.4: *(a) Comparison of the margins of experimental sills in plan-view. (a) Exp. 10 (E_r = 1) shows simple planar front whereas (b) Exp. 6 (E_r = 1) is highly segmented with finger and lobate geometries.*

4.4. Results

Here we focus on five experiments (Table 4.2) in which saucer-shaped sills formed with highly segmented intrusion fronts and complex geometries. In all experiments, an initial, flat, penny-shaped inner sill propagates along the interface between the two layers of LRD. This sill then bends upwards and intrudes the upper layer as an inclined outer sheet to form a saucer-shaped intrusion before the analogue magma erupts onto the model surface. Except for Exp. 10 (Fig. 4.4a) where the sill margin is planar, the propagating fronts of all intrusions are highly segmented with lobes and fingers. We further categorise these segments as being first (primary) and second (secondary) order (Figure 4.1g), discussed below.

The propagating margins of sills in our experiments have more complex geometries than the planar cracks that are typically formed in models using granular elasto-plastic (Mathieu et al., 2008; Galland et al., 2009) or visco-elastic (e.g., gelatine; Kavanagh et al., 2006) host materials. The inner flat sill and the outer inclined sheet of the saucer-shaped intrusions in our experiments have dominantly non-planar margins characterised by lobes and finger-like segments (e.g., Exp. 6; Figs. 4.4 and 4.5).

Table 4.2. *Summary of experiments and parameters*

No	X_{LL} (wt. %)	ρ_{LL} (kg m^{-3})	E_{LL} (Pa)	X_{UL} (wt. %)	ρ_{UL} (kg m^{-3})	E_{UL} (Pa)	E_{UL}/E_{LL}	comments
5	3	1050	5013	4	1075	10266	2.05	Flat sill to inclined saucer
6	3	1050	5013	3	1050	5013	1	Flat sill to inclined saucer
9	3.5	1060	8317	4	1075	10266	1.23	Flat sill to inclined saucer
30	3.5	1075	8317	3.5	1060	8317	1	Flat sill to inclined saucer
10	4	1075	10266	4	1075	10266	1	Flat sill to inclined saucer

X = concentration of Laponite RD® (LRD) in deionised water (wt. %); ρ is density of LRD (kg m^{-3}); E = Young's modulus of LRD (Pa). Rigidity ratio (E_r) = E_{UL}/E_{LL}

Subscripts LL = lower layer and UL = Upper Layer.

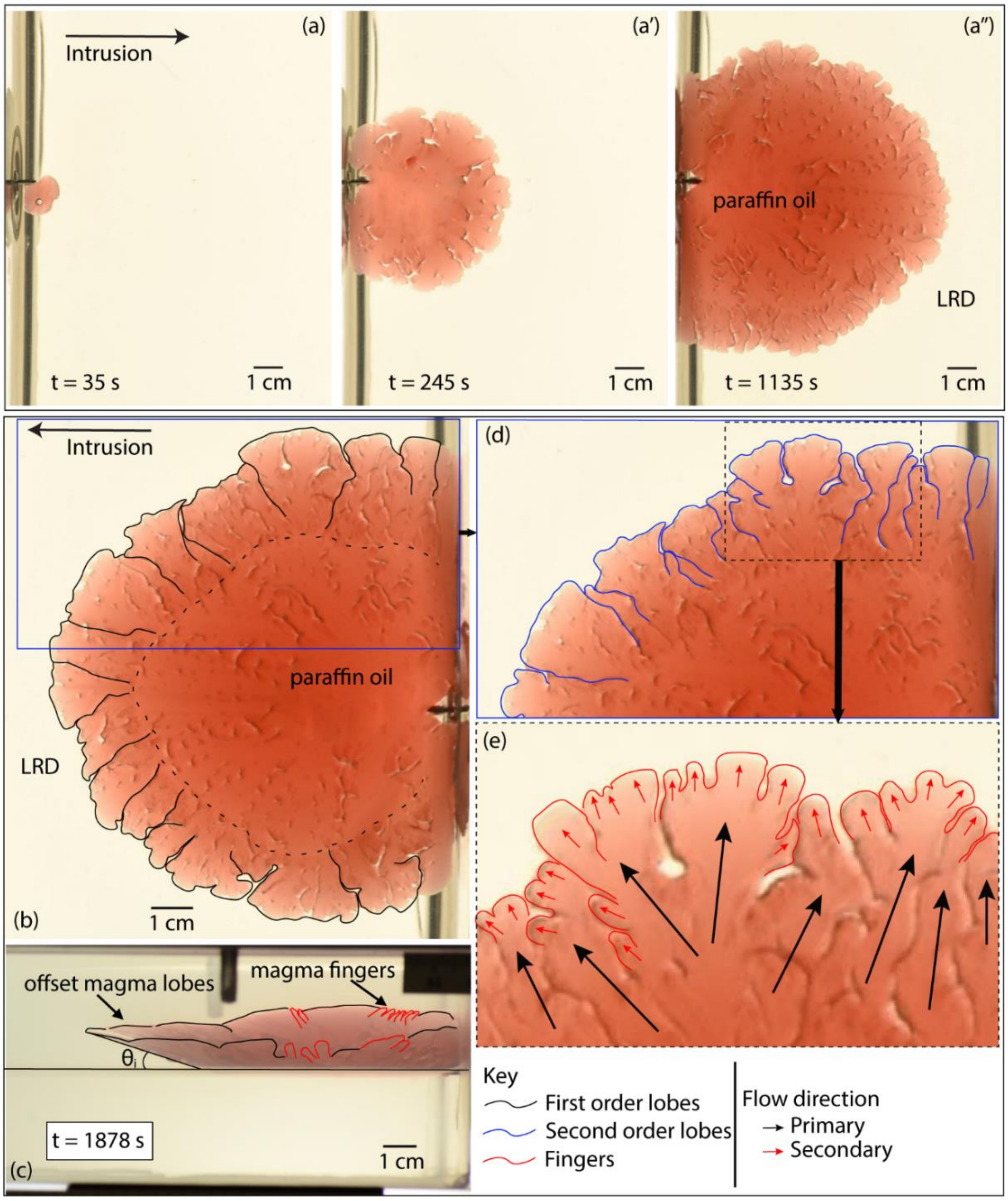

Figure 4.5: *Non-planar sill margin and segmentation formed in Exp. 6: (a-a") Plan view images. Paraffin oil (red) is injected from the left through a needle into transparent Laponite RD® (LRD). Arrow indicates sill propagation direction. (b) Plan view at a later time step than (a") rotated and magnified for a comparison with side view (c). The sill expands radially and breaks into lobes and fingers. Lobe segments show distinct 1st order (i.e. primary lobes, outlined in black) and 2nd order (i.e. secondary lobes, outlined in blue; or finger-like segments, outlined in red). The corresponding primary and secondary flow directions within the sill are shown ad black and red arrows, respectively. The dashed black line in (b) represents the transition from the horizontal inner sill to the inclined outer sheet, defining the saucer-shaped geometry observed in side view in (c). Vertically offset lobes and fingers only formed within the inclined sheet. θ_i is the dip of the inclined sheet. (d) and (e) are magnified sections of (b) and (d), respectively.*

Taking Exp. 6 as a representative example, the inner sill is initially penny shaped with a planar margin that is confined to the interface between the two LRD layers (Fig. 4.5a). At t = 245 s the sill margin starts to break down into segments (Fig. 4.5a′, 4.5b). At this early stage, the segments are relatively large 1st order lobes fed by primary fluid flow vectors (Fig. 4.5d). Upon reaching a critical width, these segments bifurcate into smaller, second order lobes and fingers fed by secondary fluid flow vectors (Fig. 4.5e and supplementary Movie 1; Appendix 2). As the inner sill propagates along the L1/L2 interface the segments evolve in the sequence: (1) fingers/lobes form at the intrusion front, (2) fingers/lobes merge laterally (i.e. segment coalescence), becoming wider, and (3) these break down again into narrower, secondary fingers/lobes. The segments that develop during propagation of the inner sill are also two dimensional (2D) structures confined to the L1/L2 interface.

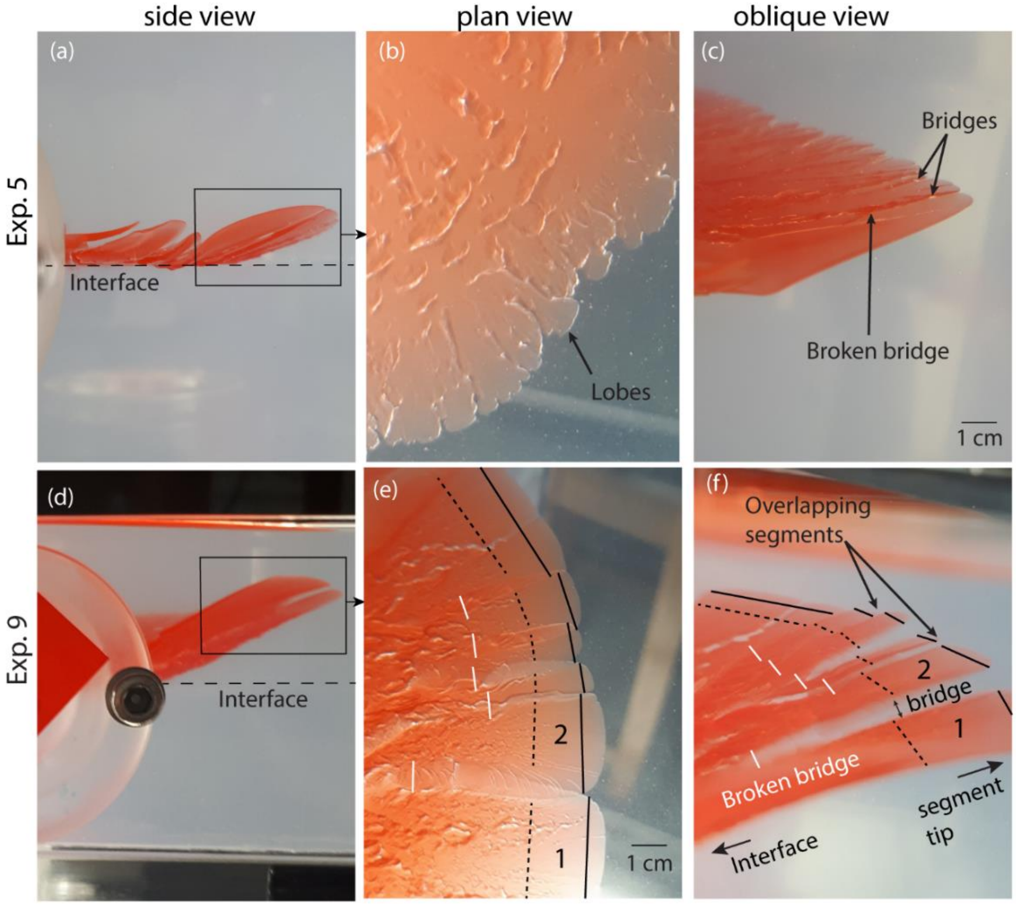

Figure 4.6: *Formation and evolution of segment connectors in Exp. 5 and 9 within inclined outer sheets in side (left), plan (middle) and oblique (right) view. In Exp. 5 (a-c) and Exp. 9 (d-f) the propagation front is non-planar and characterised by vertically displaced overlapping lobes. Bridges form closer to the centre of adjacent segments (e.g., dotted lines in segment 1 and 2; e, f) and broken bridges form closer to the layer interface (white lines) due to inflation of the segments (c, f). See text for details.*

Eventually the inner sill abandons the L1/L2 interface and intrudes upward into the homogenous L1 upper layer. During this new stage of sill growth, marginal segments form overlapping, en-echelon 3D structures. Figure 6 shows segments within the inclined outer sheets of Exp. 5 and 9 and the formation of segment connectors. These segments propagate along vertically and horizontally offset planes, and over time they thicken and connect resulting in segment connectors such as bridges and broken bridges (Fig. 4.6). At any given time, close to the tip of two adjacent segments (e.g., black lines in segment 1 and 2; Fig. 4.6e, 4.f), the vertical offset is higher (i.e., overlapping segments). Towards the middle of the same segments (dashed lines in; Fig. 4.6e, 4.f), a narrow space (i.e., bridge; Figs. 4.6c, 4.f) of the host rock analogue is created due to the inflation of the segment. Approaching the main body of the sill (white lines in; Fig. 4.6e, 4.f), the narrow bridge of host rock closes and overlapping segments coalesce vertically (i.e. broken bridge; Figs. 4.6f and 4.1c).

4.4.1. Aspect ratio analysis

Figure 4.7 plots the width/length (w/l) aspect ratios of lobe and finger-like segments in plan view from all experiments measured at four locations along the radius of the intrusion (C1 – C4; Fig. 4.7b). The aspect ratios of finger-like segments are < 1 and cluster at w/l ~ 0.5. This ratio decreases as the intrusion propagates from the inner sill to the inclined sheet (C1 to C4). In contrast, the aspect ratios of lobe segments define two distinct groups when plotted against length (Fig. 4.7a). The first group (Mode 1) forms while the sill propagates along the L1/L2 interface between the two LRD layers (C1 and C2). These "interface-controlled" lobe segments have constant, relatively short lengths (<0.5 cm) while the aspect ratio increases as the sill expands from C1 to C2. The second group (Mode 2) forms within the homogenous upper layer (C3 and C4). These "unconstrained" lobe segments have small aspect ratios (0.5 - 1.5) and they are up to 4 cm long. We consider Mode 2 to be unconstrained because the segments develop within the homogeneous upper layer where lobes exploit the 3D space ahead of the tip of the expanding sill. This implies that when lobes expand in a homogeneous material they tend to maintain an approximately constant aspect ratio of ~ 1 as they lengthen (Fig. 4.7b).

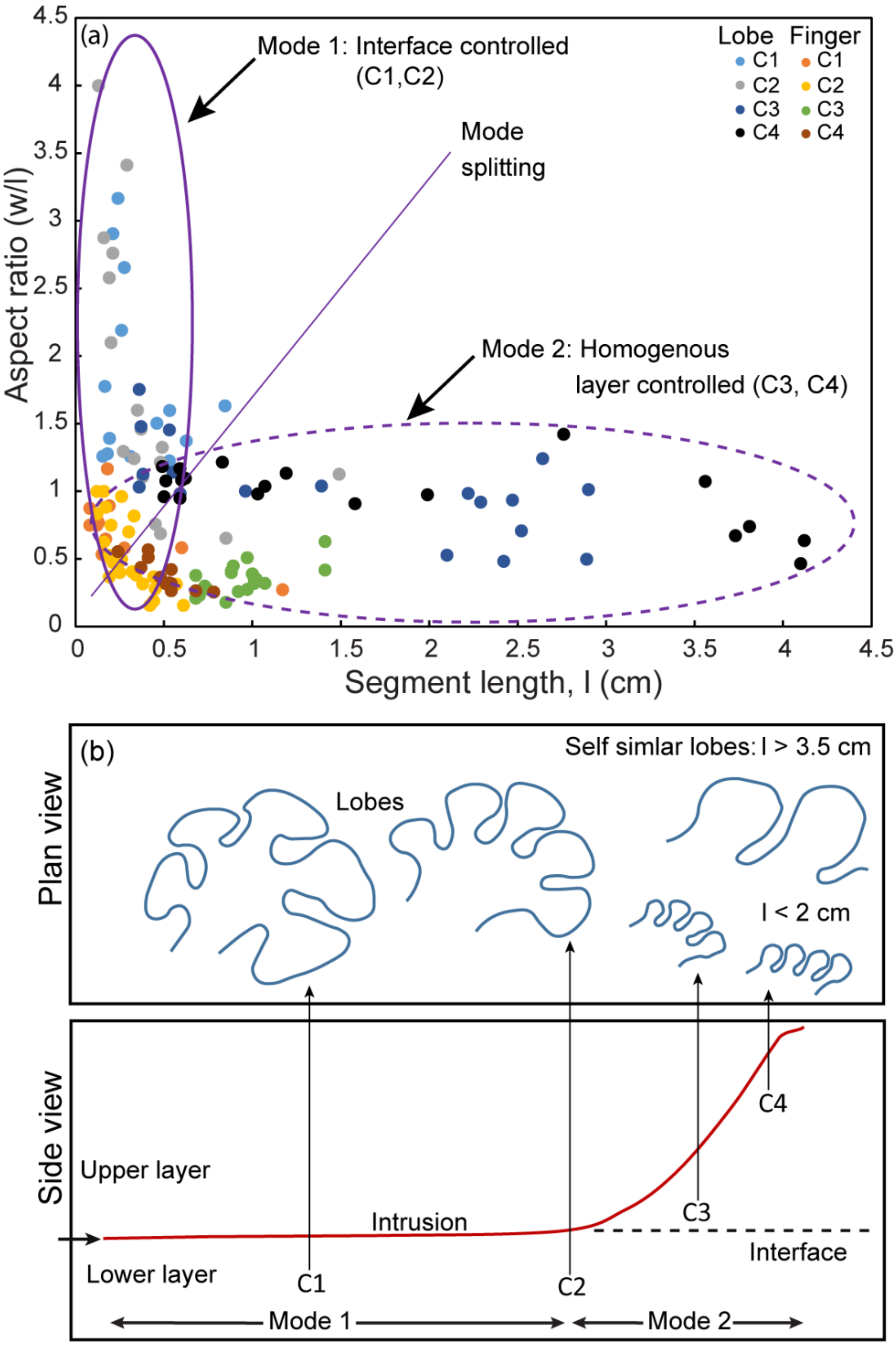

Figure 4.7: *(a) Plot of segment aspect ratio (width (w)/length (l)) versus segment length (l) measured at four locations (C1-C4) along the length of the intrusion indicated in (b) for all experiments. The two ellipses in (a) represent Mode 1 (interface-controlled) and Mode 2 (unconfined, formed within homogenous layer) type segments, respectively. Mode 1 segments are characterized by varying aspect ratios with relatively short lengths, whereas Mode 2 segments have similar aspect ratios over a range of lengths. (b) Representative plan view outlines of lobe segments at positions C1 to C4 indicated in the lower side view diagram.*

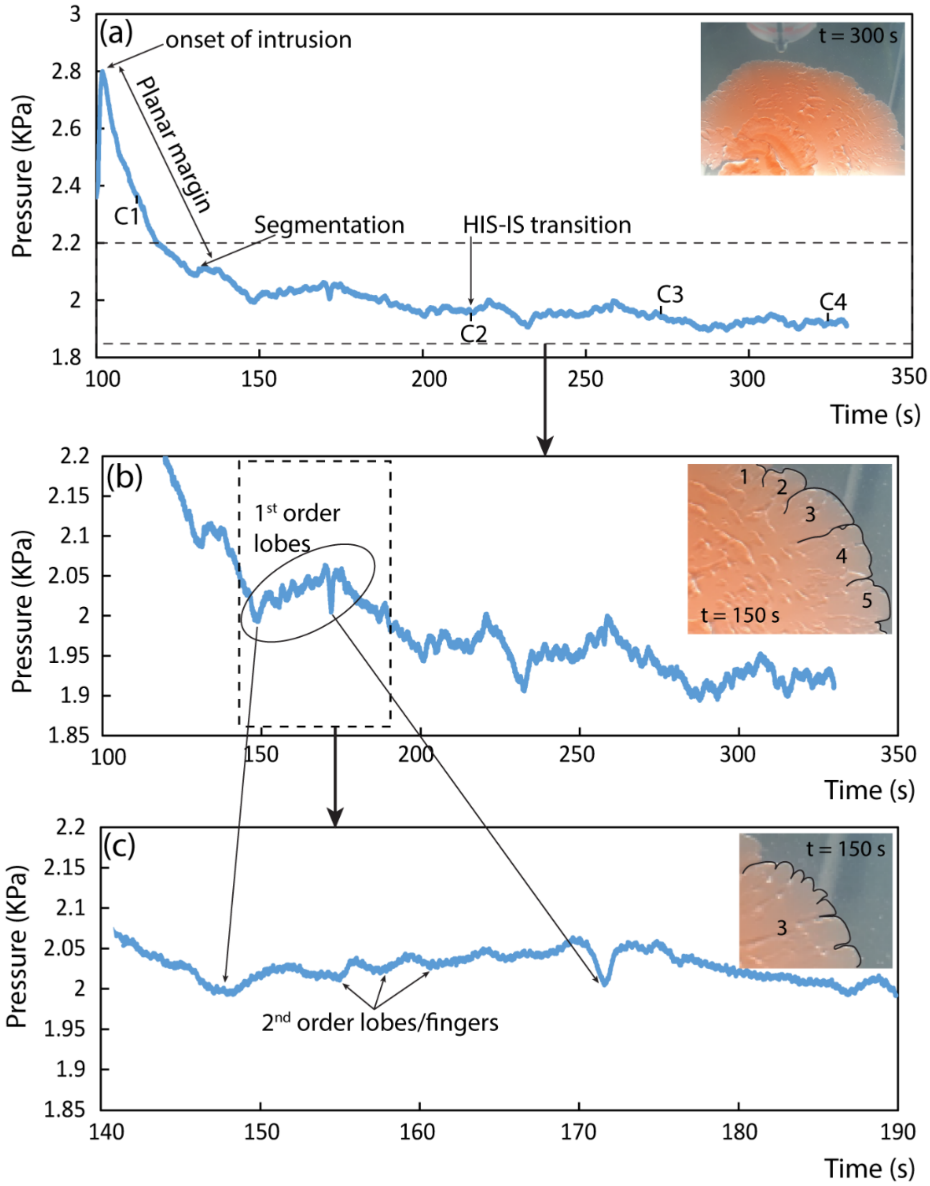

Figure 4.8: *(a) Injection pressure measured during sill emplacement in Exp. 5. Locations of aspect ratio measurements (C1-C4) and the horizontal inner sill to inclined sheet transition (HIS-IS) are indicated. Inset photograph shows the planar sill margin during initial growth stages. (b) Detail of part of (a) showing pressure fluctuations linked to the formation of first-order lobes (outlined in black with numbers in inset photograph). (c) Detail of part of (b) showing minor pressure fluctuations related to the growth and merger of second-order lobes or finger-like segments (outlined in black in inset photograph).*

4.4.2. Inlet pressure measurements

The pressure measured at the inlet of the needle during sill intrusion in Exp. 5 is plotted against time in Figure 4.8. Peak pressure coincides with intrusion initiation. The pressure then gradually drops with time as the sill radius increases, showing minor fluctuations (Fig. 4.8a). The initial pressure drop occurs without fluctuations, corresponding to the period when the sill propagates as a planar crack (Fig. 4.8a). At the end of this period, the intrusion starts to form a lobate margin. From this point onwards the pressure curve fluctuates within a broadly decreasing trend. Short wavelength periods of rising pressure (e.g., circled in Fig. 4.8b) occur during growth of first order lobes at the propagating front of the intrusion. Minor pressure variations during such periods of slightly increasing pressure corresponding to the growth of second order lobes and fingers (Fig. 4.8c). In contrast, the following periods of decreasing pressure correspond to times when earlier formed primary and secondary segments coalesce. There is no obvious change in the pressure curve when the horizontal inner sill (HIS) transitions to the inclined outer sheet (HIS-IS transition in Fig. 4.8a).

4.5. Discussion

Our experiments reveal the development of complex marginal segments and segment connectors within saucer-shaped intrusions, including pressure variations reflecting the development of these segments. We discuss the implications of these results below by considering how the evolution of the model sills in space and time may contribute to understanding of sill segmentation mechanisms. We also introduce a conceptual model for sill segmentation based on our experimental observations.

4.5.1. Sill segments and segment connectors

Our experiments have modelled saucer-shaped sills (Figs. 4.5, 4.6) with complex marginal finger-like and lobe segments, including segment connectors such as bridges and broken bridges. Such features are commonly observed in sedimentary basins such as the Raton, Karoo, Rockall, Faroe-Shetland, Northwest Australian shelf and Neuquén basins (Thomson and Hutton, 2004; Hansen and Cartwright, 2006; Schofield et al., 2012; Magee et al., 2016; Spacapan et al., 2017). The experiments reported here and in Arachchige et al. (Chapter 3), along with previous analogue hydrofracturing experiments using silica flour and clay as analogue host-rock materials (Chang, 2004; Wu, 2006) more closely simulate the natural complexity of sills and their marginal segmentation compared to penny- and saucer-shaped sills formed in sand (Galland et al., 2009; Mathiue et al., 2008) and gelatine (Kavanagh et al., 2006, 2018). This strongly suggests that upper crustal rocks behave as either elasto-plastic or visco-elasto-plastic materials during sill emplacement.

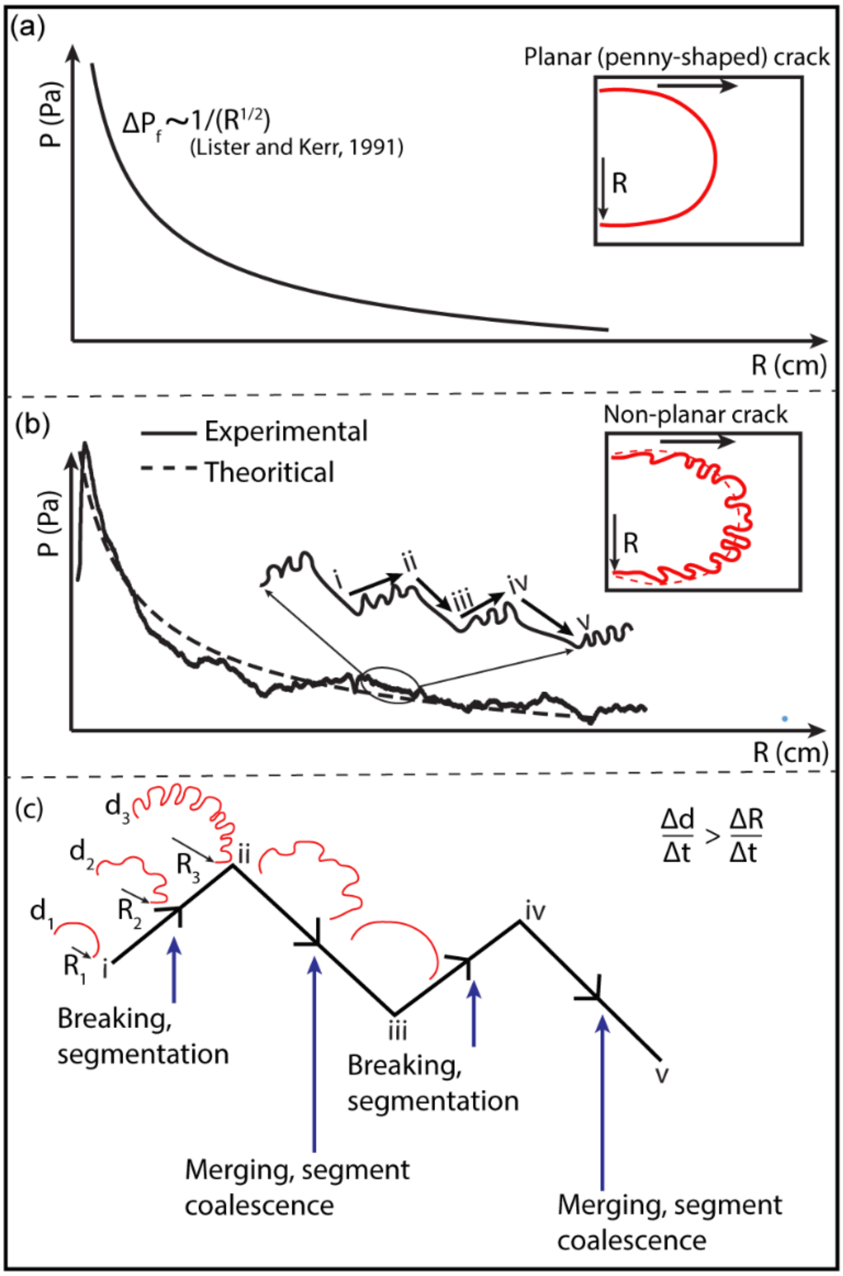

Figure 4.9: *Schematic pressure curves for (a) an ideal penny-shaped crack (Chang, 2004; Lister and Kerr, 1991) and (b) a non-planar experimental curve (Exp 5) superimposed on an ideal penny-shaped crack (dotted lines). (c) Interpretation of smaller scale pressure fluctuations highlighted in (b). During the initial growth of segments, the planar margin breaks down (i →ii; Fig. 4.9c) and the pressure rises due to a faster increase of the outer perimeter* ($\frac{\Delta d}{\Delta t}$) *compared to rate of change of sill radius* ($\frac{\Delta R}{\Delta t}$)*. Conversely, during subsequent stages of remerging/coalescence of segments (ii → iii), the pressure decreases as the rate of growth of the outer perimeter decreases. Note that, during transient pressure peaks or troughs, the change in intrusion radius (e.g.* R_3*–*R_1*) is smaller compared to the change in intrusion parameter (*d_3*–*d_1*). R − intrusion radius, d − intrusion perimeter, t − time.*

In addition to the rheology of the analogue host-rock material, we have also found that mechanical host-rock layering also controls the nature of sill segment geometries. In our experiments, the marginal segments formed during propagation of the inner sill along the L1/L2 interface are different to those formed when the inclined sheet propagates through the homogenous upper layer. During the inner sill stage, lobes and finger segments define a cyclic behaviour, showing a sequence of segment formation and coalescence. However, the new lobes and finger-like segments formed after the segment coalescence aren't linked to the previous segments meaning that segment propagation at the interface is history independent. However, once the inclined outer sheet forms, the marginal segments become three-dimensional, defining vertically offset, en-echelon, overlapping and/or underlapping segments, which later grow and connect.

Bridges and broken bridges formed by the inflation of segments (Schofield et al., 2012; Magee et al., 2019) also occur in our experiments. These segment connectors only form during the inclined sheet propagation stage of the experiments (Fig. 4.6). The growth of segment connectors results in the coalescence of segments. Therefore, the inclined sheet intrusion is characterised by a breaking (non-planar) and remerging (almost planar) sequence at the propagating front, which is further supported by the inlet pressure measurement variations (discussed in 4.4.2). This suggest that the nature of segments and their connectors evolve sequentially during growth of the experimental intrusions.

4.5.2. Insights on intrusion segmentation from pressure variations

Pressure variations during experimental sill intrusion (Fig. 4.8) provide important information for understanding flow dynamics and emplacement mechanisms. Intrusion pressure has been estimated using scaling laws in previous magma emplacement experiments (e.g., Kavanagh et al., 2015). However, fluid pressure is often directly measured in hydro-fracturing experiments (Chang, 2004; Wu, 2006; Hurt, 2012). Laboratory hydro-fractures described in Murdoch (1993a) and Chang (2004) using Center Hill clay and Georgia Red clay as analogue host rocks, respectively, show similar complex marginal segmentation structures to our model intrusions. Furthermore, the pressure curves of hydro-fractures measured by Chang (2004) and Wu (2006) reflect the formation of lobes during fracture segmentation. In Chang (2004), the injection pressure for fractures formed within Georgia Red Clay reached a peak value of ~1400 MPa and the pressure decreased up to 350 MPa during the final stage of crack growth. The maximum pressure measured during hydrofracture formation in Wu (2006) was between 6500 – 8000

MPa, decreasing to 500 – 3750 MPa, respectively. These measurements are three-orders of magnitude higher than the peak (2.8×10^{-3} MPa) and range of pressures ($1.9 – 2.8 \times 10^{-3}$ MPa) observed during the crack growth in our LRD experiments, although they show similar pressure fluctuations associated with the formation of segments. However, the differences in pressures in Chang (2004) and Wu (2006) to our results are mainly due to the use of virtually cohesionless dry particulate materials and the applied axial loads, respectively.

The fluid pressure (ΔP_f) required to propagate an ideal, fluid-filled penny-shaped crack is predicted to gradually decrease with increasing crack radius (R), according to the theoretical relationship (Lister and Kerr, 1991)

$$\Delta P_f \sim 1/ (R^{1/2}) \tag{4.4}$$

The pressure curve in Figure 9a was generated to compare this theoretical prediction with experimental data, and it can move along the y-axis depending on the fracture toughness (K_c) of the material ($\Delta P_f \sim K_c/R^{1/2}$), which is not well constrained for the LRD gels used in our experiments (Lister and Kerr, 1991; Chang, 2004). The pressure drop observed in Exp. 5 follows the general behaviour predicted by Eq. 4.4, with minor superimposed fluctuations as described above (Figs. 4.8a-b, 4.9b).

We interpret short periods of increasing pressure during sill growth (Figs. 4.9b and 4.9c; i→ii) to record segmentation events at the propagating sill margin. In Fig. 4.9b, we fit the Exp. 5 pressure curve to the theoretical curve by assuming the fracture toughness of the LRD is similar to that of theoretical curve. The perimeter (d) of an ideal penny-shaped crack increases with the radius according to $d = 2\pi R$. As the degree of marginal segmentation increases, the total outer perimeter of the propagating sill increases at a rate that is greater that of an ideal penny-shaped crack, resulting in a transient increase in pressure. The opposite happens during periods of transient pressure decrease (Figs. 4.9b and 4.9c; ii → iii), which we attribute to segment coalescence and an overall decrease in the perimeter length to a value that approaches that of an ideal penny shaped crack We therefore interpret the observed transient pressure fluctuations (Figs. 4.8b-c) to reflect periods of marginal segmentation and segment coalescence, which in turn drive changes in the rate of perimeter growth versus sill radius growth.

4.5.3. Conceptual model for sill segmentation

Two brittle fracturing mechanisms can lead to the formation of segments during emplacement of sills into brittle-elastic host rocks: (i) rotation of the principal stress axes ahead of the propagating fracture (Pollard et al., 1982; Nicholson and Pollard, 1985; Takada, 1990; Schofield et al., 2012); and (ii) exploitation of preferentially oriented, pre-existing weaknesses (Hutton, 2009; Schofield et al., 2012; Stephens et al., 2017). In the first mechanism, a change of stress orientation at the propagating front is likely due to the onset of mixed-mode loading (Mode I+II, Mode I+III), which results in twisting and splitting of the sill tip into en-echelon segments with a consistent stepping direction (Pollard et al., 1982; Nicholson and Pollard, 1985). In the second mechanism, sills emplaced into layered sedimentary strata can become segmented with inconsistent stepping direction as they follow pathways of least resistance (e.g., bedding planes, fault planes).

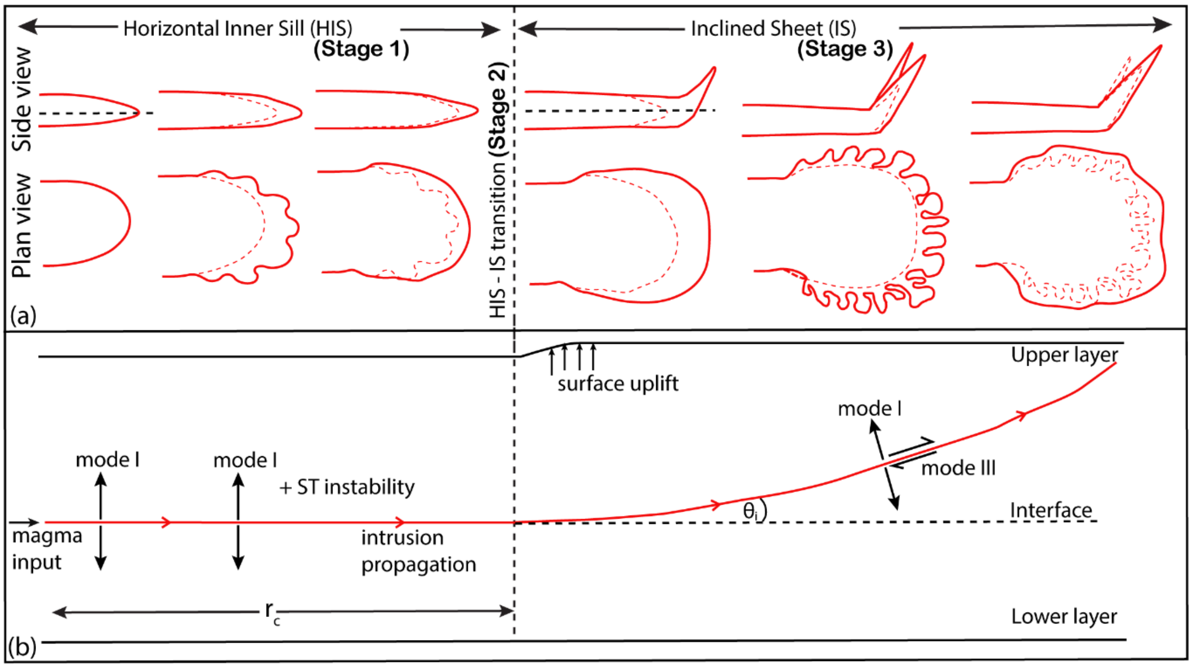

__Figure 4.10:__ Conceptual model for segment evolution within a saucer-shaped sill. (a) Side and plan views of propagating sill front geometries during: (i) the horizontal inner sill (Stage 1), (ii) the inner sill to inclined sheet transition (Stage 2), and iii) the inclined outer sheet (Stage 3). The continuous and dashed red lines represent active and previous propagating margins, respectively. (b) Simplified cross-sectional view (schematic) of the intrusion shown in (a) and the related emplacement mechanisms. Mode I – elastic fracture opening (planar). Mixed-mode (I+III) – breaking/twisting of the propagating front (segmentation).

However, inelastic mechanisms, such as ductile flow, shear faulting and granular flow (e.g., fluidisation) can also result in segment formation (Pollard et al., 1975; Thomson and Hutton, 2004; Schofield et al., 2012; Magee et al., 2016; Spacapan et al., 2017). Viscous-fingering instabilities (e.g., Saffman-Taylor instability) between a propagating magma front and a fluid host rock have previously been invoked as a mechanism of magma finger initiation (Pollard et al., 1975; Schofield et al., 2010). Moreover, a recent analysis by Ball et al. (2021, and references therein) show that visco-plastic Saffmann-Talyor instabilities can also form fracture fronts that are similar to magma fingers in both nature (Schofield et al., 2010) and the laboratory experiments reported here (Arachchige et al., 2021; Chapter 3 and 4).

Using this framework, and the sill segment and segment connector geometries and pressure curves recorded in our experiments, we propose the following multi-stage model for sill propagation and segmentation:

Stage 1: Emplacement and propagation of the horizontal inner sill (HIS) along a pre-existing horizontal interface (Fig. 4.10). A penny-shaped sill with a planar margin is initially emplaced as a Mode I fracture (opening mode) controlled by magma overpressure and the elastic response of the host rock, consistent with predictions from linear elastic fracture mechanics (LEFM) (e.g., Pollard and Holzhausen, 1979). The lobe and finger-like segments then start to emerge from the planar front without any offset or stepping, which suggests that the brittle-elastic LEFM mechanisms may not apply. Therefore, the marginal lobes and finger-like segments observed in this stage (Fig. 4.10b, Stage 1) are more likely linked to small-scale (< 1cm) visco-plastic version of Saffman-Taylor instabilities (Ball et al., 2021) occurring at the tip of the propagating sills. Segments will then propagate and grow provided there is sufficient driving pressure, and once they reach a critical dimension, segment coalescence then occurs to reform a planar sill front. This cyclic behaviour continues until the sill starts to propagate within the upper homogenous layer.

Stage 2: Transition from a horizontal inner sill (HIS) to an inclined outer sheet (IS) (Fig. 4.10; Stage 2). When the HIS reaches a critical radius (r_c) of approximately the thickness of the overburden (H) (i.e. $0.5 \leq r_c/H \leq 2.5$; Arachchige et al. Chapter 3), the sill becomes inclined relative to the L1/L2 interface and the free surface, forcing the stress at the sill tip to become asymmetric. Due to the elastic dominant interaction between the propagating sill and the upper free surface (Pollard and Holzhausen, 1979; Galland et al., 2008) the sill also climbs upwards due to the asymmetry of the stress field caused by the uplift of the overburden.

Stage 3: Sill segmentation within the inclined sheet (Fig. 4.10; Stage 3). Within the outer inclined sheet, sill propagation is no longer controlled by the anisotropy of the L1/L2 interface and the intrusion evolves in 3D. Propagation of the inclined sheet may cause surface uplift or force folding in the overburden, which will change the principal stress orientations (Fig. 4.10b). These changes at the sill front lead to 3D segmentation (> 1cm), which can be attributed to the mixed mode (Mode I+III) loading. In this case, the mode III component might be related to: (i) the 3D fracture geometry; (ii) flow front instability; or (iii) interactions with the side and upper boundaries. Unlike Stage 1, the segments are either co-planar and/or multi planar, with horizontal and vertical offsets. Inflation of these segments results in the formation of segment connectors such as bridges and broken bridges (Schofield et al., 2012; Magee et al., 2019). The margin then becomes planar (or quasi-planar) due to the connection of segments through bridges and broken bridges.

Our conceptual model provides an evolutionary framework for sill segmentation within saucer-shaped intrusions. The marginal lobes and finger-like segments observed within the interface (i.e., inner sill) and the homogenous upper layer (i.e., inclined sheet) in our experiments are more likely linked to small-scale (< 1cm) visco-plastic deformation instabilities occurring at the tip of the propagating sills and large-scale (>1 cm) mixed mode (Mode I+III) loading, respectively . This suggests the operation of scale-dependent deformation processes, with brittle-elastic (LEFM) processes dominating at the whole of intrusion scale and visco-plastic processes dominating at the crack tip scale. Moreover, the model is consistent with field and 3D seismic observations of sills and dykes in the shallow brittle upper crust. Importantly, it provides insights on the evolution of segments and segment connectors in time and space as an intrusion propagates in 3D.

4. 6. Conclusions

We present a detailed geometrical analysis of sill segmentation in a series of saucer-shaped sill emplacement experiments. Paraffin oil (model magma) is injected at constant flow rate into a layered, visco-elasto-plastic Laponite RD® (model crust). Our key conclusions are:

1. The modelled saucer-shaped sills have complex geometries and highly segmented margins consisting of fingers and lobes in both the inner flat sill, following a horizontal layer interface, and the outer inclined sheet where the segments exploit a 3D volume around the sill tip.

2. Due to the influence of the interface, the flat section of the intrusion is limited to co-planar segments and therefore no segment connectors formed. However, out of plane segments form within the inclined sheet that lead to the formation of segment connectors due to segment overlap and inflation.
3. Based on quantitative measurements of segment geometries, we determined that the segments have bimodal behaviour: i) interface-controlled aspect ratios (mode 1) forming wide lobes; and ii) homogenous layer-controlled aspect ratios (mode 2) forming narrow and long segments.
4. The pressure signatures measured during saucer-shape sill intrusion can be linked to periods of marginal segmentation and coalescence. Transient increases during sill propagation occur during period of increased segmentation, as the rate of perimeter growth increases, whereas transient pressure drops occur during segment coalescence, as the rate of perimeter growth decreases.
5. Our experiments suggest that segments and segment connectors evolve in space and time through multi-stage emplacement mechanisms. We present a conceptual sill segmentation model to account for the variety and sequence of segment geometries. We propose that the small-scale segments within the interface and the large-scale segments on inclined sheets are due to the visco-plastic instabilities and brittle-elastic fracturing, respectively.

Acknowledgements

We gratefully acknowledge support from an Australian Research Council Discovery Grant (DP190102422) to A.R.C., Dean's International Postgraduate Research Scholarship (DIPRS) and Graduate Research Completion Award (GRCA) scholarship from Monash University (Melbourne) to U.S.N.A.

Chapter 5

Discussion and conclusions

5.1. Key findings

The experimental approach in this project focussed on developing improved insights on the complexities of sills in nature, to better constrain how they are emplaced and propagate in the shallow crust, and how sill segmentation develops. My PhD research addresses two main overarching questions: (1) how do saucer-shaped sills form and propagate within rheologically complex host rocks; and (2) what controls the development of marginal lobes and fingers (i.e., sill segmentation) in sills? In order to answer these questions, a laboratory experimental program was developed, which focused on: (i) finding a suitable host rock analogue that satisfies rheological similarity with the visco-elasto-plastic behaviour of upper crustal rocks in nature; (ii) exploring the emplacement and growth mechanisms of saucer-shaped sills; and (iii) analysing the development of sill segments and segment connectors during the growth of saucer-shaped sills.

Rheological and mechanical testing of gel-forming Laponite RD® (LRD) was performed to evaluate its suitability as a visco-elasto-plastic host rock analogue in laboratory analogue experiments (Chapter 2). The analyses reveal that LRD gels made using 2.5 to 4 wt. % concentrations in water are suitable analogues to model brittle elastic and plastic deformation in the Earth's upper crust, and they exhibit visco-elasto-plastic behaviour during fracture propagation and the emplacement of model sills in the laboratory. Concentration above 4 wt. % are not recommended for analogue modelling applications because they form a gel structure too quickly, which prevents proper mixing, resulting in clumping of LRD powder and trapping of air bubbles. To model brittle viscoelastic behaviour in the laboratory, shear strain amplitudes γ must be < 10 % (at shear strain rate 0.1 s^{-1}). Plastic deformation occurs at shear strain amplitudes γ > 26.2 % and a more complex behaviour develops in between these strain limits. The transitions between these behaviours depend on the applied strain and strain rate, composition and curing time of the sample, and are much less effected by temperature.

Analogue experiments were carried out in a Perspex tank containing either a single layer or two layers of LRD. The physical properties (i.e., concentration and curing time) of the layer/s were varied to assess how the mechanical properties such as Young's modulus (E) of the analogue material influence the emplacement, growth and the propagation of saucer-shaped intrusions (Chapter 3). The modelled intrusions match the profiles of saucer-shaped sills in nature well. These intrusions form an inner flat sill along the layer interface and an inclined sheet through the upper homogenous layer. The inner sill to outer inclined sheet transition in the experiments is strongly dependent on the Young's modulus or rigidity ratio (E*) between the layers and the volumetric analogue magma injection rate. The saucer-shaped sills formed in the experiments are compatible with previous linear elastic fracture mechanics (LEFM) models in which the inner to outer sill transition is predicted to occur due to elasticity-dominated interactions between the growing inner sill, the surrounding host material and the free surface.

Saucer-shaped sills formed in the laboratory experiments have complex and highly segmented margins consisting of fingers and lobes that occur at the edges of both the inner sill and the outer inclined sheets. As the sill propagates, all marginal segments undergo periods of breaking/splitting and periods of merging/coalescence. Comparison of measurements of segment geometries from the margins of inner sills and outer inclined sheets indicate a bimodal behaviour: i) wide lobate segments with aspect ratios controlled by the Layer 1/2 interface; and ii) long and narrow segments with aspect ratios linked to fracture propagation within the homogeneous upper layer. Segment connectors such as bridges and broken bridges are only formed when the intrusion propagates within the upper homogenous layer. The main segmentation mechanism in the experiments is most likely linked to mixed Mode I+III fracturing (brittle-elastic), however it is also possible that visco-plastic Saffman-Taylor instabilities are linked to smaller scale segmentation in the vicinity of the crack tip. This suggests the operation of scale-dependent deformation processes, with brittle-elastic (LEFM) processes dominating at the whole of intrusion scale and visco-plastic processes dominating at the crack tip scale.

5.2. Research implications

5.2.1. Implications for analogue modelling of magma intrusions using Laponite RD® (LRD)

A wide variety of host rock and magma analogue materials have been used to model igneous intrusions such as dykes and sills. Most of these materials have simple end member rheological behaviours (e.g., elastic, plastic or viscous) capable of producing simple model intrusions. However, with the development of 3D seismic analysis and from recent field studies, we know that dykes and sills do not have simple, planar outer margins as traditionally considered, rather they are complex and segmented. A comprehensive rheological characterisation of LRD

(Chapter 2) indicates that it is a versatile material that exibits behaviours range from brittle-elastic, to elasto-visco-plastic to plastic, which is capable of modelling segmented intrusions with marginal lobes and fingers. I anticipate these findings will provide a link between our knowledge of segmented magmatic intrusions and rheologically complex upper crustal rocks. This in turn will provide a starting point for new geodynamic modelling investigations of non-planar magmatic intrusions, and a new set of parameters for the numerical modelling of segmented igneous intrusions.

5.2.2. Implications for the formation of dykes and sills with segmented margins

The formation of igneous dykes and sills with non-planar or segmented margins has conventionally been attributed to end member processes, such as LEFM. The scaled analogue experiments presented here replicate, for the first time, the geometries of complex marginal structures that are observed at the leading edges of igneous sills in nature. The experimental results also suggest the operation of scale-dependant processes during magma emplacement, such as brittle-elastic (LEFM) processes that dominate at the whole of intrusion scale, and visco-plastic processes that dominate at the vicinity of the crack tip. Therefore this thesis (Chapter 4) provides insights into the geometry and evolution of segments at the margins of sills and a conceptual dynamic model, which can be further applied to another igneous intrusions with non-planar margins (e.g., dykes).

5.2.3. Implications for Ni-Cu magmatic sulphide deposits

Finger-like structures that emerge from planar mafic sills are also known to trap Ni-Cu sulphides in poorly constrained narrow, elongated channels that occur from deep to shallow crustal levels (Naldrett, 1999; Seat et al., 2007; Stephen J. Barnes et al., 2016). Ni-Cu sulphide deposits, such as Noril'sk, Voisey Bay, Nebo-Babel and Jinchuan are hosted within igneous intrusions that show characteristic finger-like geometries (Saumur and Cruden, 2016). Therefore, flow of magma through elongate magma conduits is a major ore forming process. Despite an ever-increasing amount of surface and subsurface data with constantly improving resolution, understanding finger-like conduit geometries is still challenging. This thesis provides detailed information about the finger-like structures that emerge from planar igneous sheets that can be used to track magma flow pathways and to discover potential orthomagmatic ore deposits. The thesis provides critical insights into the fundamental mechanisms of how and where these finger-like geometries emerge from planar igneous intrusions, which can be developed into important tools for targeting Ni-Cu sulphide mineralisation.

5.3. Suggestions for future research

The experimental results outlined in this thesis provide insights on the geometries and emplacement mechanisms of complex saucer-shaped sills and sill segmentation, which can be compared directly to natural examples. However, the transport of magma within dykes and sills through the Earth's crust is complex and further work is required to fully understand their propagation mechanisms and controlling parameters. This future research should include:

Temperature dependant magma analogues: Our experiments did not incorporate the effects of solidification of the magma analogue, which is a variable that can be achieved in laboratory experiments with an appropriate setup and equipment (e.g., Chanceaux and Menand, 2014, 2016; Currier and Marsh, 2015). Magma viscosity increases by several orders of magnitude during cooling and solidification, making it one of the most important parameters governing the emplacement of intrusions. However, solidification effects are difficult to model in laboratory experiments due to challenging scaling requirements. Hence, most analogue models of igneous intrusion to date have been isothermal and the temperature dependence of viscosity has been ignored. Although several previous studies have used temperature dependant magma analogues in sill and dyke emplacement modelling (Taisne and Tait, 2011; Chanceaux and Menand, 2014, 2016; Currier and Marsh, 2015), no solidification experiments have been reported that replicate the results of our isothermal models. Therefore, the inclusion of temperature dependant magma analogues in future laboratory experiments using LRD gels will provide important insights on the role of magma cooling and solidification during the intrusion of saucer-shaped sills, and their segmentation.

Tracer particles and PIV (Particle Image Velocimetry): Techniques such as digital image correlation (DIC) and particle image velocimetry (PIV) using tracer particles can be used to map host rock deformation, analogue magma flow in laboratory experiments (Kavanagh et al., 2015, 2017, 2018a; Schmiedel et al., 2017). Even though analogue experiments are effective for generating 3D structures that are similar to those observed nature, due to their complexity they are often either described qualitatively or lack quantitative measurements. However, the ability to image and integrate measurements of surface and subsurface deformation and flow in laboratory intrusions using DIC and PIV techniques can bridge this gap and, in turn, further inform numerical modelling approaches.

Pressure measurements during experiments: Analysis of inlet pressures during laboratory crack propagation experiments can provide important information about flow dynamics and emplacement mechanisms. Most of the hydro-fractures modelled in the engineering literature successfully measure real-time pressure variations (Chang, 2004; Wu, 2006) . However, in most laboratory experiments of igneous dykes and sills, pressure has been either estimated using scaling laws or not recorded. We have shown in our preliminary study (Chapter 4) that adding a properly calibrated pressure sensor provides crucial information about intrusion growth and segmentation. Therefore, future efforts in laboratory modelling of igneous intrusions using pressure monitoring systems, especially when coupled with LRD as a host rock analogue will address this limitation. In this context, it is anticipated that the model results presented in this thesis will provide a starting point for more sophisticated future laboratory and numerical modelling of igneous intrusions.

References

Adam, J., Klinkmüller, M., Schreurs, G., Wieneke, B., 2013. Quantitative 3D strain analysis in analogue experiments simulating tectonic deformation: Integration of X-ray computed tomography and digital volume correlation techniques. Journal of Structural Geology 55, 127–149. https://doi.org/10.1016/j.jsg.2013.07.011

Adam, J., Urai, J.L., Wieneke, B., Oncken, O., Pfeiffer, K., Kukowski, N., Lohrmann, J., Hoth, S., van der Zee, W., Schmatz, J., 2005. Shear localisation and strain distribution during tectonic faulting - New insights from granular-flow experiments and high-resolution optical image correlation techniques. Journal of Structural Geology 27, 283–301. https://doi.org/10.1016/j.jsg.2004.08.008

Anderson, E.M., 1937. The Dynamics of the Formation of Cone-sheets, Ring-dykes, and Caldron-subsidences. Proceedings of the Royal Society of Edinburgh 56, 128–157. https://doi.org/10.1017/s0370164600014954

Arachchige, U.N., Cruden, A.R., Weinberg, R., 2021. Laponite gels - visco-elasto-plastic analogues for geological laboratory modelling. Tectonophysics 805, 228773. https://doi.org/10.1016/j.tecto.2021.228773

Bailey, R.C., 2006. Large time step numerical modelling of the flow of Maxwell materials. Geophysical Journal International 164, 460–466. https://doi.org/10.1111/j.1365-246X.2005.02788.x

Ball, T. V., Balmforth, N.J., Dufresne, A.P., 2021. Viscoplastic fingers and fractures in a Hele-Shaw cell. Journal of Non-Newtonian Fluid Mechanics 289, 104492. https://doi.org/10.1016/j.jnnfm.2021.104492

Barnes, S.J., Cruden, A.R., Arndt, N., Saumur, B.M., 2016. The mineral system approach applied to magmatic Ni – Cu – PGE sulphide deposits ☆. Ore Geology Reviews 76, 296–316. https://doi.org/10.1016/j.oregeorev.2015.06.012

Barnes, S.J., Cruden, A.R., Arndt, N., Saumur, B.M., 2016. The mineral system approach applied to magmatic Ni–Cu–PGE sulphide deposits. Ore Geology Reviews 76, 296–316. https://doi.org/10.1016/j.oregeorev.2015.06.012

Barnett, Z.A., Gudmundsson, A., 2014. Numerical modelling of dykes de fl ected into sills to form a magma chamber. Journal of Volcanology and Geothermal Research 281, 1–11. https://doi.org/10.1016/j.jvolgeores.2014.05.018

Beckett, F.M., Mader, H.M., Phillips, J.C., Rust, A.C., Witham, F., 2011. An experimental study of low-Reynolds-number exchange flow of two Newtonian fluids in a vertical pipe. Journal of Fluid Mechanics 682, 652–670. https://doi.org/10.1017/jfm.2011.264

Bertelsen, H.S., Rogers, B.D., Galland, O., Dumazer, G., Abbana Benanni, A., 2018a. Laboratory Modeling of Coeval Brittle and Ductile Deformation During Magma Emplacement Into Viscoelastic Rocks. Frontiers in Earth Science 6. https://doi.org/10.3389/feart.2018.00199

Bertelsen, H.S., Rogers, B.D., Galland, O., Dumazer, G., Benanni, A.A., 2018b. Laboratory modeling of coeval brittle and ductile deformation during magma emplacement into viscoelastic rocks. Frontiers in Earth Science 6, 5473. https://doi.org/10.3389/feart.2018.00199

Bonn, D., Kellay, H., Tanaka, H., Wegdam, G., Meunier, J., 1999. Laponite:What Is the Difference between a Gel and a Glass? Langmuir 15, 7534–7536. https://doi.org/10.1021/la990167t

Bonn, D., Tanase, S., Abou, B., Tanaka, H., Meunier, J., 2002. Laponite: Aging and shear rejuvenation of a colloidal glass. Physical Review Letters 89, 157011–157014. https://doi.org/10.1103/PhysRevLett.89.015701

Brizzi, S., Funiciello, F., Corbi, F., Di Giuseppe, E., Mojoli, G., 2016. Brizzi et al. (2016)_Salt matters_ How salt affects the rheological and physical properties of gelatine for analogue modelling _ Elsevier Enhanced Reader.pdf. https://doi.org/10.1016/j.tecto.2016.04.021

Bunger, A.P., Cruden, A.R., 2011. Modeling the growth of laccoliths and large mafic sills : Role of magma body forces. 116, 1–18. https://doi.org/10.1029/2010JB007648

Bunger, A.P., Cruden, A.R., 2011. Modeling the growth of laccoliths and large mafic sills: Role of magma body forces. Journal of Geophysical Research: Solid Earth 116, 1–18. https://doi.org/10.1029/2010JB007648

Bunger, A.P., Detournay, E., 2005. Asymptotic solution for a penny-shaped near-surface hydraulic fracture. Engineering Fracture Mechanics 72, 2468–2486. https://doi.org/10.1016/j.engfracmech.2005.03.005

Bunger, A.P., Detournay, E., Jeffrey, R.G., 2005. Étude Expérimentale Du Comportement En Bout D’Une Fracture Hydraulique Se Propageant Près D’Une Surface Libre. Comptes Rendus - Mecanique 333, 299–304. https://doi.org/10.1016/j.crme.2005.01.004

Bunger, A.P., Jeffrey, R.G., Detournay, E., 2008. Evolution and morphology of saucer-shaped sills in analogue experiments. Geological Society Special Publication 302, 109–120. https://doi.org/10.1144/SP302.8

Chanceaux, L., Menand, T., 2016. The effects of solidification on sill propagation dynamics and morphology. Earth and Planetary Science Letters 442, 39–50. https://doi.org/10.1016/j.epsl.2016.02.044

Chanceaux, L., Menand, T., 2014. Solidification effects on sill formation: An experimental approach. Earth and Planetary Science Letters 403, 79–88. https://doi.org/10.1016/j.epsl.2014.06.018

Chang, H., 2004. Hydraulic fracturing in particulate materials, Ph.D. thesis. Georgia Institute of Technology, GA. 267.

Chevallier, L., Woodford, A., 1999. Morpho-tectonics and mechanism of emplacement of the dolerite rings and sills of the western Karoo, South Africa. South African Journal of Geology 102, 43–54.

Chhabra, R.P., 2010. Non-Newtonian fluids: An introduction. Rheology of Complex Fluids 3–34. https://doi.org/10.1007/978-1-4419-6494-6_1

Christidis, G., Aldana, C., Chryssikos, G., Gionis, V., Kalo, H., Stöter, M., Breu, J., Robert, J.-L., 2018. The Nature of Laponite: Pure Hectorite or a Mixture of Different Trioctahedral Phases? Minerals 8, 314. https://doi.org/10.3390/min8080314

Cruden, A.R., Weinberg, R.F., 2018. Mechanisms of magma transport and storage in the lower and middle crust-magma segregation, ascent and emplacement. Volcanic and Igneous Plumbing Systems: Understanding Magma Transport, Storage, and Evolution in the

Earth's Crust. 13–53. https://doi.org/10.1016/B978-0-12-809749-6.00002-9

Cruden et al, 2017. Geometric Scaling of Tabular Igneous Intrusions: Implications for Emplacement and Growth. Advances in Volcanology 1–4. https://doi.org/10.1007/11157

Cummins, H.Z., 2007. Liquid, glass, gel: The phases of colloidal Laponite. Journal of Non-Crystalline Solids 353, 3891–3905. https://doi.org/10.1016/j.jnoncrysol.2007.02.066

Currier, R.M., Marsh, B.D., 2015. Mapping real time growth of experimental laccoliths: The effect of solidification on the mechanics of magmatic intrusion. Journal of Volcanology and Geothermal Research 302, 211–224. https://doi.org/10.1016/j.jvolgeores.2015.07.009

Delaney, P., Pollard, D., 1981. Deformation of Host Rocks and Flow of Magma during Growth of Minette Dikes and Breccia-bearing Intrusions near Ship Rock , New Mexico. Geological Survey Professional Paper 69.

Di Giuseppe, E., Funiciello, F., Corbi, F., Ranalli, G., Mojoli, G., 2009. Gelatins as rock analogs: A systematic study of their rheological and physical properties. Tectonophysics 473, 391–403. https://doi.org/10.1016/j.tecto.2009.03.012

Duarte, J.C., Schellart, W.P., Cruden, A.R., 2014. Rheology of petrolatum-paraffin oil mixtures: Applications to analogue modelling of geological processes. Journal of Structural Geology 63, 1–11. https://doi.org/10.1016/j.jsg.2014.02.004

Eide, C.H., Schofield, N., Jerram, D.A., Howell, J.A., 2017. Basin-scale architecture of deeply emplaced sill complexes: Jameson Land, East Greenland Christian. Journal of the Geological Society 174, 23–40. https://doi.org/10.1144/jgs2016-018

Ernst, R.E., Head, J.W., Parfitt, E., Grosfils, E., Wilson, L., 1995. Giant radiating dyke swarms on Earth and Venus. Earth Science Reviews 39, 1–58. https://doi.org/10.1016/0012-8252(95)00017-5

Eslami, A., Taghavi, S.M., 2017. Viscous fingering regimes in elasto-visco-plastic fluids. Journal of Non-Newtonian Fluid Mechanics 243, 79–94. https://doi.org/10.1016/j.jnnfm.2017.03.007

Fialko, Y., Khazan, Y., Simons, M., 2001. Deformation due to a pressurized horizontal circular crack in an elastic half-space, with applications to volcano geodesy. Geophysical Journal International 146, 181–190. https://doi.org/10.1046/j.1365-246X.2001.00452.x

Galland, O., Bertelsen, H.S., Guldstrand, F., Girod, L., Johannessen, R.F., Bjugger, F., Burchardt, S., Mair, K., 2016. Application of open-source photogrammetric software MicMac for monitoring surface deformation in laboratory models. Journal of Geophysical Research: Solid Earth 121, 2852–2872. https://doi.org/10.1002/2015JB012564

Galland, O., Holohan, E., Vries, B.V.W. De, Burchardt, S., 2015. Laboratory Modelling of Volcano Plumbing Systems : A Review. https://doi.org/10.1007/11157

Galland, O., Planke, S., Neumann, E.R., Malthe-Sørenssen, A., 2009. Experimental modelling of shallow magma emplacement: Application to saucer-shaped intrusions. Earth and Planetary Science Letters 277, 373–383. https://doi.org/10.1016/j.epsl.2008.11.003

Galland, O., Secondary, C.A., Author, C., Galland, O., Holohan, E., Burchardt, S., Galland, O., n.d. Advances in Volcanology Laboratory Modelling of Volcano Plumbing Systems Chapter # Laboratory Modelling of Volcano Plumbing Systems Olivier Galland , Eoghan Holohan , Benjamin van Wyk de Vries , Steffi Burchardt.

Galland, O., Spacapan, J.B., Rabbel, O., Mair, K., Soto, F.G., Eiken, T., Schiuma, M., Leanza, H.A., 2019. Structure, emplacement mechanism and magma-flow significance of igneous fingers – Implications for sill emplacement in sedimentary basins. Journal of Structural Geology 124, 120–135. https://doi.org/10.1016/j.jsg.2019.04.013

Gill, S.P.A., Walker, R.J., 2020. The roles of elastic properties , magmatic pressure , and tectonic stress in saucer- shaped sill growth. Journal of Geophysical Research: Solid Earth 0–2. https://doi.org/10.1029/2019JB019041

Gill, S.P.A., Walker, R.J., 2020. The Roles of Elastic Properties, Magmatic Pressure, and Tectonic Stress in Saucer-Shaped Sill Growth. Journal of Geophysical Research: Solid Earth 125, 1–24. https://doi.org/10.1029/2019jb019041

Giuseppe, E. Di, Funiciello, F., Corbi, F., Ranalli, G., Mojoli, G., 2009. Tectonophysics Gelatins as rock analogs : A systematic study of their rheological and physical properties. Tectonophysics 473, 391–403. https://doi.org/10.1016/j.tecto.2009.03.012

Griffiths, B.R.W., Fink, J.H., 1993. Effects of surface cooling on the spreading of lava flows and domes. 252.

Griffiths, R.W., 2000. The Dynamics of Lava Flows. Annual Review of Fluid Mechanics 32, 477–518. https://doi.org/10.1146/annurev.fluid.32.1.477

Hansen, D.M., Cartwright, J., 2006. Saucer-shaped sill with lobate morphology revealed by 3D seismic data: implications for resolving a shallow-level sill emplacement mechanism. Journal of the Geological Society 163, 509–523. https://doi.org/10.1144/0016-764905-073

Haug, Ø.T., Galland, O., Souloumiac, P., Souche, A., Guldstrand, F., Schmiedel, T., 2017. Inelastic damage as a mechanical precursor for the emplacement of saucer-shaped intrusions. Geology 45, 1099–1102. https://doi.org/10.1130/G39361.1

Holness, M.B., 2003. The Traigh Bhan na Sgurra Sill, Isle of Mull: Flow Localization in a Major Magma Conduit. Journal of Petrology 44, 1961–1976. https://doi.org/10.1093/petrology/egg066

Hubbert, M.K., 1937. Theory of scale models as applied to the study of geologic structures. GSA Bulletin 48, 1459–1520. https://doi.org/10.1130/GSAB-48-1459

Hurt, R.S., 2012. Toughness-Dominated Hydraulic Fractures in Cohesionless Particulate Materials, Ph.D. thesis. Georgia Institute of Technology, GA.

Hutton, D.H.W., 2009. Insights into magmatism in volcanic margins: bridge structures and a new mechanism of basic sill emplacement - Theron Mountains, Antarctica. Petroleum Geoscience 15, 269–278. https://doi.org/10.1144/1354-079309-841

Kato, M., Fujii, T., Onaka, S., 1996. Elastic strain energies of sphere, plate and needle inclusions. Materials Science and Engineering A 211, 95–103. https://doi.org/10.1016/0921-5093(95)10091-1

Kaushal, M., Joshi, Y.M., 2014. Linear viscoelasticity of soft glassy materials. Soft Matter 10, 1891–1894. https://doi.org/10.1039/c3sm52978a

Kavanagh, J.L., Boutelier, D., Cruden, A.R., 2015. The mechanics of sill inception, propagation and growth: Experimental evidence for rapid reduction in magmatic overpressure. Earth and Planetary Science Letters 421, 117–128. https://doi.org/10.1016/j.epsl.2015.03.038

Kavanagh, J.L., Burns, A.J., Hilmi Hazim, S., Hignett, S., Wood, E.P., Martin, S.A., Dennis, D.J.C.C., 2018a. Challenging dyke ascent models using novel laboratory experiments: Implications for reinterpreting evidence of magma ascent and volcanism. Journal of Volcanology and Geothermal Research 354, 87–101. https://doi.org/10.1016/j.jvolgeores.2018.01.002

Kavanagh, J.L., Engwell, S.L., Martin, S.A., 2018b. A review of laboratory and numerical modelling in volcanology. Solid Earth 9, 531–571.

Kavanagh, J.L., Menand, T., Daniels, K.A., 2013. Gelatine as a crustal analogue: Determining elastic properties for modelling magmatic intrusions. Tectonophysics 582, 101–111. https://doi.org/10.1016/j.tecto.2012.09.032

Kavanagh, J.L., Menand, T., Sparks, R.S.J., 2006. An experimental investigation of sill formation and propagation in layered elastic media. Earth and Planetary Science Letters 245, 799–813. https://doi.org/10.1016/j.epsl.2006.03.025

Kavanagh, J.L., Rogers, B.D., Boutelier, D., Cruden, A.R., 2017. Controls on sill and dyke-sill hybrid geometry and propagation in the crust: The role of fracture toughness. Tectonophysics 698, 109–120. https://doi.org/10.1016/j.tecto.2016.12.027

Kerr, R.C., 2001. Thermal erosion by laminar lava flows. Journal of Geophysical Research: Solid Earth 106, 26453–26465. https://doi.org/10.1029/2001jb000227

Kerr, R.C., Griffiths, R.W., Cashman, K. V., 2006. Formation of channelized lava flows on an unconfined slope. Journal of Geophysical Research: Solid Earth 111, 1–13. https://doi.org/10.1029/2005JB004225

Lapasin, R., Abrami, M., Grassi, M., Šebenik, U., 2017. Rheology of Laponite-scleroglucan hydrogels. Carbohydrate Polymers 168, 290–300. https://doi.org/10.1016/j.carbpol.2017.03.068

Lister, B.J.R., 1990. Buoyancy-driven fluid fracture : the effects of material toughness and of low-viscosity precursors.

Lister, J.R., Kerr, R.C., 1991. Fluid-mechanical models of crack propagation and their application to magma transport in dykes. Journal of Geophysical Research 96, 10049. https://doi.org/10.1029/91JB00600

Magee, C., Muirhead, J., Schofield, N., Walker, R.J., Galland, O., Holford, S., Spacapan, J., Jackson, C.A., Mccarthy, W., 2018a. Structural signatures of igneous sheet intrusion propagation Craig. Journal of Structural Geology. https://doi.org/10.1016/j.jsg.2018.07.010.This

Magee, C., Muirhead, J., Schofield, N., Walker, R.J., Galland, O., Holford, S., Spacapan, J., Jackson, C.A.L., McCarthy, W., 2019. Structural signatures of igneous sheet intrusion propagation. Journal of Structural Geology 125, 148–154. https://doi.org/10.1016/j.jsg.2018.07.010

Magee, C., Muirhead, J.D., Karvelas, A., Holford, S.P., Jackson, C.A.L., Bastow, I.D., Schofield, N., Stevenson, C.T.E., McLean, C., McCarthy, W., Shtukert, O., 2016. Lateral magma flow in mafic sill complexes. Geosphere 12, 809–841. https://doi.org/10.1130/GES01256.1

Magee, C., Stevenson, C.T.E., Ebmeier, S.K., Keir, D., Hammond, J.O.S., Gottsmann, J.H., Whaler, K.A., Schofield, N., Jackson, C.A.L., Petronis, M.S., O'Driscoll, B., Morgan, J., Cruden, A., Vollgger, S.A., Dering, G., Micklethwaite, S., Jackson, M.D., 2018b. Magma plumbing systems: A geophysical perspective. Journal of Petrology 59, 1217–1251. https://doi.org/10.1093/petrology/egy064

Malthe-Sørenssen, Planke, A., Svensen, S.H., Jamtveit, B., 2004. Formation of saucer-shaped sills. Geological Society, London, Special Publications 234, 215–227.

Mathieu, L., van Wyk de Vries, B., Holohan, E.P., Troll, V.R., 2008. Dykes, cups, saucers and sills: Analogue experiments on magma intrusion into brittle rocks. Earth and Planetary Science Letters 271, 1–13. https://doi.org/10.1016/j.epsl.2008.02.020

Menand, T., 2008. The mechanics and dynamics of sills in layered elastic rocks and their implications for the growth of laccoliths and other igneous complexes. Earth and Planetary Science Letters 267, 93–99. https://doi.org/10.1016/j.epsl.2007.11.043

Menand, T., Tait, S.R., 2002. The propagation of a buoyant liquid-filled fissure from a source under constant pressure: An experimental approach. Journal of Geophysical Research: Solid Earth 107, ECV 16-1-ECV 16-14. https://doi.org/10.1029/2001JB000589

Miles, A., Cartwright, J., 2010. Hybrid flow sills: A new mode of igneous sheet intrusion. Geology 38, 343–346. https://doi.org/10.1130/G30414.1

Mohanty, R.P., Joshi, Y.M., 2016. Chemical stability phase diagram of aqueous Laponite dispersions. Applied Clay Science 119, 243–248. https://doi.org/10.1016/j.clay.2015.10.021

Morariu, S., Lămătic, I., Bercea, M., 2009. Rheological behaviour of smectite aqueous dispersions. Revue Roumaine de Chimie 54, 975–980.

Mourchid, A., Lécolier, E., Van Damme, H., Levitz, P., 1998. On Viscoelastic, Birefringent, and Swelling Properties of Laponite Clay Suspensions: Revisited Phase Diagram. Langmuir 14, 4718–4723. https://doi.org/10.1021/la980117p

Muirhead, J.D., Airoldi, G., Rowland, J. V, White, J.D.L., Muirhead, J.D., Airoldi, G., Rowland, J. V, White, J.D.L., Mountain, T.C., Land, S.V., 2012. Interconnected sills and inclined sheet intrusions control shallow magma transport in the Ferrar large igneous province , Antarctica. https://doi.org/10.1130/B30455.1

Muirhead, J.D., Van Eaton, A.R., Re, G., White, J.D.L., Ort, M.H., 2016. Monogenetic volcanoes fed by interconnected dikes and sills in the Hopi Buttes volcanic field, Navajo Nation, USA. Bulletin of Volcanology 78, 1–16. https://doi.org/10.1007/s00445-016-1005-8

Murdoch, L.C., 1993a. Hydraulic fracturing of soil during laboratory experiments Part 2. Propagation. Geotechnique 43, 255–265. https://doi.org/10.1680/geot.1993.43.2.255

Murdoch, L.C., 1993b. Hydraulic fracturing of soil during laboratory experiments Part 1 . Methods and observations. Geotechnique 43, 255–265. https://doi.org/10.1680/geot.1993.43.2.255

Naldrett, A.J., 1999. World-class Ni-Cu-PGE deposits: Key factors in their genesis. Mineralium Deposita 34, 227–240. https://doi.org/10.1007/s001260050200

Nicholson, R., Pollard, D.D., 1985. Dilation and linkage of echelon cracks. Journal of

Structural Geology 7, 583–590. https://doi.org/10.1016/0191-8141(85)90030-6

Norris, J., Giese, R.F., Costanzo, P.M., Vanoss, C.J., 1993. The Surface Energies of Cation Substituted Laponite. Clay Minerals 28, 1–11. https://doi.org/10.1180/claymin.1993.028.1.01

Pek-Ing, A., Yee-Kwong, L., 2015. Surface chemistry and rheology of Laponite dispersions - Zeta potential, yield stress, ageing, fractal dimension and pyrophosphate. Applied Clay Science 107, 36–45. https://doi.org/10.1016/j.clay.2015.01.033

Persikov, E.S., 1991. The Viscosity of Magmatic Liquids: Experiment, Generalized Patterns. A Model for Calculation and Prediction. Applications. 1–40. https://doi.org/10.1007/978-1-4612-3128-8_1

Pihler-Puzović, D., Peng, G.G., Lister, J.R., Heil, M., Juel, A., 2018. Viscous fingering in a radial elastic-walled Hele-Shaw cell. Journal of Fluid Mechanics 849, 163–191. https://doi.org/10.1017/jfm.2018.404

Pollard, D., Delaney, P.T., Segall, P., 1982. Formation and interpretation of dilatant echelon cracks. Geological Society of America Bulletin 93, 1291–1303. https://doi.org/10.1130/0016-7606(1982)93<1291:faiode>2.0.co

Pollard, D., Johnson, M., 1973. David d. pollard. Tectonophysics 18, 311–354.

Pollard, D.D., 1973. Derivation and evaluation of a mechanical model for sheet intrusions. Tectonophysics 19, 233–269. https://doi.org/10.1016/0040-1951(73)90021-8

Pollard, D.D., Holzhausen, G., 1979. On the mechanical interaction between a fluid-filled fracture and the earth's surface. Tectonophysics 53, 27–57. https://doi.org/10.1016/0040-1951(79)90353-6

Pollard, D.D., Johnson, A.M., 1973. Mechanics of growth of some laccolithic intrusions in the Henry mountains, Utah, II. Bending and failure of overburden layers and sill formation. Tectonophysics 18, 311–354. https://doi.org/10.1016/0040-1951(73)90051-6

Pollard, D.D., Muller, O.H., Dockstader, D.R., 1975. The form and growth of fingered sheet intrusions. Bulletin of the Geological Society of America 86, 351–363. https://doi.org/10.1130/0016-7606(1975)86<351:TFAGOF>2.0.CO;2

Polteau, S., Mazzini, A., Galland, O., Planke, S., Malthe-Sørenssen, A., 2008. Saucer-shaped intrusions: Occurrences, emplacement and implications. Earth and Planetary Science Letters 266, 195–204. https://doi.org/10.1016/j.epsl.2007.11.015

Poppe, S., Holohan, E.P., Galland, O., Buls, N., Van Gompel, G., Keelson, B., Tournigand, P.Y., Brancart, J., Hollis, D., Nila, A., Kervyn, M., 2019. An inside perspective on magma intrusion: Quantifying 3d displacement and strain in laboratory experiments by dynamic X-ray computed tomography. Frontiers in Earth Science 7, 1–20. https://doi.org/10.3389/feart.2019.00062

Poppe, S., Holohan, E.P., Rudolf, M., Rosenau, M., Galland, O., Delcamp, A., Kervyn, M., 2021. Mechanical properties of quartz sand and gypsum powder (plaster) mixtures: Implications for laboratory model analogues for the Earth's upper crust. Tectonophysics 814. https://doi.org/10.1016/j.tecto.2021.228976

Ramberg, H., 1967. Model Experimentation of the Effect of Gravity on Tectonic Processes. Geophysical Journal of the Royal Astronomical Society 14, 307–329. https://doi.org/10.1111/j.1365-246X.1967.tb06247.x

Ranalli, G., 2001. Experimental tectonics: From Sir James Hall to the present. Journal of Geodynamics 32, 65–76. https://doi.org/10.1016/S0264-3707(01)00023-0

Reber, J.E., Cooke, M.L., Dooley, T.P., 2020. What model material to use? A Review on rock analogs for structural geology and tectonics. Earth-Science Reviews 202. https://doi.org/10.1016/j.earscirev.2020.103107

Riller, U., Cruden, A.R., Boutelier, D., Schrank, C.E., 2012. The causes of sinuous crustal-scale deformation patterns in hot orogens: Evidence from scaled analogue experiments and the southern Central Andes. Journal of Structural Geology 37, 65–74. https://doi.org/10.1016/j.jsg.2012.02.002

Rivalta, E., B, M., Dahm, T., 2005. Buoyancy-driven fracture ascent : Experiments in layered gelatine. 144, 273–285. https://doi.org/10.1016/j.jvolgeores.2004.11.030

Rubin, A.M., 1995. Propagation of magma-filled cracks. Annu. Rev. Earth Planet. Sci 287–336.

Rubin, A.M., 1993. Tensile fracture of rock at high confining pressure Implications for dike propagation. Journal of Geophysical Research 98, 919–935.

Ruzicka, B., Zaccarelli, E., 2011. A fresh look at the Laponite phase diagram. Soft Matter 7, 1268–1286. https://doi.org/10.1039/c0sm00590h

Saffman, P.G., Taylor, F.R.S., 1958. The Penetration of a fluid into a porous medium or Hele-Shaw cell containing a more viscous liquid. Proceedings of the Royal Society A 245, 312–329. https://doi.org/http://doi.org/10.1098/rspa.1958.0085

Saumur, B.M., Cruden, A.R., 2016. On the emplacement of the voisey's bay intrusion (Labrador, Canada). Bulletin of the Geological Society of America 128, 147–168. https://doi.org/10.1130/B31240.1

Schmiedel, T., Galland, O., Breitkreuz, C., 2017. Dynamics of Sill and Laccolith Emplacement in the Brittle Crust: Role of Host Rock Strength and Deformation Mode. Journal of Geophysical Research: Solid Earth 122, 8860–8871. https://doi.org/10.1002/2017JB014468

Schmiedel, T., Galland, O., Haug, T., Dumazer, G., Breitkreuz, C., 2019. Coulomb failure of Earth's brittle crust controls growth, emplacement and shapes of igneous sills, saucer-shaped sills and laccoliths. Earth and Planetary Science Letters 510, 161–172. https://doi.org/10.1016/j.epsl.2019.01.011

Schofield, N., Heaton, L., Holford, S.P., Archer, S.G., Jackson, C.A.L., Jolley, D.W., 2012. Seismic imaging of "broken bridges": Linking seismic to outcrop-scale investigations of intrusive magma lobes. Journal of the Geological Society 169, 421–426. https://doi.org/10.1144/0016-76492011-150

Schofield, N., Stevenson, C., Reston, T., 2010. Magma fingers and host rock fluidization in the emplacement of sills. Geology 38, 63–66. https://doi.org/10.1130/G30142.1

Schofield, Brown, D.J., Magee, C., Stevenson, C.T., 2012. Sill morphology and comparison of brittle and non-brittle emplacement mechanisms. Journal of the Geological Society 169, 127–141. https://doi.org/10.1144/0016-76492011-078

Schrank, C.E., Fusseis, F., Karrech, A., 2012. Thermal-elastic stresses and the criticality of the continental crust. 13, 1–21. https://doi.org/10.1029/2012GC004085

Seat, Z., Beresford, S.W., Grguric, B.A., Waugh, R.S., Hronsky, J.M.A., Gee, M.A.M., Groves, D.I., Mathison, C.I., 2007. Architecture and emplacement of the Nebo-Babel gabbronorite-hosted magmatic Ni-Cu-PGE sulphide deposit, West Musgrave, Western Australia. Mineralium Deposita 42, 551–581. https://doi.org/10.1007/s00126-007-0123-9

Spacapan, J.B., Galland, O., Leanza, H.A., Planke, S., 2017. Igneous sill and finger emplacement mechanism in shale-dominated formation: a field study at Cuesta del Chihuido, Neuquén Basin, Argentina. Journal of the Geological Society 174, 422–433. https://doi.org/10.1144/jgs2016-056

Spence, D.A., Turcotte, D.L., 1985. Magma-driven propagation of cracks. Journal of Geophysical Research 90, 575–580.

Stephens, T.L., Walker, R.J., Healy, D., Bubeck, A., England, R.W., McCaffrey, K.J.W., 2017. Igneous sills record far-field and near-field stress interactions during volcano construction: Isle of Mull, Scotland. Earth and Planetary Science Letters 478, 159–174. https://doi.org/10.1016/j.epsl.2017.09.003

Taisne, B., Tait, S., 2011. Effect of solidification on a propagating dike. Journal of Geophysical Research: Solid Earth 116, 1–14. https://doi.org/10.1029/2009JB007058

Taisne, B., Tait, S., 2009. Eruption versus intrusion ? Arrest of propagation of constant volume , buoyant , liquid-filled cracks in an elastic , brittle host. 114, 1–7. https://doi.org/10.1029/2009JB006297

Takada, A., 1990. Experimental Study on Propagation of Liquid-Filled Crack in Gelatin : Shape and Velocity in Hydrostatic Stress Condition. 95, 8471–8481.

ten Grotenhuis, S.M., Piazolo, S., Pakula, T., Passchier, C.W., Bons, P.D., 2002. Are polymers suitable rock analogs? Tectonophysics 350, 35–47. https://doi.org/10.1016/S0040-1951(02)00080-X

Thomson, K., Hutton, D., 2004. Geometry and growth of sill complexes: Insights using 3D seismic from the North Rockall Trough. Bulletin of Volcanology 66, 364–375. https://doi.org/10.1007/s00445-003-0320-z

Traversa, P., Pinel, V., Grasso, J.R., 2010. A constant influx model for dike propagation:

Implications for magma reservoir dynamics. Journal of Geophysical Research: Solid Earth 115, 1–18. https://doi.org/10.1029/2009JB006559

Valentine, G.A., Krogh, K.E.C., 2006. Emplacement of shallow dikes and sills beneath a small basaltic volcanic center - The role of pre-existing structure (Paiute Ridge, southern Nevada, USA). Earth and Planetary Science Letters 246, 217–230. https://doi.org/10.1016/j.epsl.2006.04.031

van Otterloo, J., Cruden, A.R., 2016. Rheology of pig skin gelatine: Defining the elastic domain and its thermal and mechanical properties for geological analogue experiment applications. Tectonophysics 683, 86–97. https://doi.org/10.1016/j.tecto.2016.06.019

Walker, R.J., Gill, S.P.A., 2020. Tectonic stress controls saucer-shaped sill geometry and emplacement mechanism. Geology 48, 898–902. https://doi.org/10.1130/G47604.1

Wallace, J.F., Rutherford, C.J., 2015. Geotechnical properties of LAPONITE RD®. Geotechnical Testing Journal 38, 574–587. https://doi.org/10.1520/GTJ20140211

Weijermars, R., Schmeling, H., 1986. Scaling of Newtonian and non-Newtonian fluid dynamics without inertia for quantitative modelling of rock flow due to gravity (including the concept of rheological similarity). Physics of the Earth and Planetary Interiors 43, 316–330. https://doi.org/10.1016/0031-9201(86)90021-X

Willenbacher, N., 1996. Unusual thixotropic properties of aqueous dispersions of Laponite RD. Journal of Colloid and Interface Science 182, 501–510. https://doi.org/10.1006/jcis.1996.0494

Wu, R., 2006. Some Fundamental Mechanisms of Hydraulic Fracturing, Ph.D. thesis. Georgia Institute of Technology, GA. 301.

Xue, L., Qin, S.Q., Pan, X.H., Chen, H.R., Yang, B.C., 2017. A possible explanation of the stair-step brittle deformation evolutionary pattern of a rockslide. Geomatics, Natural Hazards and Risk 8, 1456–1476. https://doi.org/10.1080/19475705.2017.1345793

Zwaan, F., Schreurs, G., 2016. How oblique extension and structural inheritance influence rift segment interaction: Insights from 4D analog models. Interpretation 5, SD119-SD138. https://doi.org/10.1190/INT-2016-0063.1

Zwaan, F., Schreurs, G., Adam, J., 2018. Effects of sedimentation on rift segment evolution and rift interaction in orthogonal and oblique extensional settings: Insights from analogue models analysed with 4D X-ray computed tomography and digital volume correlation techniques. Global and Planetary Change 171, 110–133. https://doi.org/10.1016/j.gloplacha.2017.11.002

Appendix 1

'Cookbook' for Laponite RD® preparation

Laponite® has been used extensively in colloidal and rheological modification analysis works (Mourchid et al., 1998; Bonn et al., 1999; Ruzicka and Zaccarelli, 2011; Christidis et al., 2018). However, sample preparation used here is different from these previous studies. In this section, we illustrate general guidelines and some of the specific aspects of sample preparation procedures:

1. In order to get fully hydrated transparent suspensions, desired concentrations of Laponite powder need to be vigorously stirred either with distilled or ultrapure water (Milli-Q-Plus).

2. It is highly recommend adding powder to the distilled water over the course of 15-30 s while the mixer is rotating.

3. The solution has to be stirred rigorously until all the powder dissolves in the water. Even though different stirring times have been used by different studies (10-30 min), stirring for 15 - 20 min is recommended.

4. In order to get a chemically stable solution, working with high pH values (pH =10) is necessary and measurement of the pH of water before mixing or after adding Laponite is recommended. NaOH can be added to the solution in order to get the desired pH value.

5. However, if after 15- 20 min rigorous mixing the solution is incomplete (opaque), pass the solution through a filter (0.8-1 μm, Millipore Milliex AA).

Appendix 2

This appendix contains:

- The side view video of the Exp. 6 in Chapter 3 and 4 – 7 frames per second
- The plan view video of the Exp. 6 in Chapter 3 and 4 - 7 frames per second

The file set can be downloaded via the following link:

https://figshare.com/s/0715de0ba91b33cb552e